

**Structural and Biochemical Analysis of G Protein-Coupled Receptor Kinase Activation and
Small Molecule Inhibitor Selectivity**

by

Marilyn Claire Cato

A dissertation submitted in partial fulfillment
of the requirements for the degree of
Doctor of Philosophy
(Biological Chemistry)
in The University of Michigan
2019

Doctoral Committee:

Professor Janet L. Smith, Co-Chair
Adjunct Professor John J. G. Tesmer, Co-Chair
Assistant Professor Peter L. Freddolino
Professor Debra A. Thompson
Professor John R. Traynor

Marilyn Claire Cato

catomc@umich.edu

ORCID iD: 0000-0002-3063-3891

Acknowledgements

Throughout my time in graduate school, I have received an immense amount of guidance and support that was invaluable to my development as a scientist. I would first like to thank my mentor, Dr. John Tesmer, who gave me the intellectual freedom to pursue the research projects that excited me the most and encouraged me to think critically about my results. In addition to fostering a highly collaborative laboratory environment, Dr. Tesmer also demonstrated his commitment to his employees' happiness outside of work by arranging frequent Tesmer lab activities, which allowed me to turn my colleagues and mentors into close friends. I would also like to express my gratitude towards Dr. Janet Smith, who became my co-mentor in the middle of my graduate career and provided support as I finished my research projects.

I was fortunate to participate in a number of collaborative research projects, and I would like to acknowledge the scientists who contributed to the work presented in my thesis. Dr. Xin-Qiu Yao and Dr. Barry Grant offered their computational biology expertise that was instrumental in developing hypotheses about the mechanisms of G protein-coupled receptor kinase activation that I could then test in the Tesmer lab. Dr. Helen Waldschmidt led the design and synthesis of an impressive number of small molecule inhibitors that resulted in numerous publications and advanced our knowledge of selective kinase inhibitors and heart failure. Jessica Waninger assisted me with crystallization trials during my first year in the Tesmer lab that culminated in four co-crystal structures. Dr. Renee Bouley also contributed multiple co-crystal structures and substantial structural analysis to this project that improved our understanding of the mechanisms

of small molecule inhibitor selectivity. Rachel Rowlands designed and synthesized an additional library of small molecule inhibitors that allowed us to investigate covalently binding kinase inhibitors. Dr. Osvaldo Cruz-Rodriguez mentored me when I was a rotation student and frequently shared his vast knowledge about cell culture techniques, protein purification, and assay optimization. I am grateful to each of these colleagues for their contributions to my research projects, and I am fortunate to have developed friendships with each one. Although we did not collaborate directly, I would also like to acknowledge Dr. Kelly Manthei, Sumit Bandekar, and Dr. Louise Chang for contributing to my growth as a scientist and offering their friendship and support outside of lab.

I would also like to acknowledge Jen Bohn, who was an essential source of guidance and encouragement scientifically, as well as laughter and companionship both in and outside of the laboratory, and who I largely credit with my ability to persevere through some of the more difficult days of graduate school.

Finally, I would like to express my sincere gratitude to each of my family members, both those chosen for me and those I chose for myself. My brothers, Chase and Curt, have encouraged me to be resilient and to proceed through life's challenges with a lighthearted spirit. Both of my parents have offered their unwavering support, have trusted me to make my own choices, and have always been available to offer valuable advice. I would also like to thank Chris Hanson for supporting me during setbacks, celebrating my successes, and laughing with me every day.

Table of Contents

Acknowledgements	ii
List of Figures	viii
List of Tables	x
List of Abbreviations	xi
Abstract	xiii
Chapter 1: Introduction	1
1.1. Signal Transduction through G Protein-Coupled Receptors	1
1.2. Activation and Conformational Flexibility of GPCRs	3
1.3. GPCR Desensitization	4
1.4. The GPCR Kinase Families	6
1.5. Structural Motifs in the Activation of the AGC Kinase Superfamily	7
1.6. Regulatory Features of GRKs	9
1.7. Dysregulation of β -Adrenergic Receptors and GRKs in Heart Failure	10
1.8. Activation of GRKs	13
1.9. Summary and Research Goals	15
Chapter 2: Navigating the Conformational Landscapes of G Protein-Coupled Receptor Kinases during Allosteric Activation	17
Foreword	17
2.1. Introduction	17
2.2. Materials and Methods	19
2.2.1. Principal Component Analysis	19
2.2.2. Contact Map Analysis	20
2.2.3. Molecular Dynamics Simulations	20

2.2.4. Plasmid Preparation	21
2.2.5. Protein Expression and Purification	22
2.2.6. Radiometric Assays to Determine Steady-State Parameters	23
2.3. Results	24
2.3.1. Principal Component Analysis	24
2.3.2. Contact Map Analysis	26
2.3.3. Molecular Dynamics Simulations	27
2.3.4. Protein Expression and Purification	30
2.3.5. Radiometric Assays to Determine Steady-State <i>Parameters</i>	30
2.4. Discussion	32
Chapter 3: Steady-State Analysis of a Region of GRK2 Predicted to be involved in Activated GPCR Engagement	37
Foreword	37
3.1. Introduction	37
3.2. Materials and Methods	42
3.2.1. Plasmid Preparation	42
3.2.2. Protein Expression and Purification	42
3.2.3. Protein Concentration Normalization	43
3.2.4. Radiometric Assays to Determine Steady-State Parameters	44
3.3. Results	45
3.3.1. Purification of GRK2 Mutants Expressed in HEK293F Cells	45
3.3.2. GRK2 Concentration Normalization	46
3.3.3. GRK2 Michaelis-Menten Analysis	47
3.4. Discussion	49
Chapter 4: Structural and Functional Characterization of GRK2-Selective Small Molecule Inhibitors	51
4.1. Introduction	51
4.2. Structure-Based Design, Synthesis, and Biological Evaluation of Highly Selective and Potent GRK2 Inhibitors Based on GSK180736A	53
4.2.1. Foreword	53
4.2.2. Background	54

4.2.3. Materials and Methods	57
4.2.3.1. Library Construction	57
4.2.3.2. Pharmacological Assays	57
4.2.3.3. Plasmid Preparation and Insect Cell Expression of Bovine GRK2 and Human $G\beta\gamma$	58
4.2.3.4. Protein Purification	58
4.2.3.5. Crystallization and Data Processing	59
4.2.3.6. Mouse Cardiomyocyte Shortening Assays	60
4.2.4. Results	60
4.2.4.1. Structure-Activity Relationships of the GSK180736A Derivative Compounds	60
4.2.4.2. GRK2- $G\beta\gamma$ Co-crystallization with CCG215022, CCG224062, CCG224406, and CCG224411	62
4.2.4.3. Molecular Basis for GRK2 Potency and Selectivity by the GSK180736A Derivatives	66
4.2.4.4. Contractility in Mouse Cardiomyocytes with GSK180736A Derivatives	71
4.2.5. GSK180736A Derivatives Summary	72
4.3. Structure-Based Design, Synthesis, and Biological Evaluation of Highly Selective and Potent GRK2 Inhibitors Based on Paroxetine	74
4.3.1. Foreword	74
4.3.2. Background	75
4.3.3. Materials and Methods	75
4.3.3.1. Paroxetine Derivatives Library Construction	75
4.3.3.2. Pharmacological Assays	76
4.3.3.3. X-ray Structure Determination	76
4.3.3.4. Mouse Cardiomyocyte Shortening Assays	76
4.3.4. Results	76
4.3.4.1. Structure-Activity Relationships of the Paroxetine Derivative Compounds	76

4.3.4.2. GRK2-G β γ Co-crystal Structure Analysis with CCG211998, CCG222886, and CCG258208	79
4.3.4.3. Molecular Determinants of GRK2 Potency and Selectivity by the Paroxetine Derivatives	81
4.3.4.4. Mouse Cardiomyocyte Contractility Assays with Paroxetine Derivatives	84
4.3.4.5. Role of the Hinge Binding Moiety	85
4.3.5. Paroxetine Derivatives Summary	88
4.4. GRK2-Selective Inhibitor Conclusions	89
Chapter 5: Design and Pharmacological Characterization of Covalent GRK5-Selective Inhibitors	93
Foreword	93
5.1. Introduction	93
5.2. Materials and Methods	97
5.2.1. Homology Model and Virtual Screen	97
5.2.2. Pharmacological Assays	97
5.2.3. Intact and Tandem Mass Spectrometry	98
5.3. Results	98
5.3.1. Design, Construction, and Structure-Activity Relationships of an Initial Library of Covalent Inhibitors	98
5.3.2. Structure-Activity Relationships of Pyrrolopyrimidine Derivatives	101
5.3.3. Time Dependence of Inhibition for Lead Compounds	107
5.3.4. Intact and Tandem Mass Spectrometry on Top Compounds	108
5.4. Discussion	109
Chapter 6: Conclusions and Future Directions	111
References	118

List of Figures

Figure 1.1. G protein signaling through GPCRs	2
Figure 1.2. Structural transmembrane helix rearrangements between inactive- and active-state GPCRs	4
Figure 1.3. GPCR desensitization and internalization	5
Figure 1.4. GRK families and domain architecture	6
Figure 1.5. Active-state PKA	8
Figure 1.6. β AR signaling in cardiomyocytes	12
Figure 1.7. Model of a GPCR-GRK complex at the cell membrane	14
Figure 2.1. Domain architecture and structural arrangement of the GRK4 subfamily	19
Figure 2.2. PCA reveals distinct crystallographic conformers and collective motions connecting conformers	24
Figure 2.3. PCA of full-length GRKs	25
Figure 2.4. Residue contact and energy analyses focused on the RHD-large lobe interface identify potential residues involved in GRK activation	27
Figure 2.5. Select mutations disrupting domain interactions promote RHD opening and KD closure as revealed by MD simulations	28
Figure 2.6. Representative purification of GRK5 from <i>E. coli</i>	29
Figure 2.7. Disrupting the RHD-KD interface causes in vitro changes in steady-state parameters	31
Figure 2.8. Comparison of c-Src and GRK5	33
Figure 3.1. Comparison of GRK2 and GRK5 predicted GPCR engagement regions	41
Figure 3.2. Representative purification of bovine GRK2 from HEK293F cells	45
Figure 3.3. GRK2 concentration normalization	46
Figure 3.4. Michaelis-Menten analysis with variable [ATP]	47

Figure 3.5. Michaelis-Menten analysis with variable [rhodopsin]	48
Figure 4.1. GRK2-selective inhibitors	54
Figure 4.2. Structural models of GRK2-G $\beta\gamma$ in complex with the three lead compounds	55
Figure 4.3. Representative purifications of bovine GRK2 and human G $\beta\gamma$ -C68S used in crystallization trials	63
Figure 4.4. Co-crystal structures reveal that the inhibitors bind in the ATP-binding pocket in a similar conformation as the GSK180736A parent structure	65
Figure 4.5. Adaptive structural changes in the GRK2 P-loop	66
Figure 4.6. Structural determinants of inhibitor potency for GSK180736A derivative compounds	67
Figure 4.7. Structural differences in the hinge regions of PKA, GRK2, and GRK5	67
Figure 4.8. Comparison of GRK2 and GRK5 hydrophobic subsites when bound to CCG215022	68
Figure 4.9. Molecular origins of selectivity for CCG224406	69
Figure 4.10. Cardiomyocyte contractility of GSK180736A derivatives	71
Figure 4.11. GRK2-G $\beta\gamma$ -inhibitor co-crystal structures with paroxetine derivative compounds	80
Figure 4.12. Cardiomyocyte contractility of paroxetine-derivative compounds	84
Figure 4.13. CCG224061 is a hybrid between GSK180736A and paroxetine	85
Figure 4.14. PC analysis of GRK and PKA structures	87
Figure 4.15. Comparison of GRK2 when indazole or benzodioxole hinge-binding compounds are bound	88
Figure 5.1. An AST-loop cysteine is conserved in the GRK4 subfamily	96
Figure 5.2. Lead compounds with modest GRK5 potency share a common pyrrolopyrimidine core	98
Figure 5.3. GRK1-GSK2163632A shows the pyrrolopyrimidine interactions with the hinge	99
Figure 5.4. Cys474 is oriented towards the GSK2163632A tetrahydroquinoline	100
Figure 5.5. <i>Para</i> substituents may collide with the GRK2 AST-loop	104
Figure 5.6. <i>Para</i> -substituted compounds docked into the GRK5/GRK6 homology model	105
Figure 5.7. Time-dependent inhibition of CCG265328 and CCG265507.....	108

List of Tables

Table 2.1. Comparison of steady-state parameters	31
Table 4.1. Inhibitory activity of the GSK180736A derivative compounds	61
Table 4.2. Refinement statistics for GRK2–G $\beta\gamma$ ·GSK180736A derivative complexes	64
Table 4.3. Inhibitory activity of the paroxetine derivative compounds	77
Table 4.4. Refinement statistics of GRK2–G $\beta\gamma$ ·benzodioxole derivative complexes	81
Table 4.5. SAR of the hinge binding moiety	86
Table 5.1. Inhibitory activity of <i>meta</i> - and <i>para</i> -pyrrolopyrimidine derivatives	102
Table 5.2. Inhibitory activity of <i>para</i> -pyrimidine derivatives	107

List of Abbreviations

AGC kinase: kinase superfamily named for representative members: protein kinase A, protein kinase G, protein kinase C
 α N: extreme N-terminal helix conserved in GRKs
AST: active site tether
AMP: adenosine monophosphate
ATP: adenosine triphosphate
 β AR, β_1 AR, β_2 AR: β -adrenergic receptor, β_1 -adrenergic receptor, β_2 -adrenergic receptor
 β ARKct: β -adrenergic receptor kinase C-terminal peptide
BI: Boehringer Ingelheim
 β -ME: 2-mercaptoethanol
BSA: buried surface area
cAMP: cyclic AMP
CCG: Center for Chemical Genomics
CLBD: C-terminal lipid binding domain
C-lobe: C-terminal kinase domain lobe
CT: C-terminus
Cys: cysteine
DFG-loop: loop defined by Asp (D) – Phe (F) – Gly (G)
DMSO: dimethylsulfoxide
DTT: dithiothreitol
ECL: extracellular loop
Epi: epinephrine
EPK: eukaryotic protein kinase
FDA: Food and Drug Administration
GAP: GTPase Activating Protein
GPCR: G protein-coupled receptor
GRK: G protein-coupled receptor kinase
GSK: GlaxoSmithKline
H-bond: hydrogen bond
HDAC5: histone deacetylase 5
HEK293F: human embryonic kidney 293 cells, FreeStyle
IC₅₀: half maximal inhibition concentration
ICL: intracellular loop
IPTG: isopropyl β -D-1-thiogalactopyranoside
 k_{cat} : rate constant for catalysis, turnover number
KD: kinase domain

K_d : dissociation constant
 K_i : inhibitory constant
 K_m : Michaelis constant
 k_{off} : rate constant for dissociation
MD: molecular dynamics
MS: mass spectrometry
NLBD: N-terminal lipid binding domain
N-lobe: N-terminal kinase domain lobe
Nor: norepinephrine
NT: N-terminus, N-terminal
PC1-2: principal component 1, principal component 2
PCA: principal component analysis
PDB: Protein Data Bank
PH: pleckstrin homology
PIP₂: phosphatidylinositol 4,5-bisphosphate
PKA: cAMP-dependent protein kinase, protein kinase A
PKC: protein kinase C
PKG: cGMP-dependent protein kinase, protein kinase G
P-loop: kinase phosphate-binding loop
PMSF: phenylmethylsulfonyl fluoride
rcf relative centrifugal force
RGS: Regulator of G protein Signaling
RH: RGS Homology
Rho: rhodopsin
rmsd: root-mean-square deviation
ROCK1: Rho-associated Coiled-Coil Containing Protein Kinase 1
ROS: rod outer segment
SAR: structure-activity relationship
SDS-PAGE: sodium dodecyl sulfate polyacrylamide gel electrophoresis
Ser: serine
SSRI: selective serotonin reuptake inhibitor
TAC: transverse aortic constriction
Thr: threonine
TM1-7: GPCR transmembrane helix 1-7
 V_{max} : maximum rate of reaction
wt: wild-type

Abstract

Cellular signaling through G protein-coupled receptors (GPCRs) is essential for most physiological processes, ranging from vision, taste, and smell to immune, neurological, and cardiovascular functions. In order to remain prepared to receive future signals and to protect the cell from the toxic effects of prolonged signaling, the duration and strength of GPCR-mediated signal transduction pathways must be tightly regulated. GPCR kinases (GRKs) drive signal termination by selectively recognizing and phosphorylating the C-terminal tails and intracellular loops of GPCRs that are actively signaling. GRK-mediated phosphorylation leads to the recruitment of arrestin, decoupling from G proteins, and GPCR internalization into the cytosol. The mechanism of GRK activation is complex and not fully understood. It is well-established that activated GPCRs allosterically increase GRK activity 100- to 1000-fold, but many questions remain about the structural determinants of GRK engagement with GPCRs and how this interaction stabilizes a fully activated kinase domain conformation.

The mechanisms underlying these processes are important to understand because aberrant signal transduction is commonly found in human diseases. In heart failure, compromised β -adrenergic receptor (β AR) signaling and elevated levels of GRK2 and 5 lead to decreased cardiac output even in the presence of high circulating levels of the signaling molecules, adrenaline and noradrenaline. Given the elevated expression and activity of GRK2 and 5 in heart failure, GRK inhibition has exciting potential for the treatment of heart failure. In addition, there is a need for

GRK-selective chemical probes that can be used to elucidate the distinct roles that GRK2 and 5 play in the progression of heart failure.

With the overall goal of determining structural features that contribute to GRK activation and small molecule inhibitor specificity in the ATP-binding site, combined biochemical, pharmacological, and structural methods were utilized to probe GRK function. To assess GRK activation, steady-state kinetic analyses centered around 1) a region on GRK2 predicted to be involved in GPCR engagement and 2) an intramolecular interface in GRKs identified using principal component analysis of all available GRK crystal structures were performed. Results from these experiments suggest that GPCR docking sites may differ among the GRKs, and an intramolecular GRK interface distal to the active site contributes to stabilization of the activated kinase domain conformation in what we interpret to be an intermediate state on the path to full GPCR-mediated GRK activation. To understand the molecular determinants of small molecule inhibitor specificity, several GRK2– $G\beta\gamma$ -inhibitor complexes were crystallized and structurally characterized. Structure-activity relationships were assessed for two libraries of GRK2-selective inhibitors and one library of GRK5-selective inhibitors. These studies resulted in highly potent and selective GRK2 inhibitors and covalent GRK5 inhibitors, and the structural analyses indicate subtle but significant differences in the ATP-binding sites of GRK2 and 5 that can be utilized in future rounds of GRK inhibitor development and optimization.

Chapter 1: Introduction

1.1. Signal Transduction through G Protein-Coupled Receptors

G protein-coupled receptors (GPCRs) make up the largest genetic superfamily found in mammals, with over 800 known human GPCRs. GPCRs are further divided into five major families related by sequence homology (1-2), and by far the best characterized and largest family, with over 700 known receptors, is the Class A (or Rhodopsin-like) family of GPCRs (3). These seven transmembrane-spanning proteins at the cell membrane are essential for most physiological processes, ranging from vision, taste, and smell, to immune, neurological, and cardiovascular functions (4). Not surprisingly, then, dysregulation of GPCR-mediated pathways is associated with a large variety of human diseases, ranging from night-blindness to multiple cancers and heart failure. Indeed, more than 40% of clinically approved drugs target GPCRs, making these receptors the largest drug target for human disease (5).

GPCRs translate extracellular signals that can come in the form of neurohormones, photons of light, or peptides into intracellular responses. This ability to transduce a signal from outside the cell to inside the cell is no small feat given the 4 nm thickness of the cell membrane (6). At the molecular level, signal transduction across the membrane begins with binding of an extracellular signaling molecule, or agonist, to the extracellular side of a GPCR. Agonist binding causes a conformational change in the GPCR that is recognized inside the cell by inactive, GDP-bound heterotrimeric G proteins ($G\alpha\beta\gamma$) (4). Binding to activated GPCRs causes the $G\alpha$ subunit

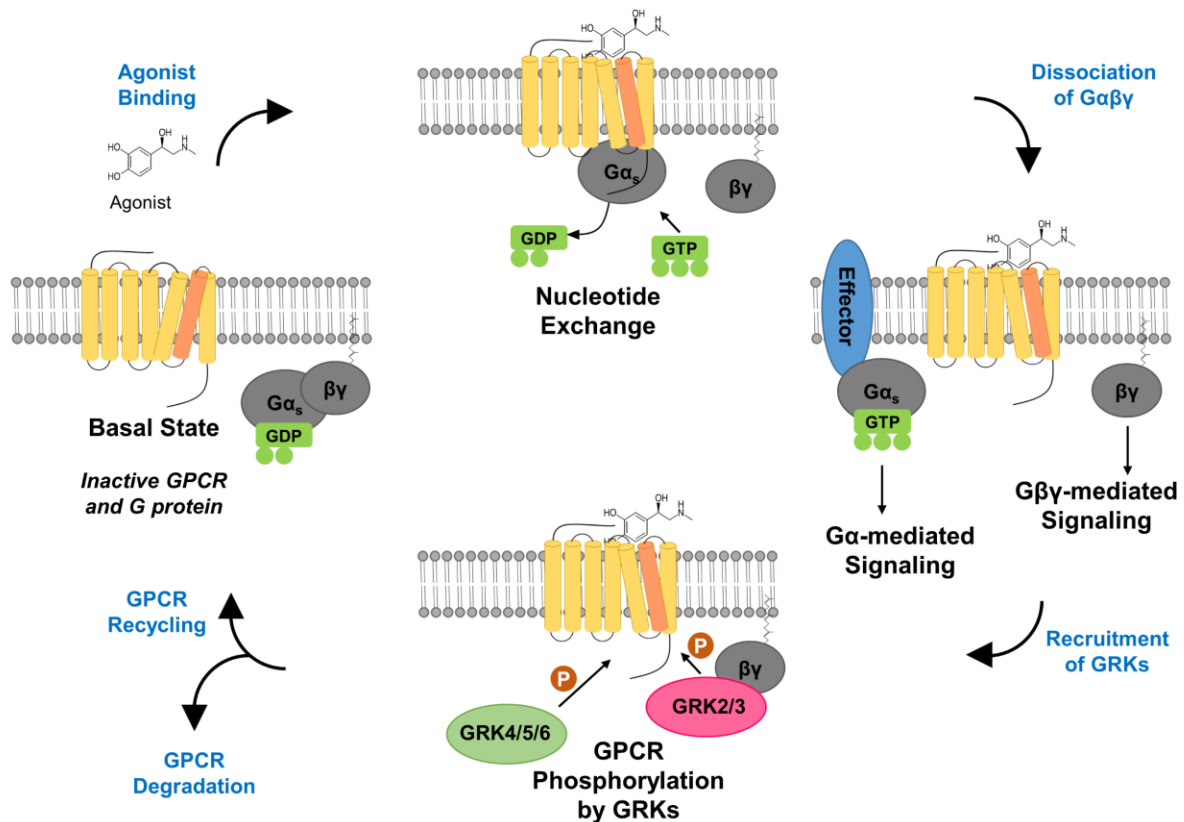


Figure 1.1. G protein signaling through GPCRs. Signal transduction pathways begin with binding of an extracellular signaling molecule, or agonist, to an inactive GPCR. Agonist binding causes a conformational change in the GPCR, reflected here as a shift in transmembrane helix 6 (TM6, orange cylinder). Subsequent binding and nucleotide exchange on heterotrimeric G proteins causes their activation and dissociation into $G\alpha$ and $G\beta\gamma$ subunits, which can each modulate signaling pathways through downstream effector proteins. Active-state GPCRs are selectively recognized and phosphorylated by GRKs at their C-terminal tails and intracellular loops, leading to internalization into endosomes (not shown). GPCRs can then continue signaling through G protein-independent pathways (not shown), be tagged for degradation, or returned to their basal state and recycled back to the cell membrane where they can receive future extracellular signals.

to release GDP, bind the readily available cytosolic GTP, and dissociate from the $G\beta\gamma$ subunits.

Activated GTP-bound $G\alpha$ and liberated $G\beta\gamma$ subunits can then modulate the activity of different effector proteins, such as phospholipase $C\beta$ and adenylyl cyclase, to increase the levels of second messenger molecules such as inositol triphosphate, diacylglycerol, Ca^{2+} , and cyclic AMP (cAMP), among others. These second messengers then regulate the activities of a wide variety of other intracellular signaling proteins, causing amplification and propagation of the signal that began with a single agonist binding event at a GPCR (7-8) (**Figure 1.1**).

Although this general mechanism of signal transduction is common to GPCRs, a wide diversity of physiological outcomes are possible. Between over 800 known GPCRs with differing cellular expression profiles, four families of heterotrimeric G proteins (G_s , G_i , G_q , $G_{12/13}$) that signal through different effectors, and the propensity for crosstalk between different signaling pathways within a single cell, the complexity of these processes and their outcomes at the tissue and organ levels can begin to be appreciated. In addition, GPCRs are highly dynamic proteins that exist in an ensemble of conformational states that can be modulated by different ligand (agonist, antagonist, inverse agonist, and biased agonist) molecules (9-12). While agonists stabilize an ensemble of conformations that are more active, and inverse agonists stabilize an ensemble of states that are less active, it is important to recognize that a two-state on/off model does not accurately describe GPCR signaling.

1.2. Activation and Conformational Flexibility of GPCRs

The determination of several important GPCR crystal structures led to the first models of GPCRs in what is believed to be a fully active state (notably (13-17)), which requires both binding of an extracellular agonist and an intracellular G protein or G protein mimetic. Crystal structures of GPCRs show a common core comprised of seven transmembrane helices (TM1-7), which are connected by both the highly variable extracellular loops (ECL1, 2, and 3) that face the extracellular space (1) and intracellular loops (ICL1, 2, and 3) directed towards the cytosol, with their N- and C-termini directed towards the extracellular space and cytosol, respectively (4). Of note, ICL3 demonstrates high variability in sequence and length and is involved in interactions with the intracellular binding partners of GPCRs (5). Structural characterization of multiple GPCRs (notably rhodopsin and the β_2 -adrenergic receptor) in different ligand states

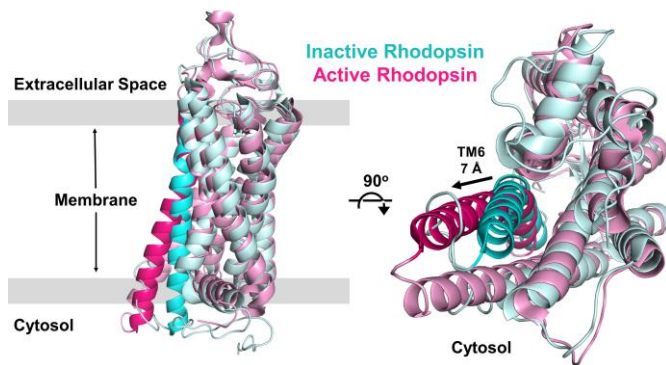


Figure 1.2. Structural transmembrane helix rearrangements between inactive- and active-state GPCRs. Inactive rhodopsin (PDB ID 1U19, light cyan) and active rhodopsin (PDB ID 3DQB, light pink) (14) are overlaid, with their TM6 helices colored in cyan (inactive) and magenta (active). Left: GPCR activation is associated with a 7 Å shift of TM6 away from the central GPCR axis. Right: View from the cytosol shows the increased binding surface area revealed upon GPCR activation that is recognized by the agonist-dependent intracellular binding partners, G proteins and GRKs.

demonstrates what appears to be a common mechanism for Class A GPCR activation, whereby a 7-14 Å swing of transmembrane helix 6 (TM6) away from the central axis along with smaller structural rearrangements in TM3 and TM5 reveals access to a binding pocket on the intracellular side of the GPCR (3,

12) (**Figure 1.2**). Importantly, with the exception of activated rhodopsin, maximal displacements of these intracellular GPCR helices are only stabilized in crystal structures when either $G\alpha$ (17) or a $G\alpha$ binding mimetic (e.g. a nanobody selective for the activated GPCR (16)) is bound, suggesting that the fully active GPCR state is only reached in the cell when its intracellular binding partner is present.

1.3. GPCR Desensitization

To remain poised for future signals and to protect the cell from the toxic effects of prolonged signaling, GPCR-mediated signaling is terminated in a tightly regulated manner by GPCR kinases (GRKs) (19). Much like GDP-bound heterotrimeric G proteins, GRKs specifically recognize activated, agonist-bound GPCRs, perhaps through the intracellular GPCR binding pocket that is revealed upon the agonist-driven structural rearrangements in TM3, TM5, and TM6 (20-21). Phosphorylation of serines and threonines in the C-terminal tails and intracellular loops of activated GPCRs by GRKs leads to the recruitment of arrestin, which

occludes G protein binding and terminates the signal from that receptor. Arrestin binding also targets the receptors for endocytosis in clathrin-coated pits, where they can either continue signaling through G protein-independent signaling pathways, undergo ubiquitination and lysosomal degradation, or be recycled back to the cell membrane (22-23) (**Figure 1.3**).

The collective events that lead to G protein uncoupling and a decrease in receptor density at the cell membrane, termed GPCR desensitization, are an essential aspect of signal transduction regulation. Although second messenger-dependent kinases such as protein kinase A and C (PKA, PKC) also phosphorylate GPCRs regardless of whether they are in an active state (heterologous desensitization) (24), the rapid and selective GRK-mediated phosphorylation of activated receptors (homologous desensitization) is the predominant mechanism for controlled signal termination (21). The mechanisms underlying GRK-mediated desensitization are important to understand because aberrant signal transduction is commonly found in disease. For example, increased GRK expression and activity in the heart is linked to congestive heart failure (described in more detail below).

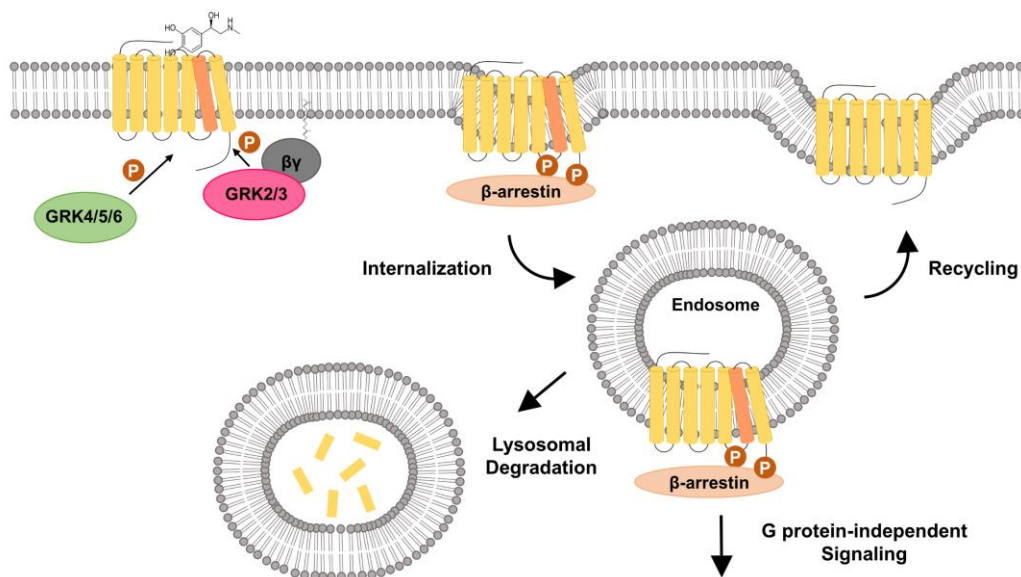


Figure 1.3. GPCR desensitization and internalization. GRKs drive GPCR desensitization by phosphorylating the C-terminal tails and ICLs of activated GPCRs, which leads to the recruitment of arrestin and subsequent internalization into cytosolic endosomes. In endosomes, GPCRs can either continue signaling through G protein-dependent or G protein-independent pathways, be tagged for lysosomal degradation, or be recycled to the cell membrane to continue signaling.

1.4. The GPCR Kinase Families

The seven human GRKs are subdivided into three families based on sequence homology, and they most obviously differ in their C-terminal extensions which determine their mode of membrane localization (25) (**Figure 1.4A**). The GRK1 subfamily members (GRK1 and 7) are either farnesylated (GRK1) or geranylgeranylated (GRK7) at their C-terminal CAAX motifs, and these lipidation modifications drive them to the cell membrane. The GRK4 subfamily members (GRK4, 5, and 6) can be reversibly palmitoylated, and they also contain a positively charged

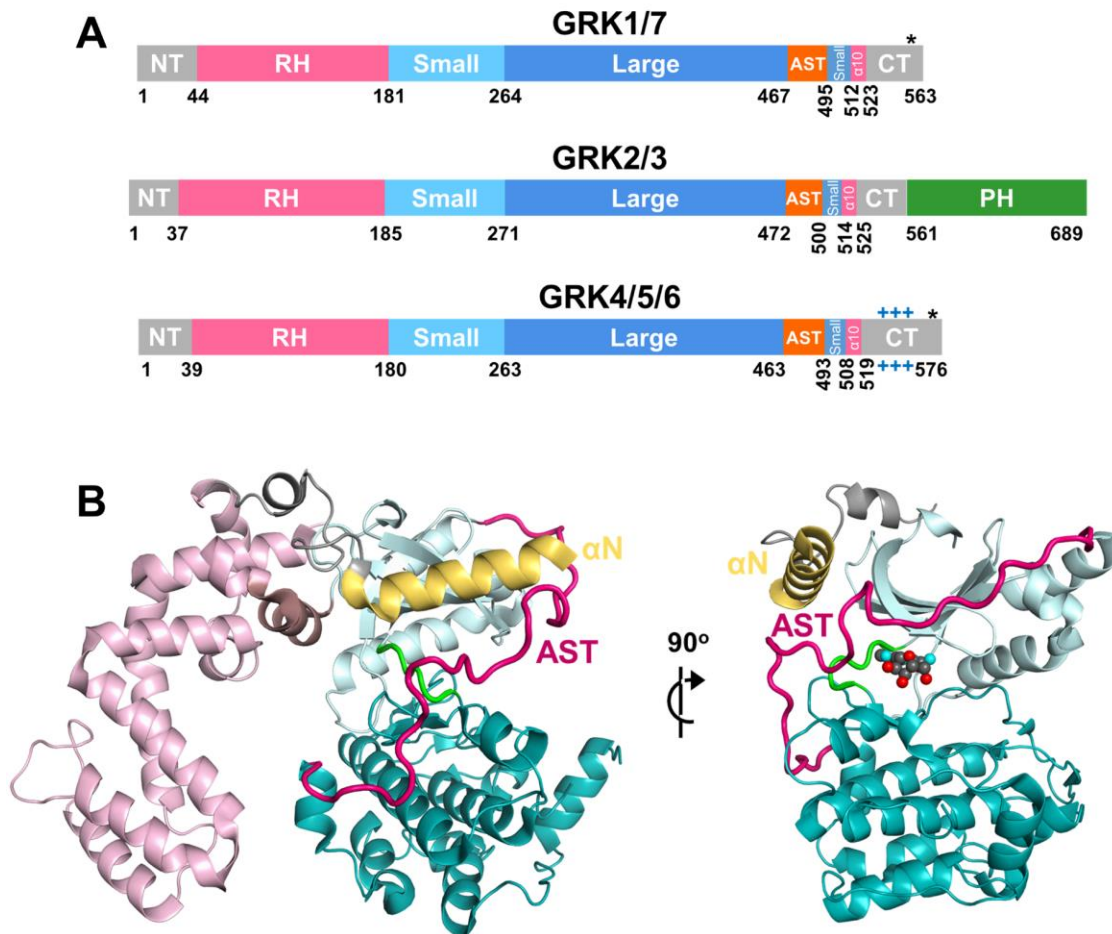


Figure 1.4. GRK families and domain architecture. **A**) The seven human GRKs are subdivided into the GRK1 (1 and 7), 2 (2 and 3), and 4 (4, 5, and 6) subfamilies. All GRKs contain a common kinase domain core comprised of a small and large lobe that are inserted into a loop in a Regulator of G protein Signaling Homology (RH) domain. GRKs are the most variable in their C-terminal extension, which dictate their mode of membrane localization. GRK1 and 4 subfamily members contain lipidation modifications (denoted by *). GRK4 subfamily members also contain a positively charged surface on an amphipathic helix that drives association with negatively charged phosphate head groups of the membrane. GRK2 subfamily members are recruited to the membrane by interaction with membrane-associated $G\beta\gamma$ through their pleckstrin homology (PH) domain. **B**) GRK6 (PDB ID 3NYN) (37) shows the structural arrangement of the conserved GRK core. RH domain, light pink; kinase domain small lobe (light cyan) and large lobe (dark teal); α N-terminus, gold; AST-loop, magenta.

patch on a C-terminal amphipathic helix that drives stable association with the negatively charged membrane phospholipid head groups. The GRK2 subfamily (GRK2 and 3) is unique in that its members are recruited to the membrane by a C-terminal pleckstrin homology (PH) domain that associates with membrane-bound $G\beta\gamma$ subunits that are liberated from heterotrimeric G proteins after agonist-dependent activation. GRKs also interact with phospholipids, although the question remains whether phospholipid binding plays a role in the allosteric activation of GRKs or if it predominantly drives GRK membrane localization (26–30).

In addition to differences in membrane localization, GRKs gain some GPCR specificity through differences in cellular expression. GRK1 and 7, the visual GRKs, are exclusively expressed in the rod and cone cells in the retina where they phosphorylate the GPCRs, rhodopsin and cone opsin. GRK3 is predominantly expressed in olfactory neurons, and GRK4 is expressed in the testes. GRK2, 5, and 6 are ubiquitously expressed, and thus interact with a wider variety of substrates than the other GRKs (24, 31).

1.5. Structural Motifs in the Activation of the AGC Kinase Superfamily

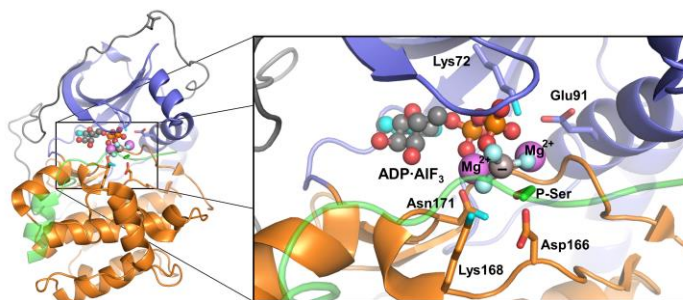
GRKs are members of the broader superfamily of AGC kinases, a collection of over 60 Ser/Thr kinases related by sequence homology to the catalytic domains of cAMP-dependent protein kinase (PKA), cGMP-dependent protein kinase (PKG), and protein kinase C (PKC) (32). The biological importance of AGC kinases is in part evidenced by their high evolutionary conservation and presence in most eukaryotes. AGC kinases differ from the broader superfamily of eukaryotic protein kinases (EPKs) with a conserved C-terminal extension involved in regulation of kinase activation and localization (33, 34). Within this C-terminal extension is the

active site tether (AST), a loop that is involved in nucleotide entry and exit from the kinase active site and is thought to play a role in GRK activation.

Despite divergence in their regulatory features, all AGC kinases share a common catalytic kinase domain fold comprised of a small and large lobe (N-lobe and C-lobe, respectively), with the ATP-binding site at their interface and recurring structural motifs in both lobes (35). Notably, the small lobe contains the P-loop (also called the glycine-rich loop) which contributes residues that orient the phosphates on a bound ATP molecule, the α C-helix which borders the active site, a lysine essential for orienting ATP, and the hinge that bridges the small and large lobes. The large lobe contains the DFG motif (for Asp-Phe-Gly, or Asp-Leu-Gly in GRKs) in the activation loop, in addition to several other active site residues essential for orienting ATP and the substrate serine or threonine to be phosphorylated (32). There is great structural variability among inactive AGC kinase structures; however, activation of AGC kinases brings important residues contributed from both the small and large lobes into

a fully activated conformation that is highly structurally conserved across the entire superfamily (**Figure 1.5**). The transition state-

mimic complex of PKA (36) is widely accepted to be the best model of a fully activated AGC



Active-State Protein Kinase A

Figure 1.5. Active-state PKA. The transition state mimic co-crystal structure of PKA (PDB ID 1L3R) (36) shows the AGC kinase domain in a fully activated conformation and serves as a reference model for the structural rearrangements presumed to occur in GRK activation. Alignment of residues from the small and large lobes and full closure of the kinase domain around a bound nucleotide are essential for phosphotransfer.

kinase and thus has been used as a reference to determine the degree of activation observed in other AGC kinase structural models, including GRKs. Most AGC kinases are activated by phosphorylation of typically three conserved motifs: the activation loop, the turn motif, and the

hydrophobic motif. Phosphorylation at these sites causes structural rearrangements, notably in the α C-helix and activation loop, which bring the active site residues into an optimal position for catalyzing phosphotransfer onto the serine or threonine of the substrate peptide. Interestingly, GRKs only retain the turn motif, and thus GRK activity is more dependent on its highly selective interactions with activated GPCRs.

1.6. Regulatory Features of GRKs

In addition to the common bilobal kinase domain fold, GRKs have additional structural features that contribute to their regulation (25) (**Figure 1.4A**). The first ~30 residues make up the N-terminus, which is conserved in GRKs but is not found in other AGC kinases. The N-terminus is disordered in most structural models, indicating its high degree of flexibility, but was found to form an α -helix and lay across the small lobe in the first crystal structure where the N-terminus was fully resolved (37) (**Figure 1.4B**). It has long been proposed to interact with activated GPCRs, and either N-terminal truncations or mutations are sufficient to eliminate GRK phosphorylation of receptors while maintaining their ability to phosphorylate soluble peptide substrates (although with impaired kinetics) (25). GRKs also possess a Regulator of G protein Signaling, or RGS, homology domain (RH domain). RGS proteins typically bind to G proteins, where they exhibit GTPase Accelerating Protein (GAP) activity that returns G proteins to their inactive, GDP-bound state (38). Only GRK2 has been shown to bind to a G protein ($G\alpha_q$), and it does not retain its GAP activity in this interaction (39-40). In addition, the entire kinase domain is inserted into a loop in the RH domain. As such, the RH domain has been suggested to maintain the kinase domain in a semi-active conformation, offering a possible explanation for why GRKs have not evolved to contain the phosphorylation motifs that are highly conserved in other AGC

kinases and are required for their activation (41-42). The tightly linked structural arrangement of the RH domain and kinase domain, along with the potential for the RH domain to serve as a protein-protein interaction interface for other signaling proteins like $G\alpha$, has implicated the RH domain in the regulation of GRK activation, perhaps through an allosteric mechanism. Finally, GRKs contain a conserved AST-loop that leads to variable C-terminal regions involved in membrane localization as discussed above. The AST-loop is remarkably conserved among GRKs, with the most obvious variability coming from the slightly longer and C-terminally more acidic AST-loop found in GRK2 and 3. As in other AGC kinases, the GRK AST-loop is proposed to be involved in regulating nucleotide entry and exit (32, 34). In GRKs, it has also been proposed to bind to receptors where it either plays a role in the allosteric activation of the kinase domain, conferring specificity for GPCR binding, or some combination of the two (25, 37).

1.7. Dysregulation of β -Adrenergic Receptors and GRKs in Heart Failure

Contractility of the heart is primarily driven by the β -adrenergic receptors (β ARs), and particularly the β_1 AR. In the normally functioning heart, increased circulation of the catecholamines epinephrine (adrenaline) and norepinephrine (noradrenaline) bind to and activate β ARs at the cardiomyocyte cell membrane. These agonist-bound β ARs then activate the G protein, $G\alpha_s$, which stimulates the activity of the effector, adenylyl cyclase, leading to an increase in cyclic AMP (cAMP). Binding of cAMP to the regulatory subunits of PKA causes the release and activation of the catalytic subunits of PKA, which can then regulate signaling pathways that result in increased intracellular Ca^{2+} levels and ultimately heart contractility (43-46). GRK2 and GRK5 are the most abundant GRKs in the heart, and they rapidly phosphorylate

activated β ARs, leading to the heart's desensitization to circulating catecholamines. In addition, GRK5 has the unique ability among GRKs to translocate to the nucleus in a Ca^{2+} -dependent manner, where it can phosphorylate histone deacetylase 5 (HDAC5) which regulates the expression of cardiac hypertrophy genes. Desensitization and hypertrophy are initially beneficial as a short-term stress response (e.g. during exercise), but become pathological when prolonged in response to continuous cardiac stress (e.g. valve dysfunction or hypertension) (47-50).

During heart failure, prolonged release of catecholamines from the adrenal medulla are circulated through the bloodstream in an attempt to compensate for decreased cardiac output (51, 52). This long-term sensory overdrive has toxic effects in the heart and leads to both decreased expression of β ARs and increased expression of GRK2 and 5 (53). Increased GRK2 and 5 activity causes desensitization and internalization of β ARs, which exacerbates the already poor signaling by decreasing the density of β ARs available at the cell surface. Similarly, the stress-induced gene regulation activity of GRK5 increases the expression of hypertrophic genes, which leads to pathological enlargement of the heart that ultimately results in reduced heart chamber size and a compromised ability to pump blood to the body (**Figure 1.6**).

Mouse models of heart failure examining the effects of GRK knockout, overexpression, and small molecule or peptide inhibition have demonstrated that targeting GRKs has promising therapeutic potential for treating heart failure. While homozygous GRK2 knockout is embryonic lethal in mice, cardiac-specific GRK2 knockdown prevents the progression of heart failure and maintains normal β AR signaling in both control and post-myocardial infarction mice (54). Furthermore, GRK2 gene ablation post-myocardial infarction reverses the pathological remodeling of the heart and may even increase cardiac function (55). Evidence for the

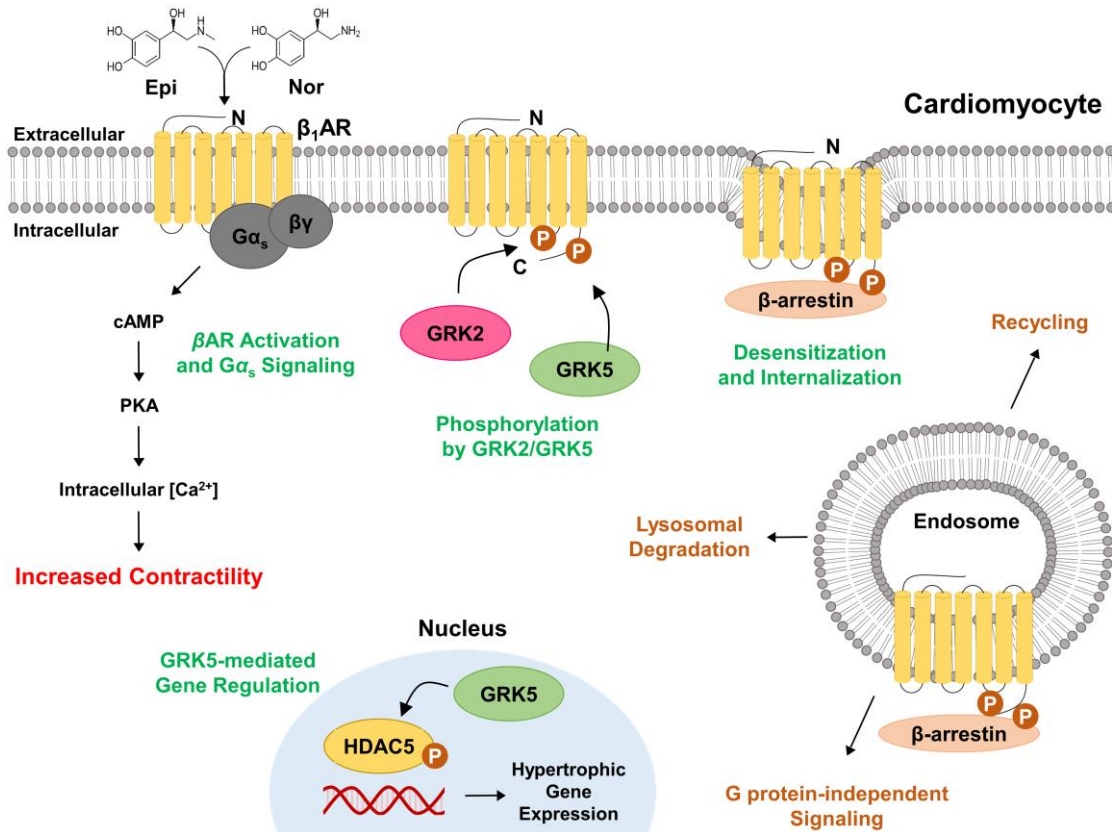


Figure 1.6. β AR signaling in cardiomyocytes. Binding of the agonists, epinephrine (Epi) or norepinephrine (Nor) to the β ARs initiate signaling through $G\alpha_s$, resulting in increased cAMP, activation of PKA, and ultimately increased heart contractility. Phosphorylation by GRK2 and 5 leads to β -arrestin-dependent internalization. During prolonged stress, GRK5 translocates into the nucleus in a Ca^{2+} -CaM-dependent mechanism where it phosphorylates HDAC5 and turns on expression of maladaptive hypertrophic genes.

cardioprotective effects of GRK2 inhibition came from transgenic mice that co-express a peptide inhibitor of GRK2 in cardiomyocytes (56). This β ARKct peptide (for β -adrenergic receptor kinase C-terminus) is derived from the C-terminus of GRK2, including parts of the PH domain that contain the binding elements for $G\beta\gamma$ binding. β ARKct binds to $G\beta\gamma$ and is thought to inhibit GRK2 activity by sequestering free $G\beta\gamma$ subunits, thus preventing the $G\beta\gamma$ -mediated GRK2 translocation to the membrane. Transgenic mice expressing β ARKct in cardiomyocytes have increased baseline contractility, and co-expressing β ARKct with overexpressed GRK2 prevents the β AR dysfunctions associated with increased GRK2 activity. Similarly, transgenic overexpression of GRK2 in vasculature was sufficient to decrease β AR signaling (57). These studies suggest that inhibition of GRK2 has the overall effect of increasing β AR signaling, most

likely by decreasing β AR internalization and increasing the β AR density at the cell membrane, but the inhibition of $G\beta\gamma$ signaling in general given the $G\beta\gamma$ sequestration by β ARKct may also play an important role. Better proof for the direct cardioprotective effects of GRK2 inhibition was provided by the demonstration that the small molecule GRK2 inhibitor, paroxetine, reverses β AR dysfunction in isolated cardiomyocytes (58) and maladaptive heart remodeling after myocardial infarction (59). GRK5 is not as well characterized as GRK2, but studies suggest that inhibition of GRK5 may also be cardioprotective (60). Homozygous GRK5 knockout mice are viable and have no basal cardiac phenotype, but show decreased hypertrophy after pressure-overload-induced heart failure is caused by transverse aortic constriction (TAC) surgery (61). In summary, the use of mouse models have proven the importance of GRK2 and GRK5 in the progression of heart failure, and indicate the therapeutic potential that inhibition of GRK2, GRK5, or both has for treating this devastating disease.

1.8. Activation of GRKs

The mechanisms underlying receptor-mediated GRK activation are complex and not fully understood. Membrane localization and allosteric activation by GPCRs play an important role in GRK function (62). Structural analysis, kinetic experiments, and comparison with active structures of PKA suggests that GRK activation at the very least involves ordering of the N-terminal helix, ordering of the AST-loop, phospholipid binding in some subfamilies, and kinase domain closure (37, 63-67). These hypotheses have been difficult to probe structurally because most GRK crystal structures are trapped in open, inactive conformations where the small and large lobes are not fully closed and the N-terminus and AST-loop are disordered. The GRK6·sangivamycin complex (PDB 3NYN) (37) was the first to resolve a GRK in what is

thought to be close to an active conformation, where the full N-terminal helix and AST-loop are ordered (**Figure 1.4B**). Recent structures of GRK5 in complex with sangivamycin (PDB 4TNB) and AMP-PNP (PDB 4TND) (68) also feature well-ordered AST-loops, but their kinase domains are not fully closed and their AST-loops do not follow the expected trajectory. Instead the loops are involved in extensive protein-protein interactions in the crystal lattice. Even with several fully resolved GRK structures now available, the structural determinants of GPCR engagement

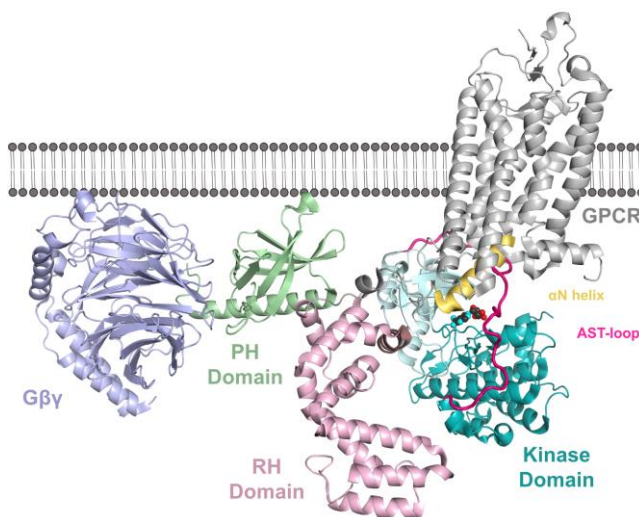


Figure 1.7. Model of a GPCR-GRK complex at the cell membrane. A composite model of GRK2 (PDB ID 4PNK) (104), with the fully ordered α N-helix (gold) and AST-loop (magenta) from GRK6 (3NYN) (37) in complex with activated rhodopsin (PDB ID 3DQB) (14) highlights the predicted structural determinants of membrane recruitment and GPCR engagement. The model was generated by aligning the GRK6 α N with the $G\alpha$ helix that was co-crystallized in this structural model of rhodopsin.

on GRKs are poorly understood.

We suggest a model where the GRK N-terminus docks into the GPCR binding pocket revealed by TM6 movement upon agonist binding, analogous to the interaction of $G\alpha$ subunits with this region through their C-terminal helix. Additional interactions from the GRK AST-loop and surfaces on the small lobe may interact specifically with activated GPCRs and help to

stabilize the kinase domain in a fully activated conformation, thus contributing to the allosteric activation of GRKs (25, 37, 63) (**Figure 1.7**). Differences in this proposed docking site within the GRK family may confer specificity for different features of GPCRs, particularly in intracellular loop 3 (ICL3) which is highly divergent in length and sequence among GPCRs and is known to interact with GRKs (5). This model is consistent with decades of structural, biochemical, and biophysical work within the field, but might only be resolved by a high

resolution structural model of a GPCR-GRK complex. The dynamic nature of both GPCRs and GRKs, along with the complicating technical factor of being a membrane-embedded complex, have prevented crystallization of a GPCR-GRK complex. With technological advances in membrane protein crystallography and cryo-electron microscopy, it is exciting to consider that a high resolution GPCR-GRK complex is on the horizon.

1.9. Summary and Research Goals

Appropriately regulated GPCR-mediated signal transduction is essential for a wide variety of biological processes, and dysregulation of these pathways is prevalent in human diseases such as heart failure. GRKs orchestrate the homologous desensitization of GPCRs by selectively phosphorylating activated receptors at their C-terminal tails and intracellular loops. In addition to binding selectively to agonist-bound receptors, GRKs are allosterically activated by this interaction, with a 100- to 1000-fold increase in kinase activity upon GPCR engagement. The structural determinants for this allosteric activation are poorly understood despite the availability of over 41 GRK crystal structures in the Protein Data Bank. The molecular mechanisms of GRK activation are particularly important to understand given the clear roles of GRK2 and GRK5 in the progression of heart failure, and the therapeutic benefit of inhibiting one or both of these kinases. Designing inhibitors that target either the inactive or active kinase conformation may be beneficial for conferring selectivity and potency to different GRKs, especially in light of the high structural conservation of the ATP-binding site. These gaps in the field led me to develop my overall goal of determining what structural features contribute to GRK activation and small molecule inhibitor selectivity. In the following chapters, I present the biochemical, computational, and pharmacological assessment of GRK structure and function in a

variety of collaborative projects that have progressed our understanding of these particular questions. Chapters 2 and 3 discuss the structural determinants of GRK activation using biochemical methods, and Chapters 4 and 5 address the development, structural characterization, and biochemical evaluation of GRK2- and GRK5- selective inhibitors. Finally, I conclude by offering my insight into the most pressing future issues to be addressed in GRK research.

Chapter 2: Navigating the Conformational Landscapes of G Protein-Coupled Receptor Kinases during Allosteric Activation¹

Foreword

Ideas and conclusions presented in Chapter 2 are published in the *Journal of Biological Chemistry* (69), including selected sections and figures that are copied verbatim. The publication was written with equal contributions from Dr. Xin-Qiu Yao and me, along with Dr. Barry Grant and Dr. John Tesmer. Xin-Qiu Yao in the Departments of Computational Medicine and Bioinformatics and the University of Michigan Medical School performed the principal component analysis, contact map analysis, and molecular dynamics simulations. I prepared plasmids, expressed, and purified all mutants and performed the steady-state analysis.

2.1. Introduction

G protein-coupled receptors (GPCRs) are essential for transferring extracellular signals into intracellular responses, and the duration of the signal is primarily regulated by the phosphorylation of intracellular loops and the C-terminal tails of activated GPCRs by GPCR kinases (GRKs) (22, 23). Although sequence analysis, crystallography, and comparison with other members of the broader structural superfamily of AGC kinases have provided insight into

¹This research was originally published in the *Journal of Biological Chemistry*. Yao, X.-Q., Cato, M. C., Labudde, E., Beyett, T. S., Tesmer, J. J. G., and Grant, B. J. Navigating the conformational landscape of G protein-coupled receptor kinases during allosteric activation. *J. Biol. Chem.* 2017; 292:16032-43. © the American Society for Biochemistry and Molecular Biology

the structure and function of GRKs, the mechanisms underlying GRK activation by GPCRs are not well understood (37, 63-67). A high resolution crystallographic structural model of an activated GPCR-GRK complex is not currently available, but biophysical, computational, and biochemical methods can be used to determine the conformational states that are sampled along the pathway to full GRK activation.

GRKs belong to the broader structural superfamily of AGC kinases (33). Kinases in the AGC superfamily share a common catalytic core comprising small and large lobes with the ATP-binding site at their interface (70). AGC kinases differ from the broader superfamily of eukaryotic protein kinases by featuring a conserved C-terminal tail involved in the regulation of kinase activation and localization (34). Within this C-terminal tail is the active site tether (AST), a loop that makes contact with ATP and is involved in nucleotide entry and exit from the kinase active site (71). In addition to their common catalytic subunit fold, over two-thirds of AGC kinases contain additional domains outside of the kinase domain that are also involved in kinase regulation and localization (32). By far the best structurally characterized AGC kinase is protein kinase A (PKA), with 190 entries in the Protein Data Bank (PDB). Structural determinants of the activation of AGC kinases, including GRKs, have thus been deduced primarily based on the spectrum of PKA crystal structures in various conformational states, with a $Mg^{2+} \cdot ADP \cdot AlF_3$ complex (PDB 1L3R) considered to be the most reflective of an active, transition state-like configuration (36). One hallmark of AGC kinase activation seen in this structural model is full closure of the small and large lobes of the kinase domain around a bound ATP molecule.

To fully understand the structural determinants involved in GRK activation, it is important to note that GRKs possess several unique features not found in other AGC kinases (**Figure 2.1**). GRKs have an N-terminal helix that is thought to interact specifically with their

GPCR substrates, C-terminal extensions that are important for membrane localization, and a regulator of G protein signaling homology domain (RHD), which, among other roles, maintains the small lobe of the kinase domain in a catalytically competent configuration that, in other AGC

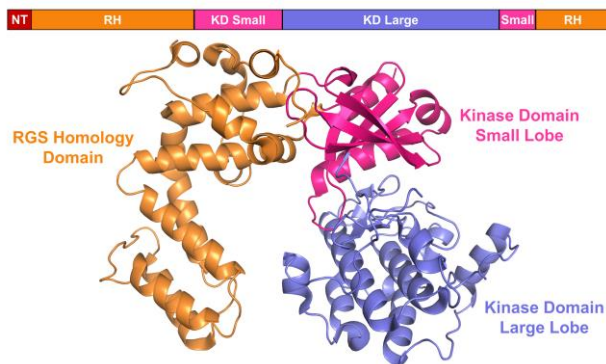


Figure 2.1. Domain architecture and structural arrangement of the GRK4 subfamily. PDB ID 4WNK (32)

kinases, would require the phosphorylation of two or more AGC kinase motifs that are not present in GRKs (25). In fact, the entire GRK kinase domain polypeptide sequence is inserted into a loop in the RHD, so these two domains are intimately linked within

the three-dimensional structure. Because the RHD bridges the small and large lobes of the kinase domain, another potential regulatory role for the RHD is to control the conformation of the kinase domain (41). We hypothesized that the RHD-KD interface is an intramolecular allosteric site that contributes to the ability of the kinase domain to adopt an active conformation.

To assess the importance of this proposed intramolecular allosteric site, mutations to disrupt the RHD-KD interface were made both *in silico* and *in vitro*, and subsequent changes in the frequency of KD closure and shifts in the steady-state parameters were determined.

2.2. Materials and Methods

2.2.1. Principal Component Analysis

PCA was performed to characterize inter-conformer relationships. Prior to PCA, iterated rounds of structural superposition were performed to identify the most structurally invariant region. During this procedure, residues with the largest positional variance were removed, before

each round of superposition, until only invariant core residues remained. The identified “core” residues were used as the reference frame for the superposition of crystal structures and MD trajectories prior to further analysis. For GRK structures, the “core” residues are mostly found in the large lobe of the kinase domain, including Lys244, Asp282-Gly312, Tyr323-Arg324, Asn330, Leu332-Asp335, Pro351, Gly353-Asp354, Val364-Gly379, Val413, Arg415-His426, Glu431-Lys433, Lys445-Leu448 (human GRK5 sequence). PCA was performed for the 11 crystallographic structures of the GRK4 subfamily, and then all GRK and PKA structures as well as MD trajectories were projected into the PC1-PC2 subspace for further analysis.

2.2.2. Contact Map Analysis

Residues were considered in contact if the minimal distance between any heavy atoms from each residue is less than 4.5 Å and the residues are separated by three amino acids in sequence.

2.2.3. Molecular Dynamics Simulations

MD simulations were performed with Amber12 using the ff99SB force field. The Mg²⁺-AMP-PNP-bound human GRK5 crystal structure (PDB: 4TND) (68) was employed as the starting model for all simulations. The AMP-PNP was replaced with an ATP by simply changing the nitrogen of the γ -imidophosphate to oxygen. Both N- and C-termini were capped with acetyl and methylamide groups, respectively. In addition, in simulations with AST removal, intra-chain termini of the broken chain were capped. In all systems, Arg and Lys were protonated while Asp and Glu were deprotonated. The protonation states for His residues were determined based on their pKa values at pH 7.0 calculated by PROPKA. Simulation structures were solvated in a truncated cubic box of pre-equilibrated TIP3P water molecules, which extended 12 Å in each dimension from the surface of the solute. Na⁺ or Cl⁻ counter-ions were added to neutralize the

systems. Energy minimization was performed in four stages, with each stage employing 500 steps of steepest decent followed by 1500 steps of conjugate gradient. First, minimization for solvent only was performed with fixed positions of protein and ligand atoms. Second, side-chain and ligand were relaxed with backbone still fixed. Third, all protein and ligand atoms were relaxed with fixed solvent. Fourth, all atoms were free to move without any restraint. Following minimization, a 10 ps MD was performed to heat the system from 0K to 300K under constant-volume periodic boundary conditions. A further 1 ns equilibration simulation was performed at constant temperature (300K) and constant pressure (1 bar). Subsequent 100-ns production-phase MD was then performed under the same conditions as equilibration. For both energy minimization and MD simulations, the particle-mesh Ewald summation method was adopted to treat long-range electrostatic interactions. In addition, an 8 Å cutoff was used to truncate the short-range nonbonded Van der Waals interactions. Additional operational parameters included a 2 fs time step, removal of the center-of-mass motion every 1000 steps and update of the nonbonded neighbor list every 25 steps. All hydrogen atoms were constrained using the SHAKE algorithm. In simulations with restraint, an additional linear-parabolic-flatted-well potential was applied to restrain the distance between specified atoms to around its initial value. The potential changes linearly when $R < r_1$ or $R \geq r_4$, where R is the atomic distance, $r_1 = 1.3 \text{ \AA}$, $r_4 = R_0 + 0.5 \text{ \AA}$, and R_0 is the target distance value. When $r_1 \leq R < r_2$ or $R_0 \leq R < r_4$, the potential is parabolic, where $r_2 = 1.8 \text{ \AA}$. The force constants for the left-hand and right-hand parabola are 20 and 80 ($\text{kcal} \cdot \text{mol}^{-1} \cdot \text{\AA}^{-2}$), respectively. The potential is zero when $r_2 \leq R < R_0$.

2.2.4. Plasmid Preparation

Human wild-type GRK5 with a non-cleavable C-terminal hexahistidine tag separated by a Val-Asp linker in a modified pMAL vector for expression in *Escherichia coli* was produced by

Emily Labudde. V92A, V92L, V92M, K454A, R455A, and K454A/R455A point mutations were all generated using inverse PCR. All plasmid samples were confirmed by Sanger sequencing through the University of Michigan DNA Sequencing Core.

2.2.5. Protein Expression and Purification

For expression in *E. coli*, BL21(DE3) suspension cultures containing the GRK5 expression plasmid of interest were grown at 37 °C to an optical density at 600 nm of ~0.6 before protein expression was induced by addition of 0.5 mM isopropyl β -D-1-thiogalactopyranoside (IPTG) at 20 °C. Cells were harvested at 16 h post-induction by centrifugation at 3000 relative centrifugal force (rcf) at 4 °C. Cell pellets were frozen at -80 °C and stored until future use.

For GRK5 purification, cell pellets were thawed and resuspended in Lysis Buffer (25 mM HEPES pH 7.5, 300 mM NaCl, 0.1 mM EDTA pH 8.0, 10 mM 2-mercaptoethanol (β -ME), 10 μ M leupeptin, 100 μ M phenylmethylsulfonyl fluoride (PMSF)) by 10-20 passes through a 40-mL Dounce homogenizer. Resuspended cells were lysed by three passes through a high-pressure homogenizer (Avestin Emulsi-Flex-C3). The soluble fraction was separated from the insoluble by ultracentrifugation at 40,000 rpm at 4 °C for 40 min. Clarified lysate was filtered through a 0.45 μ m PVDF filter (Millipore-Sigma) and passed over 3 mL of Ni-NTA-agarose resin (Qiagen) per 1-liter expression volume by gravity at 4 °C. Ni-NTA resin was washed with 10 column volumes of High-salt Wash Buffer (25 mM HEPES pH 7.5, 300 mM NaCl, 20 mM imidazole, 10 mM β -ME, 10 μ M leupeptin, 100 μ M PMSF) and 10 column volumes of Low-salt Wash Buffer (25 mM HEPES pH 7.5, 25 mM NaCl, 20 mM imidazole, 10 mM β -ME, 10 μ M leupeptin, 100 μ M PMSF) prior to elution with 5 column volumes of Elution Buffer (25 mM HEPES pH 7.5, 25 mM NaCl, 300 mM imidazole, 10 mM β -ME). The Ni-NTA elution fraction was concentrated to ~5 mL using a 30-kDa cutoff Amicon Ultra-15 centrifugal filter unit

(Millipore-Sigma) and diluted to 50 mL in Anion Exchange Buffer A (20 mM HEPES pH 7.5, 10 mM NaCl, 2 mM dithiothreitol (DTT)) to reduce the NaCl and imidazole concentrations prior to anion exchange chromatography using a 5-mL HiTrap Q HP column (GE Healthcare). Following a 10 column volume Anion Exchange Buffer A wash, GRK5 was eluted by a 20 column-volume linear gradient prepared from Anion Exchange Buffers A and B (20 mM HEPES pH 7.5, 500 mM NaCl, 2 mM DTT). Fractions with >90% pure GRK5 as assessed by Coomassie staining were pooled and concentrated to 3.5 mg/mL, flash frozen in liquid nitrogen, and stored at -80 °C until use in steady-state kinetic assays.

2.2.6. Radiometric Assays

Steady-state kinetic parameters (k_{cat} and K_m) for tubulin phosphorylation by GRK5 were determined at room temperature. 10- μ L kinase reactions containing 50 nM GRK5 and 500 nM soluble tubulin dimer (PurSolutions, bovine brain lyophilized tubulin) in Reaction Buffer (20 mM HEPES pH 7.5, 10 mM NaCl, 10 mM MgCl₂, 2 mM DTT) were initiated by addition of 1-75 μ M ATP supplemented with radioactive [γ -³²P]-ATP (PerkinElmer Life Sciences) and stopped in the linear initial velocity range of 20, 40, and 60 s by addition of 1X SDS gel loading buffer. Samples were separated on a 4-15% Criterion TGX precast gel (Bio-Rad), gels were exposed to a storage phosphor screen overnight and scanned using a Typhoon scanner, and bands corresponding to phosphorylated tubulin were quantified using ImageQuant software and converted to phosphorylated tubulin concentration ([p-tubulin]) (pM) based on a [γ -³²P]-ATP standard curve. [p-tubulin] was plotted as a function of time for each ATP concentration, and initial velocity values (pM p-tubulin·s⁻¹) were calculated as the slope of the line. These initial velocity values were then converted to kinase activity by dividing by the enzyme concentration (pM p-tubulin·s⁻¹· pM⁻¹ GRK), plotted as a function of ATP concentration, and fit to the

Michaelis-Menten equation to determine k_{cat} (s^{-1}) and K_{m} (μM) for each GRK5 variant. For steady-state parameter comparisons, the kinase activity of each mutant was normalized to the wild-type kinase activity value for each independent experiment. Each experiment was performed with $n = 3$. A one-way ANOVA was performed to determine which mutants have significantly different ($p < 0.05$) k_{cat} and K_{m} values relative to wild-type. All calculations, curve fitting, and statistical analyses were performed using GraphPad Prism 7.03.

2.3. Results

2.3.1. Principal Component Analysis

Between the 41 GRK crystal structures now deposited in the PDB with many different classes of inhibitors and substrates analogs bound, it remains ambiguous how close these structures are to being active and what the principal domain motions are. To methodically and quantitatively measure how active these GRK structures are in comparison to PKA, we determined the conformational profile of GRKs using principal component analysis (**Figure**

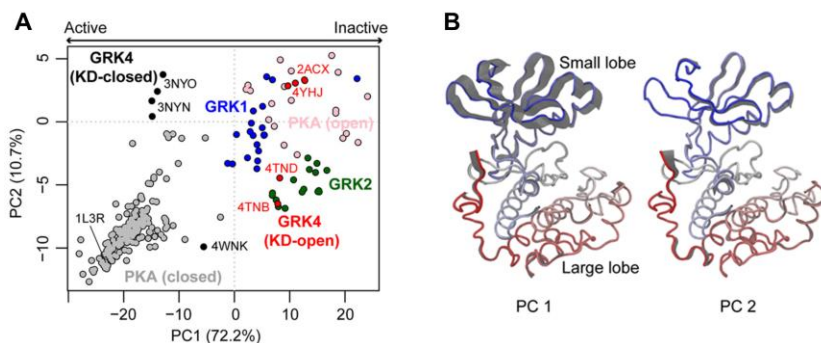


Figure 2.2. PCA reveals distinct crystallographic conformers and collective motions connecting conformers. A) KD-closed (black circles) and -open (red circles) GRK4, GRK1 (blue circles), and closed (gray circles) and open (pink circles) PKA crystal structures are projected into the PC subspace of a PCA performed on the crystal structures of GRK4 subfamily kinase domain. KD-closed structures represent a conformational state closer to the kinase active state, whereas KD-open structures represent the kinase inactive state. The numbers in axis labels indicate the percentage of total structural variance captured by the corresponding PC. **B)** The collective motions associated with PC1 and PC2. Only the kinase domain is shown and is color-coded by residue index (from blue N-terminus to red C-terminus). The gray shadow indicates the motion along the corresponding PC.

2.2A). The primary structural variation (principal component 1, or PC1; **Figure 2.2B)** found in the kinase domain (KD) of the GRK crystal structures analyzed was, not surprisingly, opening and closing of the small and large lobes of the

kinase domain around the ATP-binding site in an apparent clamshell-like motion. In addition, a smaller degree of domain motion among the GRK kinase domains was found to be attributed to twisting of the small lobe relative to the large lobe (principal component 2, or PC2; **Figure 2.2B**). Projecting all of the known PKA crystal structures onto the principal component (PC) subspace defined by the kinase domains of GRK structures revealed that the same structural variation associated with opening and closing of the kinase domain in GRKs also separates PKA crystal structures into open and closed, or inactive and active, conformations. Importantly, this PC subspace can be used as a straightforward way to assess the degree of activation of any GRK crystal structure based on the yardstick of activation of PKA.

Interestingly, GRK1- and GRK2-subfamily crystal structures tend to cluster on the kinase domain-open side of PKA in the PCA, while GRK4-subfamily structures cluster in the kinase domain-closed side, suggesting that GRK4-subfamily structures in general approach a more activated conformation. However, the majority of PKA structures, including the transition-state mimic structure, adopt a more closed conformation than is evident in any currently available GRK structure, which further supports the claim that no fully active GRK crystal structure has yet been determined. Furthermore, this suggests that the partially closed kinase domain observed in GRK4-subfamily crystal structures represents an

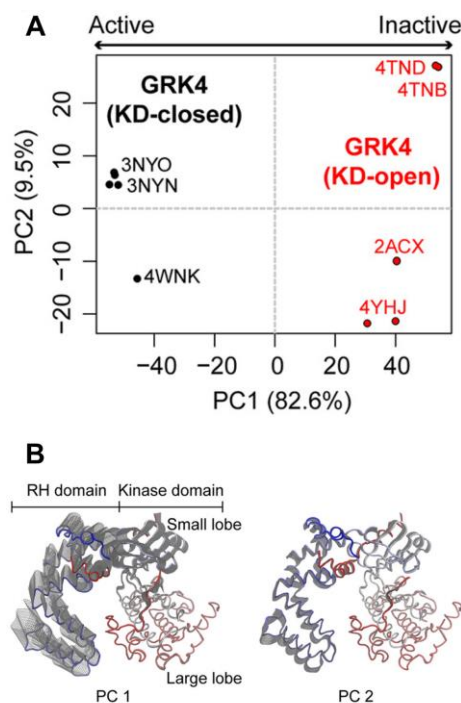


Figure 2.3. PCA of full-length GRKs. **A)** Projection of GRK4 subfamily structures into the PC subspace of a PCA performed on the crystal structures of full-length GRK4 subfamily members. **B)** The corresponding collective motions revealed by the full-length structure PCA.

intermediate conformational state that is sampled along the pathway to full kinase domain closure and GRK activation.

Repeating the principal component analysis discussed above on full-length GRK4-subfamily structures rather than only their kinase domains revealed that domain motion in the RHD is coupled to opening and closing of the kinase domain (**Figure 2.3**). More specifically, kinase domain (KD) closure is coupled to the RHD movement away from the KD large lobe, henceforth referred to as RHD opening. This coupling of the RHD and KD motions led us to hypothesize that the interface between the RHD and the large lobe of the KD that is disrupted upon RHD opening is an intramolecular allosteric site important for GRK activation.

2.3.2. Contact Map Analysis

When we assessed the number of intramolecular interactions between the RHD and KD large lobe in GRK4-subfamily crystal structures in either the most open or most closed KD crystal structures, we observed that more intramolecular contacts were made at the RHD-KD interface in the KD open structures. In particular, RHD/KD residue pairs of Glu91/Lys454, Val92/Lys454, Val92/Arg455, and Val92/Ala458 make intramolecular contacts in all six KD-open GRK4-subfamily structures that were assessed, and they lose contact in the five KD-closed structures that were assessed (**Figure 2.4A**). Closer inspection of KD-open crystal structures reveals a salt bridge between Glu91 and Lys454 and hydrogen bonds formed between the backbone carbonyl of Val92 and the side chain of Arg455 (**Figure 2.4B**). In addition, the side chain of Val92 makes contact with surrounding residues suggesting that the hydrophobic effect of burying this valine may be important for stabilization of the RHD-KD interface. To summarize, our analysis of residue-residue atomic contacts in either open or closed GRK4-subfamily structures highlighted four residue pairs that we hypothesized were important for

stabilizing the RHD-KD interface. We then sought to test this hypothesis by mutating Val92, Lys454, and Arg455 and observing the effects on RHD and KD opening and closure both *in silico* and *in vitro*.

2.3.3. Molecular Dynamics Simulations

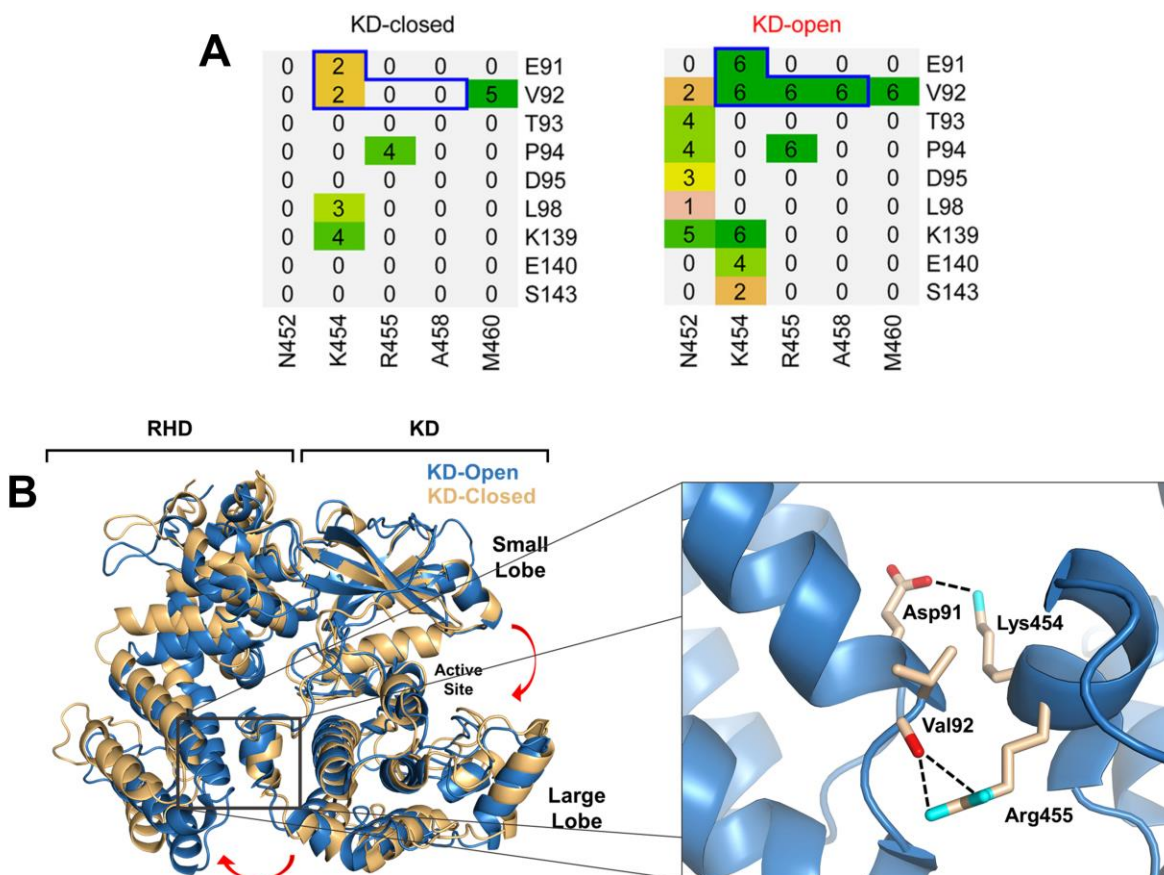


Figure 2.4. Residue contact and energy analyses focused on the RHD-large lobe interface identify potential residues involved in GRK activation. **A)** Residue contact analysis for KD-closed and KD-open structural groups. The value associated with each residue pair indicates the number of structures in the group in which the two residues are in contact. Regions outlined by blue lines contain residue pairs that form contact in all the KD-open structures but either lose the contact completely or form a contact much less frequently in the KD-closed structures. **B)** Superposed GRK4 subfamily KD-closed (gold) and KD-open (marine) structures. Hydrogen bonds between RHD and KD residues pairs are represented as dashed lines.

Based on our contact map analysis at the RHD-KD interface, we constructed six GRK5 mutants *in silico* to test the effect of interdomain perturbation by 1) disruption of the ionic interactions (K454A, R455A, and K454A/R455A) and 2) modulation of hydrophobic interactions (V29A, V92L, V92M). All molecular dynamics simulations started from a KD-open model (GRK5-AMP-PNP, PDB 4TND) with the first 14 residues in the N-terminus and the

AST-loop deleted because they are either disordered in most available GRK crystal structures or adopt a configuration that is an artifact of crystal packing. In addition, a distance restraint was placed between the truncated N-terminus and the RHD to prevent the N-terminus from adopting a biologically irrelevant conformation during the simulations.

Over the course of 100 ns of simulation time, the wild-type protein did not display any significant RHD opening (3% of total simulation time) or KD closure (0%), suggesting that the RHD-KD interactions are stable enough to maintain the protein in a RHD-closed and KD-open state. Disruption of the ionic interactions by single mutations (K454A and R455A) caused mild

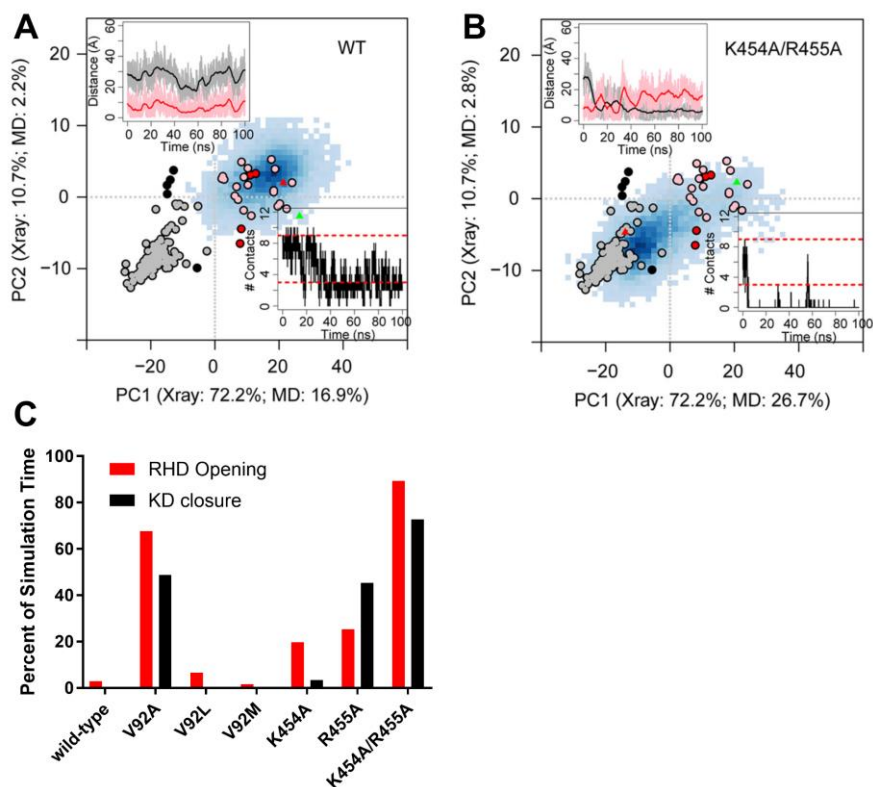


Figure 2.5. Select mutations disrupting domain interactions promote RHD opening and KD closure as revealed by MD simulations. A-B) Protein conformations are projected into the PC subspace of a PCA performed on the crystal structures of the GRK4 subfamily kinase domain. Blue shaded areas in each panel represent the conformations sampled by MD with darkness of color indicating sample density. The KD-closed (black circles) and -open (red circles) GRK crystal structures as well as the closed (red circles) and open (pink circles) PKA crystal structures are shown as references. The start (green triangles) and end (red triangles) of simulation are indicated in the map. The numbers in axis labels indicate the percentage of total variance of the GRK crystal structures and the simulation snapshots, respectively, captured by the corresponding PC. Top left inset, time series of the minimal distance between simulation snapshots and the KD-closed (black; dc) or KD-open (red; do) GRK structures. Bottom right inset, time series of the number of contacts between the RHD and the KD large lobe that are not observed in the KD-closed (RHD-open) crystal structures. C) Summary of the conformational sampling by the wild-type (WT) and mutant simulations.

enhancement of RHD opening (20% and 25%, respectively) and KD closure (5% and 45%, respectively), indicating that neither single mutation alone is sufficient to fully destabilize the ionic interactions at the RHD-KD interface. When the double mutant (K454A/R455A) was assessed, we observed a large enhancement in both RHD opening (90%) and KD closure (73%), suggesting an additive stabilization at the RHD-KD interface by these two ionic residues (**Figure 2.5**). Similarly, decreasing the hydrophobic stabilization between the RHD and KD with V92A caused a significant increase in both RHD opening (68%) and KD closure (49%). Interestingly, increasing the size of the hydrophobic side chain at Val92 (V92L and V92M) had no effect on

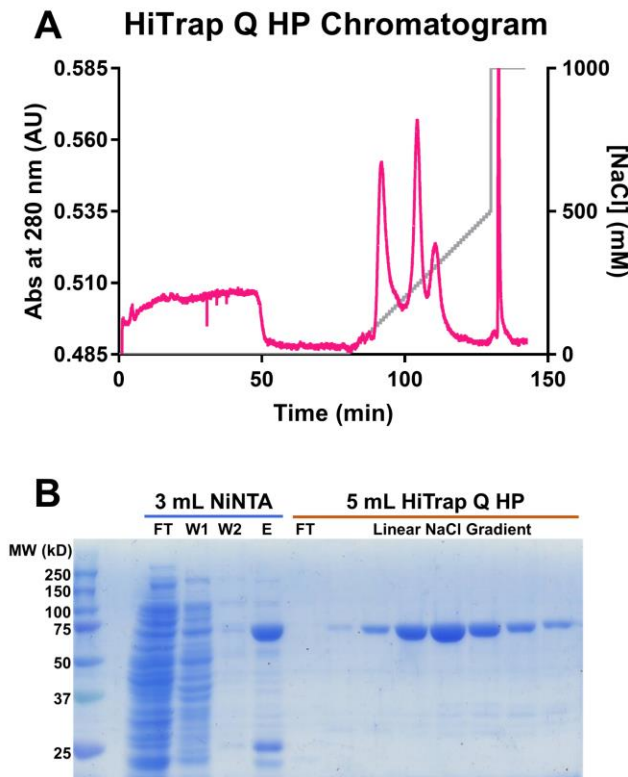


Figure 2.6. Representative purification of GRK5 from *E. coli*. **A)** Absorbance trace from anion exchange chromatography. The first peak contains active GRK5. **B)** SDS-PAGE analysis of a representative GRK5 purification. Fractions corresponding to different chromatography steps are indicated with blue (NiNTA) and orange (HiTrap Q HP) bars. FT, flow through; W1 and W2, wash 1 and 2; E, elution.

RHD opening (5% and 2%, respectively) or KD closure (0%) when compared to the wild-type simulations. In summary, our molecular dynamics simulations demonstrate that, when starting from an RHD-closed and KD-open model, wild-type GRK5 makes interactions at the RHD-KD interface that are stable enough to maintain the protein in a conformation where the RHD is locked to the large lobe of the KD. Neither the neutralization of K454A or R455A alone, nor increasing the hydrophobic bulk at amino acid position 92 (V92L and V92M), has a

large effect on RHD opening or KD closure. However, neutralizing both ionic residues (K454A/R455A) or decreasing the hydrophobicity of the side chain at amino acid position 92 (V92A) is sufficient to disrupt the stabilizing interactions at the RHD-KD interface enough to cause significant increases in the frequency of both RHD opening and KD closure. These results suggest that breaking the interaction between the RHD and KD large lobe is coupled to KD closure around the ATP-binding site and, we hypothesize, an increase in kinase activity.

2.3.4. Protein Expression and Purification

To validate our molecular dynamics results, we expressed wild-type and RHD-KD interface mutant GRK5 variants in *E. coli* and determined their steady-state parameters using an *in vitro* kinase assay. GRK5 was isolated by NiNTA affinity and anion exchange, and purity was assessed by SDS-PAGE (**Figure 2.6**). Protein yields of all GRK5 mutants were 1-2 mg/liter of expression volume.

2.3.5. Radiometric Assays to Determine Steady-state Parameters

To test the effect of disrupting the size and hydrophobicity of Val92, we generated V92A, V92L, and V92M mutants (**Figure 2.7, Table 2.1**). In agreement with the molecular dynamics simulations, increasing the size of the side chain with V92L and V92M had no effect on k_{cat} relative to wild-type, although there was a slight yet significant decrease by one-way ANOVA in the K_m for ATP of these mutants ($4.8 \mu\text{M}$, $p = 0.04$, and $4.4 \mu\text{M}$, $p = 0.05$, respectively) relative to wild-type ($6.7 \mu\text{M}$), resulting in 1.6- and 1.9-fold increases in catalytic efficiency (k_{cat}/K_m) relative to wild-type. This modest decrease in K_m may be reflective of a decreased propensity to release ATP from the active site once it is bound due to the potential steric clashes with the larger side chains at the RHD-KD interface in these mutants. V92A had the largest effect on k_{cat} out of any of the mutants tested with a 1.9-fold increase in k_{cat} relative to wild-type, consistent

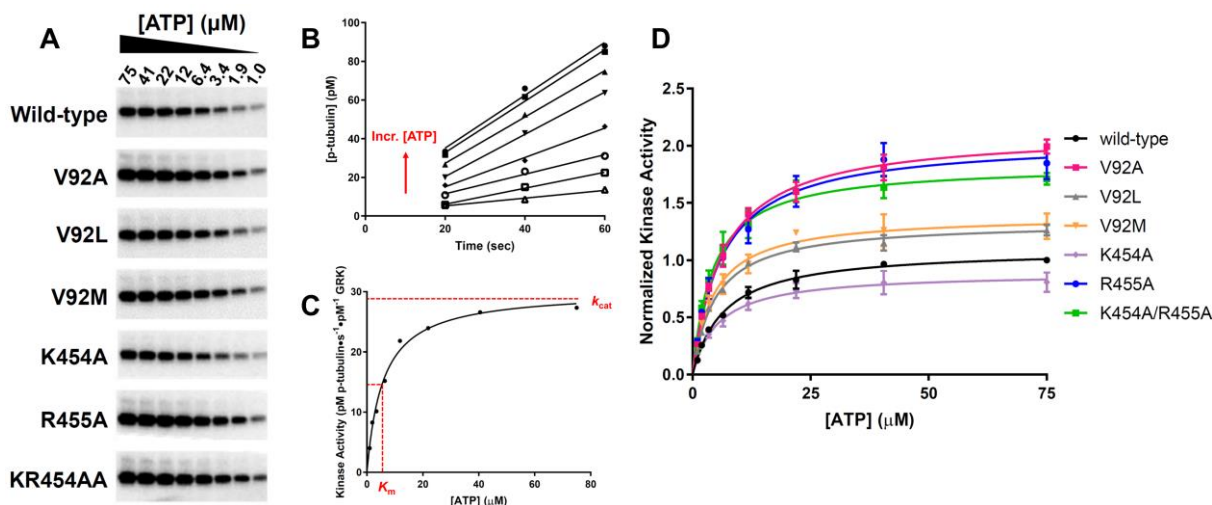


Figure 2.7. Disrupting the RHD-KD interface causes in vitro changes in steady-state parameters. Excess tubulin was incubated with 50 nM kinase, and the [ATP] was varied from 1 to 75 μM to determine kinase activity for wild-type GRK5 and RHD-KD interface mutants expressed in *E. coli*. **A)** Tubulin phosphorylation reactions at varying ATP concentrations were quenched at 20, 40, and 60 s, separated by SDS-PAGE, and exposed to a phosphor storage screen overnight. A representative gel of the 40 s time points is shown. **B)** After converting band intensities to pM p-tubulin using an ATP standard curve, [p-tubulin] was plotted as a function of time for each ATP concentration, and lines were fit to determine initial velocities (i.e. slopes in $\text{pM}\cdot\text{s}^{-1}$). Each line represents the three time points at a single ATP concentration, and the direction of the lines corresponding to increasing (Incr.) [ATP] is indicated with a red arrow. Only the wild-type data are shown for clarity. **C)** The slopes calculated from B were divided by the GRK concentration to calculate kinase activity ($\text{pM p-tubulin}\cdot\text{s}^{-1}\cdot\text{pM}^{-1}\text{ GRK}$), plotted as a function of [ATP], and fit to the Michaelis-Menten curve k_{cat} and K_{m} . Approximate k_{cat} and K_{m} values are indicated with red dotted lines. **D)** For each independent experiment, kinase activity of the RHD-KD mutants was normalized to wild-type and fit to the Michaelis-Menten curve to determine K_{m} values and k_{cat} values relative to wild-type. Each curve is the average of $n = 3$ experiments, and error bars represent standard error of the mean.

with the enhanced RHD opening and KD closure observed in the molecular dynamics

simulations. This result suggests that a smaller residue at this position does not make as many stabilizing hydrophobic interactions bridging the RHD and KD, thus shifting the equilibrium to an open RHD and favoring the closed KD state.

Next, we sought to test the effects of perturbing the ionic interactions and the RHD-KD interface by generating K454A, R455A, and K454A/R455A mutants (**Figure 2.7, Table 2.1**).

Table 2.1. Comparison of steady-state parameters

GRK5 variant	$K_{\text{m}} \pm \text{S.E.}$	k_{cat} (relative to WT)	$k_{\text{cat}}/K_{\text{m}}$ (relative to WT)
	μM		
Wild type	6.7 ± 0.6	1	1
V92A	6.4 ± 0.6	1.9	1.9
V92L	4.8 ± 0.4^a	1.2	1.6
V92M	4.4 ± 0.5^a	1.2	1.9
K454A	5.5 ± 0.9	0.8	0.9
R455A	6.1 ± 0.2	1.9	1.9
K454A/R455A	4.5 ± 0.6	1.7	2.5

^a $p < 0.05$ for K_{m} values by one-sample t test.

*Each value is calculated from $n = 3$ experiments. Indicated error is standard error of the mean.

Although Lys454 is positioned to form a salt bridge with Glu91 when the RHD and KD large lobe are engaged, we saw no significant changes in either the k_{cat} or K_{m} relative to wild-type in the single

K454A mutant. This result agrees with the K454A molecular dynamics simulations where the frequency of KD closure (3%) is close to that observed in the wild-type simulation (0%). With both R455A and the K454A/R455A double mutant, we observed a significant increase in k_{cat} (1.9- and 1.7-fold relative to wild-type, respectively) and a decrease in the K454A/R455A K_m (4.5 μM , as compared to 6.7 μM for wild-type). These mutants had 1.9- and 2.5-fold increases in catalytic efficiency, again in agreement with the large increase in the frequency of KD closure (45% and 73%) observed in our molecular dynamics simulations for these mutants. The increase in activity dependent on the R455A mutation may be reflective of a change in the ionic environment and/or a loss of stabilizing polar interactions between the Val92 backbone carbonyl and the guanidinium group of Arg455. Overall our *in vitro* results, in particular the increases in k_{cat} values for V92A, R455A, and K454A/R455A, mirror the molecular dynamics simulations, supporting our hypothesis that the equilibrium towards a more closed and active GRK conformation can be influenced by interactions at the RHD-KD interface.

2.4. Discussion

Using a combined approach of computational and *in vitro* experiments, we explored the structural dynamics and function of GRKs and propose an activation mechanism of the kinases that involves cooperative subdomain motions. Specifically, the small and large lobes of the KD close via an “asymmetric bite” (via the two major conformational changes captured by PC1 and PC2 from our principal component analysis) to achieve a configuration competent for catalyzing phosphotransfer. This closure of the KD small and large lobes is coupled with the opening of the RHD relative to the large lobe of the KD. Based on this model, potential allosteric residues, which are over 20 Å away from the active site, are predicted to be located at the RHD-KD interface. Our results show that perturbation introduced by site-directed mutagenesis of these

residues can indeed affect the dynamics of the kinase domain and the catalytic activity, thereby supporting our hypothesis that the RHD can allosterically impact kinase activation. In particular, mutants V92A, R455A, and K454A/R455A are shown to have increased frequency of KD closure *in silico* and enhanced catalytic efficiency for phosphorylation *in vitro*.

As many AGC kinases contain extra domains involved in cellular localization or regulation of kinase activity, a regulatory role for the RHD of GRKs has always been speculated, especially given that the GRK RHD has little or no GTPase-activating protein (GAP) activity despite high structural similarity to regulator of G protein signaling (RGS) proteins which are known to modulate GTPase activity in associated G proteins (39). Structural clues about the role of the RHD were first provided by the crystal structure of the GRK2–G β γ complex (PDB 1OMW) (41). In this structure, the GRK RHD was found to adopt the canonical α -helical bilobal fold (38) with the bundle subdomain adjacent to the small lobe of the kinase domain and the terminal subdomain adjacent to the kinase large lobe. In addition to the contacts made between the RHD terminal subdomain and the KD large lobe that were explored in this chapter, the α 10

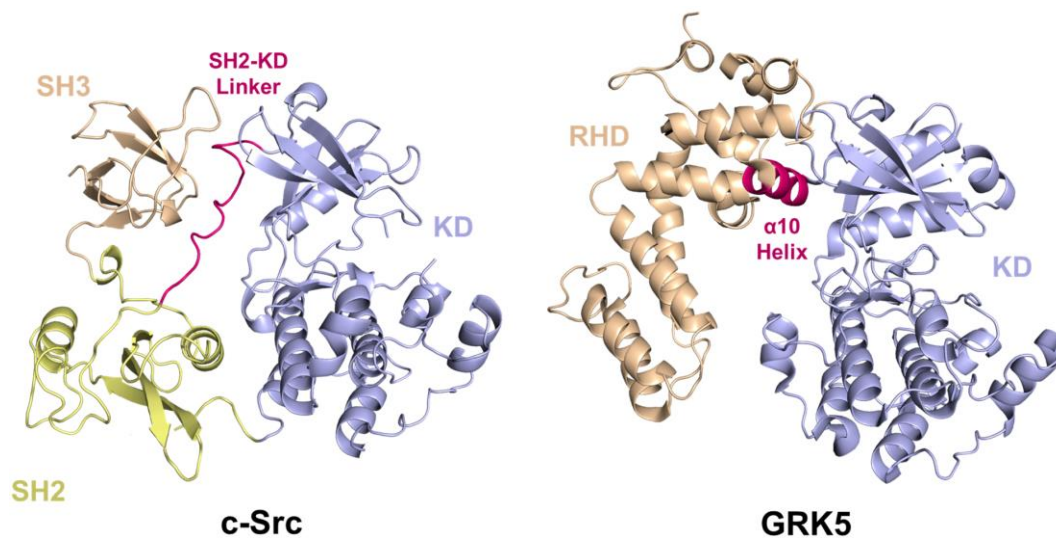


Figure 2.8. Comparison of c-Src and GRK5. SH3 (wheat) and SH2 (yellow) domains play a regulatory role in c-Src (PDB ID 1FMK) (72) and are suggested to play a similar role in GRK5 (PDB ID 4WNK) (32). An analogous role is also suggested for the SH2-KD linker in c-Src and the α 10-helix in GRK5 (magenta).

helix from the bundle subdomain of the RHD was identified as a potential site of regulation because it makes extensive contacts with two loops in the kinase small lobe that are adjacent to the active site (**Figure 2.8**). Thus, the $\alpha 10$ helix can be thought of as a bridge between the KD and RHD and could be involved either in the allosteric activation of GRKs or in the maintenance of an active small lobe conformation. When superimposed on the structure of c-Src, a distantly related protein kinase, it was found that the terminal and bundle subdomains of the RHD roughly overlay with the c-Src SH3 and SH2 domains, respectively, which are well-known to play a regulatory role in c-Src activation (72), suggesting an analogous role for the RHD in GRKs.

While our studies were being conducted, evidence for a regulatory role of the RHD was similarly provided by functional analysis of GRK5 activity towards the β_2 -adrenergic receptor (β_2 AR) (73). In this study, neutralizing the charged residues at the RHD-KD large lobe interface by making multiple alanine mutations caused a 60% increase in catalytic efficiency for β_2 AR phosphorylation by GRK5. In addition, molecular dynamics simulations showed more frequent and prolonged separation between the KD and RHD upon neutralizing charges at this interface, and covalently linking the RHD bundle domain to the KD large lobe with an engineered disulfide bond dramatically reduced GRK activity towards bleached rhodopsin, indicating, as expected, that a separation of the RHD and KD is required for formation of a catalytically competent kinase domain. Interestingly, the hinge for the domain motion from the authors' molecular dynamics simulations was near the $\alpha 10$ helix, in agreement with the hypothesis that perturbations in the RHD can be translated into the changes in kinase domain activity via the bridging $\alpha 10$ helix.

Our molecular dynamics and functional analyses of the RHD contact in GRK5 are largely consistent with this parallel study, but in either case, mutations at the interface only result in mild

activation of the kinase activity versus receptor or soluble substrates. Activated receptors, in contrast, have been reported to activate GRKs 100 – 1000-fold. Thus, this interface makes at best a mild contribution to the overall activation of GRK5 by GPCRs. Based on our prior crystallographic results, the majority of the activation likely involves modulation of the α N and AST-loop regions, stabilizing the active form of the kinase domain. In a previous hypothetical model, an activated GPCR is proposed to dock to the ~20 amino acid N-terminal α -helix (α N) of GRKs (74). This is similar to how receptors bind the C-terminal α 5 helix of the $G\alpha$ subunit of GDP-bound heterotrimeric G proteins (17), leading to G protein activation. Intriguingly, the α N region also contributes to the ordering of the AST-loop (37), a requisite for the kinase domain closure. The α N and AST-loop thereby form a bridge between the closed large and small lobes and create a surface through which activated receptors can regulate kinase activation allosterically. Integrating all of this information, we conclude that GRK activation is associated with a set of collaborative events, including N terminus ordering and binding to the receptor, AST-loop ordering, RHD opening, and KD closure.

It is unclear whether other GRK subfamilies are subject to the same allosteric control that we observed at the RHD-KD interface. Mutation of Arg458 in bovine GRK1 (analogous to Arg455 in human GRK5) to alanine has no effect on arrestin recruitment as measured by a Tango assay (75) and suggests that the level of allosteric control through the RHD-KD interface varies from GRK to GRK.

Our unique contribution to the story of GRK5 activation is that we empirically determined the coupling of kinase domain closure with separation of the RHD and KD by performing a bioinformatics analysis of all currently available GRK crystal structures and then supported our findings with *in silico* and *in vitro* experiments. In addition to neutralizing charged

residues at the RHD-KD interface (i.e. R455A and K454A/R455A, the so-called GRK “ionic lock” from Komolov et al. (73)), we also showed that the size of a hydrophobic residue (i.e. V92A) is equally if not more important for this interaction network. Moreover, by the nature of our experimental design, which used the soluble substrate tubulin to assess catalytic efficiency, we removed confounding effects of anionic detergents or lipids and showed that perturbing the RHD-KD interface with single or double amino acid mutations is sufficient to cause enhancement in GRK5 activity. Importantly, our analysis described the known conformational landscape for all reported GRK structures, allowing in the future a straightforward assessment of how active a new GRK structure may be as measured by the yardstick of PKA. We also showed that there are two dominant conformational transitions of the GRK kinase domain, a twist of the small lobe relative to the large lobe captured by PC2 and the clamshell-like motion captured by PC1, which together form an asymmetric bite motion. Regardless of the precise molecular mechanism of GPCR-mediated activation, we propose that it must lower energetic barriers for these transitions. Our results thus make a significant contribution to our understanding of GRK allosteric activation which, not inconsistent with other AGC kinases, likely involves structural perturbations of regions outside the kinase domain.

Chapter 3: Steady-State Analysis of a Region of GRK2 Predicted to be involved in Activated GPCR Engagement

Foreword

Ideas and conclusions presented in Chapter 3 are in preparation for publication. I collected all data presented herein and prepared all sections and figures.

3.1. Introduction

GPCR-mediated signal transduction pathways are essential for a variety of cellular events and are highly regulated, from the release of second messengers to termination of the response (4, 9, 18, 74, 76). Signal termination, which is achieved through GPCR desensitization and internalization into endosomes away from the cell surface, is particularly important for maintaining the cell in a state poised to respond appropriately to future incoming signals (22-23, 77). GPCR desensitization is initiated when specific residues on the receptor intracellular loop 3 (ICL3) or C-terminal tail are phosphorylated by serine/threonine kinases. These phosphorylation events can occur via second messenger-dependent kinases such as protein kinase A or C (PKA, PKC) in a process called heterologous desensitization which can occur regardless of the GPCR being activated (78-79). However, the primary method of regulated signal termination is by homologous desensitization, which is carried out by GRKs that specifically and rapidly

recognize actively signaling GPCRs and, unlike kinases involved in heterologous desensitization, are highly specific for agonist-bound, activated receptors over non-activated receptors (19, 24, 80-81). These processes are particularly important to understand because they are dysregulated in a number of devastating human diseases, including cancer and heart failure (21, 48, 50, 82).

Since GRKs were identified as regulators of GPCR-mediated signaling, an important question in the field of signal transduction has been how GRKs are activated in an agonist-dependent fashion (83-87). In other words, what structural features on GRKs are utilized to discriminate between the agonist-free and agonist-bound states of GPCRs, and how does binding to agonist-bound GPCRs enhance the catalytic activity of GRKs? It is well-established that activated GPCRs serve as allosteric activators of GRKs. In addition to increasing the phosphorylation of receptors, the presence of agonist-bound receptors increases the GRK catalytic efficiency towards soluble peptide substrates, showing that binding to activated GPCRs stabilizes a more catalytically competent conformation of the GRK kinase domain (67, 88). Despite a wealth of mechanistic information from high resolution crystal structures of five of the seven GRKs (41, 89-92), the structural determinants involved in the transition from the “open” (or inactive GRK state) to the “closed” (or active state) have been challenging to elucidate. In particular, the highly conserved GRK N-terminus and AST-loop regions, which have long been thought to play a role in the allosteric activation of GRKs, are disordered or in a conformation that is not expected to be biologically relevant in most crystal structures (37), which is likely reflective of the fact that most GRK structures do not adopt a fully closed kinase domain conformation.

In addition to regulation by allosteric activation, GRK activity is also dependent on membrane localization. The seven GRKs are divided into three subfamilies which differ

primarily in their C-terminal tails and mechanisms of membrane localization. The GRK1 subfamily members (GRK1 and 7) remain stably associated with the membrane through C-terminal prenylation modifications. GRK4 subfamily members (GRK4, 5, and 6) are either palmitoylated or contain positively charged patches that are associated with the negatively charged phospholipids in the membrane (93). GRK2 subfamily members (GRK2 and 3) are unique in that they have a C-terminal pleckstrin homology (PH) domain that allows association with the membrane in a $G\beta\gamma$ -dependent mechanism (93). In addition, GRK activity is influenced by binding to anionic phospholipids such as PIP2 and phosphatidylserine, although the question remains whether phospholipid binding causes an allosteric activation or is only supportive of membrane localization (25, 27-30, 94). Whether phospholipid binding has an allosteric effect or not, in the cell it is overshadowed by the 100- to 1000-fold allosteric activation driven by binding to active-state GPCRs.

Classically, in an effort to determine regions of GRKs that are important for their GPCR-mediated allosteric activation, structure-guided mutational analyses of GRKs have been carried out to determine residues that impair receptor phosphorylation but not soluble peptide phosphorylation. By this method, mutations that affect both receptor and soluble peptide phosphorylation are reflective of regions that stabilize the activated kinase conformation in general, whereas mutations that only impair receptor phosphorylation are likely to be at regions that make specific interactions with the receptor. The determination of the GRK6-sangivamycin crystal structure (37), which adopts the most closed kinase domain conformation of any other GRK structure seen to date and has a fully ordered N-terminus and AST-loop, was instrumental in guiding these mutational analyses. In this structure, the N-terminus was found to form an α -helix and lay across the kinase domain, where it makes interactions with both the small lobe and

the ordered AST-loop. Although differences in experimental design and results have led to some ambiguity in the details, decades of investigation by multiple research groups have led us to propose a model whereby GRKs make specific interactions with receptors through their highly conserved extreme N-terminal residues, and the remainder of the amphipathic N-terminal helix forms specific interactions with the kinase domain small lobe and the AST-loop, which becomes ordered upon kinase domain closure around a bound nucleotide. In addition, regions of the AST-loop have been shown to interact with residues in the large lobe of the kinase domain, which supports the hypothesis that ordering of these interactions would stabilize a closed conformation of the kinase domain (25, 63-66, 95). Thus, this GRK docking site comprised of the N-terminus, AST-loop, and possibly also surfaces on the kinase domain small lobe, are thought to form complementary interactions with activated receptors, which would stabilize the GRK in an activated conformation.

Recently, a β 2AR-GRK5 complex was isolated in PIP2-containing bicelles and was used to investigate interactions at the GRK-GPCR interface (73). In particular, crosslinking studies in combination with tandem mass spectrometry were used to identify regions on GRK5 that interact with ICL3 of the β 2AR in an agonist-dependent fashion (**Figure 3.1A**). In this study, regions that had previously been assigned as the N-terminal and C-terminal lipid binding domains in GRK5 were also found to form crosslinks with ICL3 of the β 2AR, suggesting that these lipid binding domains are also involved in making specific interactions with the activated receptor. When the structure of GRK2 is superimposed onto GRK5, we found that these lipid binding regions in GRK5 overlap with solvent-exposed hydrophobic patches in GRK2 (**Figure 3.1B**). Furthermore, we found that these hydrophobic patches, which occur on either the α NT-RH domain linker or a helix that connects the end of the RH domain to the PH domain, are uniquely conserved in the

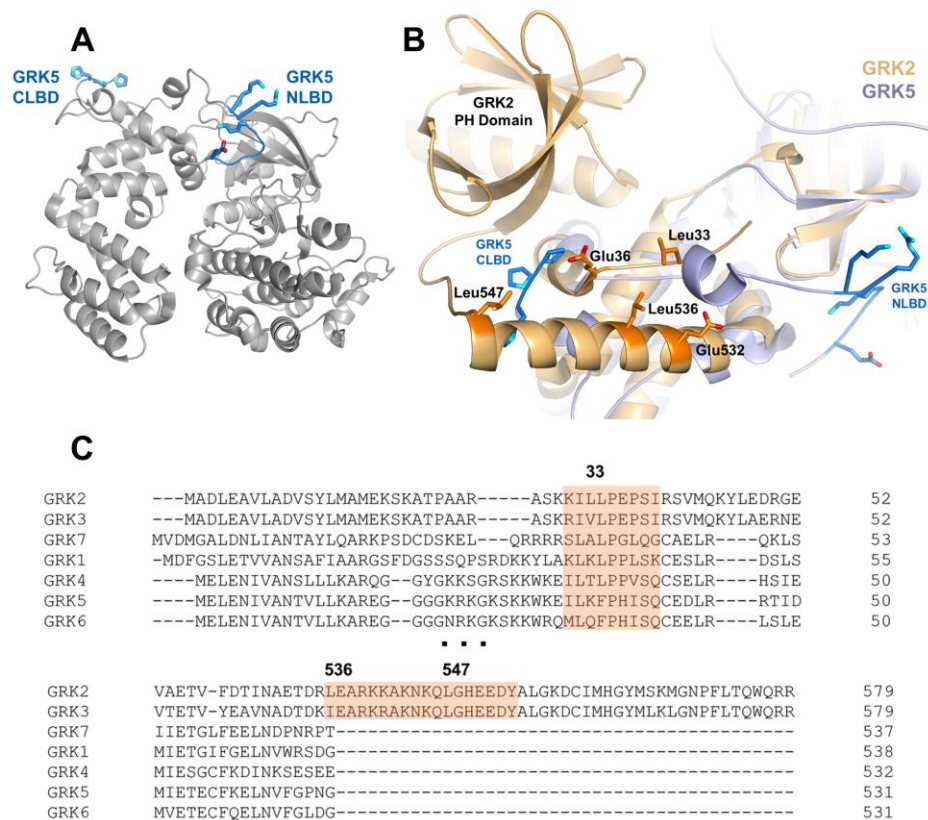


Figure 3.1. Comparison of GRK2 and GRK5 predicted GPCR engagement regions. **A**) Peptides (blue sticks) involved in crosslinks with the β_2 AR ICL3 are mapped onto a full-length GRK5 crystal structure (PDB ID 4TND, grey) (68). NLBD, N-terminal lipid binding domain; CLBD, C-terminal lipid binding domain. **B**) GRK2 (PDB ID 4PNK, gold) (104) alignment with GRK5 (slate) indicates the proximity of the ICL3-crosslinking peptides in GRK5 (blue sticks) with a hydrophobic patch of solvent-exposed residues in GRK2 (orange sticks). **C**) Multiple sequence alignment of the seven human GRKs, with the GRK2 subfamily-conserved solvent-exposed residue positions indicated.

GRK2 subfamily (**Figure 3.1C**). Closer inspection of this region revealed solvent exposed acidic residues on the same regions that are also uniquely conserved in the GRK2 subfamily. We thus hypothesized that these GRK2-subfamily conserved residues interact with complementary residues in ICL3 of activated GPCRs based on their proximity to ICL3-interacting regions observed in GRK5- β_2 AR crosslinking studies.

To test the hypothesis that GRK2 solvent-exposed conserved residues at the α NT-RH and RH-PH domain linkers make specific interactions with activated receptor substrates, we mutated, expressed, and purified L33N, E36A, E532A, L536N, and L547N from HEK293F cells and determined their steady-state kinetic parameters when either tubulin, a soluble substrate, or

rhodopsin in rod outer segments, a substrate in a more biologically relevant membrane environment, was used as a substrate. As a control, we also generated K220R, which has been shown to eliminate kinase activity in GRK2 (96). These studies would make a unique contribution to the field because they investigate whether a putative receptor binding surface identified in the GRK4 subfamily is making the analogous interactions in the GRK2 subfamily, and our conclusions would offer a possible explanation for how GRKs gain specificity for their GPCR substrates.

3.2. Materials and Methods

3.2.1. Plasmid Preparation

Bovine GRK2-S670A with a non-cleavable C-terminal hexahistidine tag in pcDNA3, a HEK cell expression vector, was a kind gift from Rachel Sterne-Marr at Siena College. For GRK2 studies, we routinely use the S670A variant because it eliminates an ERK1/ERK2 phosphorylation site that, when phosphorylated, decreases binding to $G\beta\gamma$ and GRK2 activity (81, 97). Site-directed mutagenesis was used to generate L33N, E36A, K220R, E532A, L536N, and L547N, and all constructs were verified by Sanger sequencing through the University of Michigan DNA Sequencing Core.

3.2.2. Protein Expression and Purification

For expression in HEK293F cells, 0.4 L of suspension HEK293F cells were transiently transfected with 500 μ g of the appropriate maxi-prepped plasmid at a polyethyleneimine-to-DNA ratio of 2:1 in Opti-MEM (Gibco). Cells were harvested by centrifugation at 3,000 rcf 60 h post-transfection, flash-frozen in liquid nitrogen, and stored at -80 °C until future use. Frozen cell pellets were thawed and lysed in 50 mL CelLytic M (MilliporeSigma) per 1 L of expression volume for 30 min at 4 °C. After dilution to 60 mL in NiNTA Equilibration Buffer (25 mM

HEPES pH 8.0, 500 mM NaCl, 10 mM β -ME, 10 μ M leupeptin, 100 μ M PMSF), the soluble fraction was isolated by ultracentrifugation at 40,000 rpm at 4 °C for 45 min. Clarified lysate was filtered through a 0.45 μ m PVDF filter.

Filtered clarified lysates were passed over 0.5 mL NiNTA resin equilibrated in Equilibration Buffer by gravity. Resin was washed with 10 column volumes of High Salt Wash Buffer (25 mM HEPES pH 8.0, 500 mM NaCl, 40 mM imidazole, 10 mM β -ME, 10 μ M leupeptin, 100 μ M PMSF) and 10 column volumes of Low Salt Wash Buffer (25 mM HEPES pH 8.0, 50 mM NaCl, 40 mM imidazole, 10 mM β -ME, 10 μ M leupeptin, 100 μ M PMSF) prior to elution in 10 column volumes of Elution Buffer (25 mM HEPES pH 8.0, 50 mM NaCl, 150 mM imidazole, 10 mM β -ME). Eluted protein was diluted to 50 mL in Ion Exchange Buffer A (20 mM HEPES pH 8.0, 25 mM NaCl, 2 mM DTT) and loaded onto a tandem 1 mL HiTrap Q HP (GE Healthcare)/1 mL HiTrap SP HP (GE Healthcare) column set-up. The tandem column set-up was then disassembled, and GRK2 was eluted from the 1 mL HiTrap SP HP by a linear NaCl gradient prepared from Ion Exchange Buffers A and B (20 mM HEPES pH 8.0, 1 M NaCl, 2 mM DTT). Protein fractions that were >90% pure as assessed by SDS-PAGE and Coomassie staining were pooled, concentrated, and buffer exchanged into Storage Buffer (20 mM HEPES pH 8.0, 100 mM NaCl, 10% glycerol, 2 mM DTT), flash-frozen in liquid nitrogen, and stored at -80 °C until use in steady-state assays.

3.2.3. Protein Concentration Normalization

Prior to use in assays, protein concentrations of the frozen purified protein samples were normalized to wild-type as follows. Total protein concentration for each variant after a single freeze-thaw was determined by Bradford analysis, equal amounts of total protein were separated on a 10% polyacrylamide gel by SDS-PAGE, and the gel was stained using Bio-Safe Coomassie

Stain (Bio-Rad). The gel was scanned, and band intensities corresponding to GRK2 only were analyzed in ImageQuant. To bring all GRK2 concentrations to the same level prior to use in assays, the wild-type GRK2 concentration determined by Bradford analysis was assumed to be correct, and concentrations of the other variants were adjusted based on their relative GRK2 band intensities.

3.2.4. Radiometric Assays to Determine Steady-State Parameters

Steady-state parameters for the phosphorylation of tubulin and rhodopsin in rod outer segments (ROS) by GRK2 with variable ATP concentrations were determined at room temperature as described in Chapter 2 with the following exceptions: 1) Reaction Buffer contained lower salt (20 mM HEPES pH 7.5, 2 mM NaCl, 2 mM MgCl₂, 2 mM DTT) and 2) reactions were stopped at 8 min, which was determined to be in the linear range of the GRK2 kinase reaction for both tubulin and rhodopsin (data not shown). In addition, steady-state parameters for the phosphorylation of rhodopsin in ROS were determined with variable rhodopsin concentrations. For variable rhodopsin experiments, reactions containing 20 nM GRK2 and 150 nM human G β γ ₂ in low salt Reaction Buffer were incubated with 50 nM-5 μ M light-activated rhodopsin in ROS and initiated by the addition of 5 μ M ATP supplemented with radioactive [γ -³²P]-ATP. Hyperphosphorylated rhodopsin in urea-stripped ROS and wild-type human G β γ ₂ was provided by Qiuyan Chen. As with other radiometric assays, reactions were quenched at 8 min with SDS gel loading buffer, and phosphorylated products were separated on a 4-15% Criterion TGX precast gel. Gels were exposed to a phosphor screen overnight, scanned using a Typhoon scanner, and band intensities corresponding to phosphorylated product were quantified using ImageQuant software. For each independent experiment, band intensities were normalized to wild-type such that the highest wild-type band intensity was set to 1 to account for

day-to-day variability in phosphor screen intensity. Each experiment was performed with $n = 3$. K_m and normalized V_{max} were determined by plotting normalized band intensity as a function of either [ATP] or [rhodopsin] and fitting to the Michaelis-Menten equation. Statistical significance was assessed by one-way ANOVA using multiple comparisons corrections. All curve-fitting and statistical analyses were performed using GraphPad Prism 7.03.

3.3 Results

3.3.1. Purification of GRK2 Mutants Expressed in HEK293F Cells

GRK2 variants were expressed and purified from HEK293F cells rather than insect cells, as they have been for high yield crystallographic studies, to facilitate a more efficient approach

to protein production. As expected, the His₆-tagged GRK2 construct bound well to NiNTA and was eluted at 150 mM imidazole. A tandem Q/S column (tandem anion/cation exchange) was selected for an additional purification step because a single S (cation exchange) column was ineffective at separating impurities from GRK2. At pH 8, many anionic impurities in the NiNTA elution were first trapped on the Q (anion exchange) column, while the GRK2 flowed through the

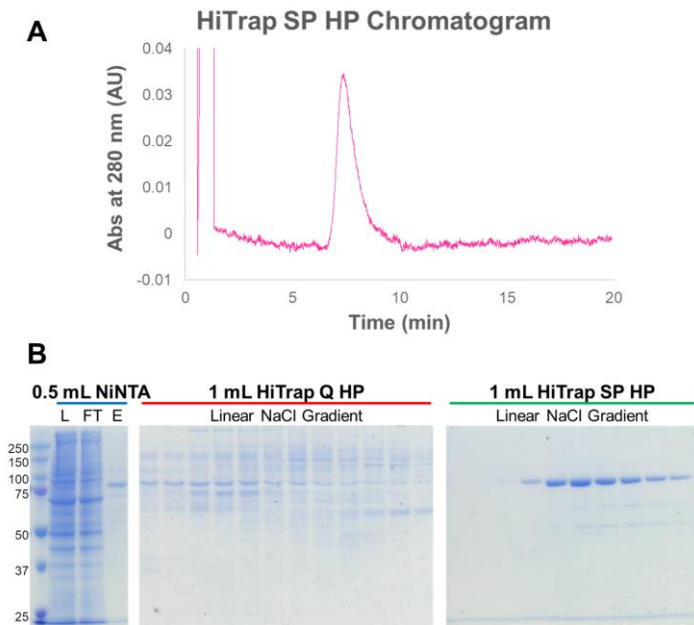


Figure 3.2. Representative purification of bovine GRK2 from HEK293F cells. **A)** Absorbance trace from cation exchange chromatography indicates that GRK2 elutes as a single peak. **B)** SDS-PAGE analysis of 0.5 mL NiNTA affinity (blue bar), and tandem anion (orange bar) – cation (green bar) chromatography steps. For 1 mL HiTrap Q and SP HP columns, the NiNTA elution was loaded on a tandem column setup, and then individual 1 mL columns were separated and linear NaCl gradients were run over each independently. The Q column trapped many impurities, allowing >90% pure GRK2 to be eluted from the SP column. L, load; FT, flow through; E, elution.

Q column and bound to the S column. GRK2 was then cleanly eluted from the S column in a single peak, and a single predominant band corresponding to GRK2 was observed in SDS-PAGE (Figure 3.2). Typical GRK2 protein yields from HEK293F cells were 50-100 $\mu\text{g}/1$ L expression volume.

3.3.2. GRK2 Concentration Normalization

The GRK2 mutant concentrations were normalized to the wild-type GRK2 concentration prior to use in kinetic assays to account for variability in protein sample purity. SDS-PAGE

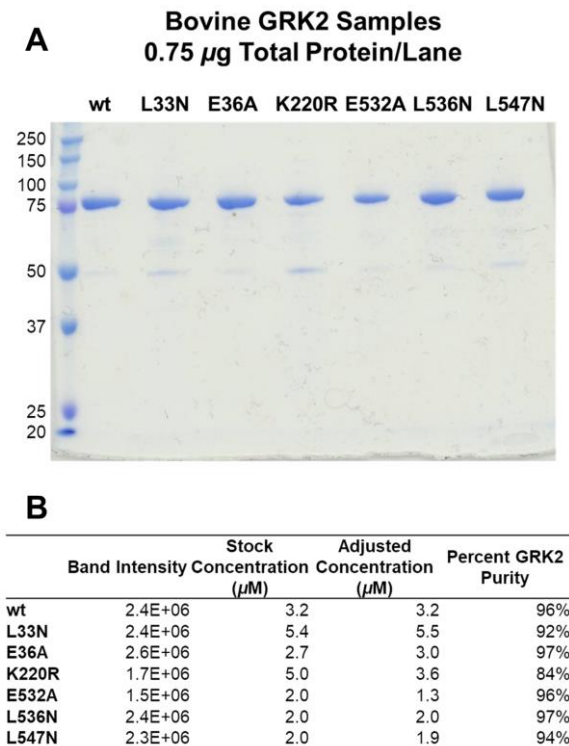


Figure 3.3. GRK2 concentration normalization. **A)** Purified GRK2 samples used in kinase assays. 0.75 μg total protein is loaded in each lane. **B)** Quantification of band intensity and percent GRK2 purity of the gel samples in Fig. 3.3A. Stock concentrations were adjusted based on the relative GRK2 band intensities, and these adjusted concentrations were used when calculating volumes for reaction preparations.

analysis indicated that the total protein concentrations as determined by Bradford analysis were not exactly reflective of GRK2 concentration alone because certain samples had more impurities than others (Figure 3.3A). Given the direct relationship of V_{max} to enzyme concentration, it is essential to ensure that the concentration of the protein of interest is consistent when performing Michaelis-Menten analyses. We determined the percent GRK2 purity for each of the variants using band densitometry analysis, and then brought the GRK2 in each sample to the same relative

level. This GRK2 concentration adjustment caused some samples to have higher impurities than

others (**Figure 3.3B**). With the exception of K220R, which was 84% pure, all of the samples are >90% pure, so we do not expect these impurities to affect our assay readout.

3.3.3. GRK2 Michaelis-Menten Analysis

To assess the effect of mutating solvent-exposed residues conserved within the GRK2 subfamily that overlay with ICL3-interacting residues in GRK5, we first performed a Michaelis-Menten analysis on both the soluble substrate, tubulin, and rhodopsin in ROS when the concentration of ATP was varied from 1-75 μM (**Figure 3.4**). We hypothesized that there would be no change in K_m values or normalized V_{max} for tubulin phosphorylation because we did not

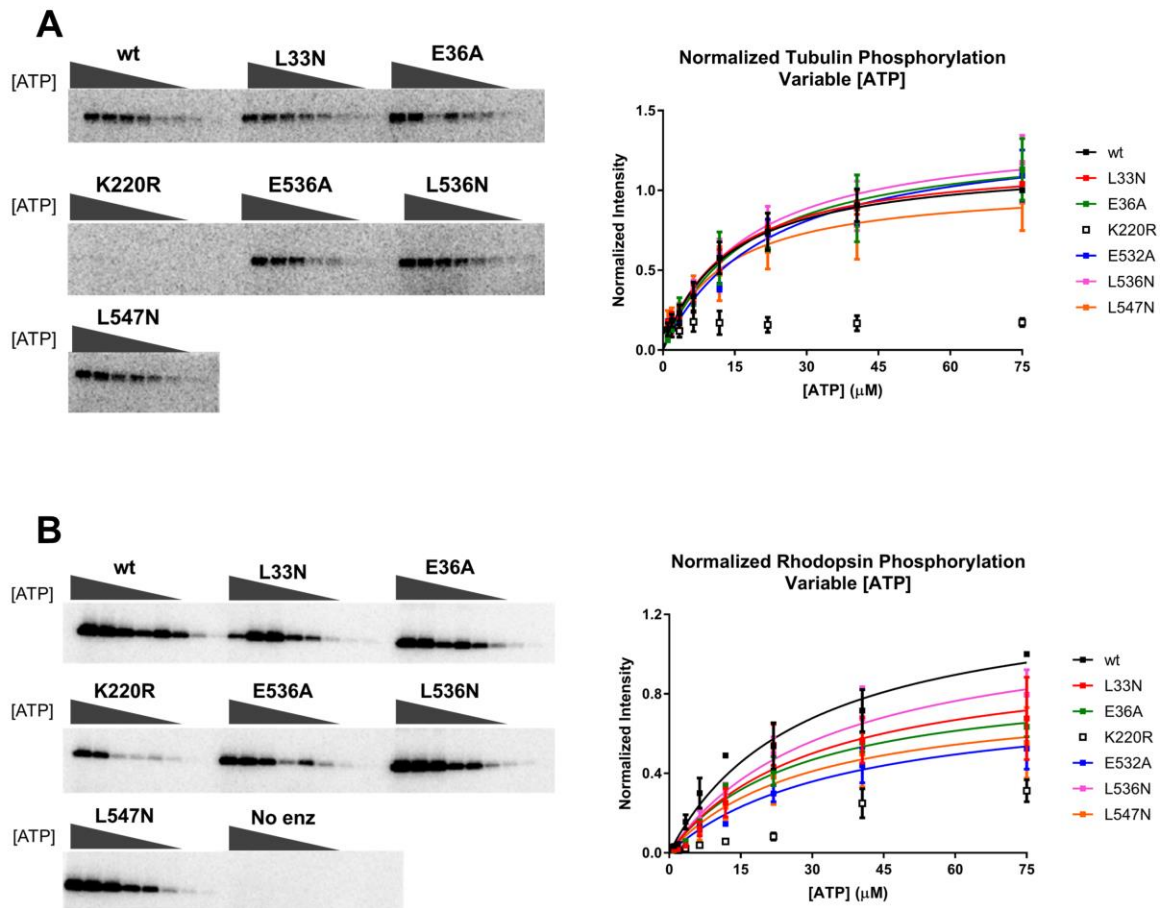


Figure 3.4. Michaelis-Menten analysis with variable [ATP]. A) Tubulin phosphorylation and B) rhodopsin in ROS phosphorylation by the GRK2 mutants was detected by SDS-PAGE. Bands correspond to phosphorylated product at variable ATP concentrations. Band intensities are plotted as a function of [ATP] and fit to the Michaelis-Menten model. Plots are representative of $n = 3$ experiments, and error bars represent the standard deviation.

expect these mutations to affect the binding kinetics of ATP or the ability of the kinase domain to adopt a closed state in the absence of receptor. Similarly, we did not expect any changes in K_m for rhodopsin phosphorylation when ATP was varied, but changes in the normalized V_{max} for rhodopsin could be indicative of a receptor binding defect. In line with our hypothesis, we observed no significant changes in K_m , normalized V_{max} , or normalized V_{max}/K_m (henceforth referred to as “normalized catalytic efficiency”) for either tubulin or rhodopsin phosphorylation when the concentration of ATP was varied.

We also performed Michaelis-Menten analysis on rhodopsin in ROS when the concentration of rhodopsin was varied rather than ATP (**Figure 3.5**), with the hypothesis that receptor binding effects in the variants would be captured as changes in the K_m for rhodopsin given that the K_m is mathematically related to the K_d . The results we observed did not support our hypothesis, as there was no significant difference in the K_m for rhodopsin in any of the variants. We did observe slight but consistent and statistically significant decreases in normalized V_{max} for all of the variants except L33N, which could either reflect a change in the forward rate constant for catalysis, the enzyme concentration, or specific activity differences among the variants purified. Because the variants have no more than a 2-fold decrease in

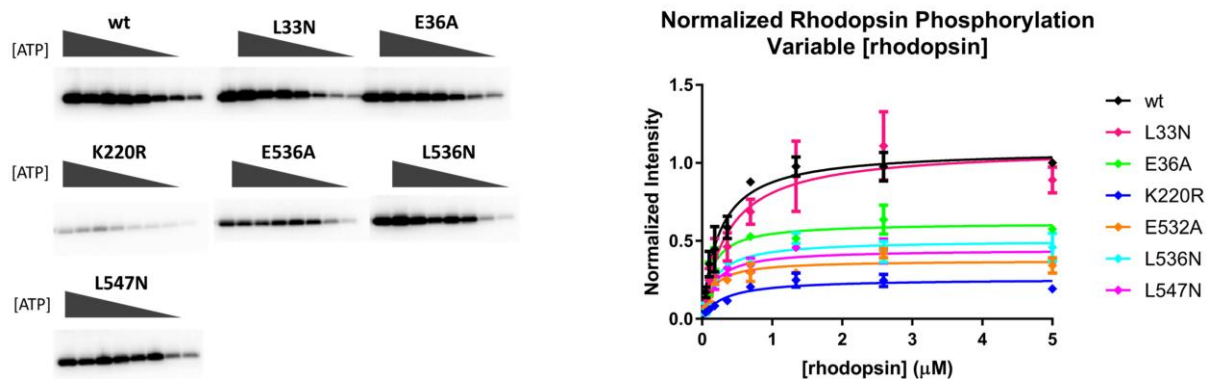


Figure 3.5. Michaelis-Menten analysis with variable [rhodopsin]. The phosphorylation of rhodopsin in ROS by GRK2 mutants was assessed by SDS-PAGE, and band intensities corresponding to phosphorylated product from $n = 3$ experiments were plotted as a function of [rhodopsin]. Error bars represent the standard deviation.

normalized V_{\max} , and none of these changes are seen in the normalized catalytic efficiency, we conclude that these minor but significant normalized V_{\max} changes are a reflection of variability in specific activity and cannot on their own be indicative of receptor binding defects.

3.4. Discussion

In this study, we performed Michaelis-Menten analyses using GRK2 variants with predicted receptor-binding defects on tubulin and rhodopsin when the concentration ATP was varied, and on rhodopsin when the concentration rhodopsin was varied. We hypothesized that we would not observe changes in tubulin phosphorylation but would see rhodopsin phosphorylation defects, which would suggest impaired receptor engagement as a result of single mutations in GRK2. Specifically, we predicted that an increase in the K_m for rhodopsin in the GRK2 mutants would be indicative of a receptor binding defect. We observed no significant changes in the steady-state parameters for tubulin or rhodopsin with either variable [ATP] or [rhodopsin], with the exception that we consistently saw a decrease in normalized V_{\max} in our variable [rhodopsin] experiments that we attribute to differences in specific activity of the GRK2 variants.

We chose to replace leucine with asparagine, which is a relatively conservative mutation in that these two side chains are the same size and charge, with the primary difference being a change from nonpolar to polar, to specifically probe the importance of having hydrophobic side chains at this region. Hydrophobic side chains are rarely found on the surface of proteins, but rather are either folded into the protein core or buried in a protein-protein interaction. The fact that these hydrophobic patches, which are modeled as facing the solvent in all of our GRK2 crystal structures, are conserved in the GRK2 subfamily strongly suggests that they play a role in some protein-protein interaction. Alternatively, it is possible that these hydrophobic chains insert

into the acyl phase of the membrane, though a significant conformational change would need to occur to bring this hydrophobic patch close enough to the membrane to interact with lipids.

Although we saw no significant defects in the normalized catalytic efficiency of tubulin or rhodopsin with the mutations we selected, the possibility remains that more disruptive mutations could cause a receptor binding defect. In addition, the single mutations we made may not have enough of a detectable change in the context of our steady-state experiment, but the use of double- or triple-mutants may have a more drastic effect. Another interpretation of the data presented here is that GRK2 may interact with ICL3 of β 2AR through this region, as suggested for GRK5, but the much shorter ICL3 found in rhodopsin cannot make the analogous interactions. If so, the way this patch of solvent-exposed residues on GRKs interacts with ICL3 segments from different receptors may serve as a way for GRKs to discriminate between GPCR binding partners. To fully assess the potential role of these solvent-exposed hydrophobic residues in GRK2 receptor engagement, a number of different receptors with variable ICL3 lengths and compositions will need to be tested.

In summary, we performed an *in vitro* steady-state analysis on GRK2-mediated phosphorylation of tubulin and rhodopsin when either the [ATP] or [rhodopsin] substrates were varied. We found no significant effects when solvent-exposed hydrophobic amino acids were mutated to polar residues or solvent-exposed charged residues were mutated to neutral, suggesting that this region is not an essential determinant for rhodopsin engagement. The question remains if and how this GRK2 subfamily-conserved patch interacts with the ICL3 of different receptors not explored in this study.

Chapter 4: Structural and Functional Characterization of GRK2-Selective Small Molecule Inhibitors²

4.1. Introduction

Many cellular events are regulated by signaling pathways instigated by G protein-coupled receptors (GPCRs) (4). GPCR kinases (GRKs) specifically recognize and phosphorylate activated GPCRs, leading to their desensitization and internalization, which is critical for a normal return to cellular homeostasis (21). The seven mammalian GRKs are divided into the GRK1 (GRKs 1 and 7), GRK2 (GRKs 2 and 3), and GRK4 (GRKs 4, 5, and 6) subfamilies based on sequence homology (19). The GRK1 subfamily is expressed primarily in the retina and GRK4 in the testes, whereas GRKs 2, 3, 5, and 6 are more ubiquitously expressed (22).

Cardiovascular function is controlled in part by β -adrenergic receptors (β ARs). In the normally functioning heart, β ARs at the cardiomyocyte cell surface are activated in response to increased circulating levels of the fight-or-flight hormones, epinephrine and norepinephrine, leading to an increase in cardiac output (48). GRK2 and GRK5, the predominant GRKs expressed in the heart, then regulate signal termination through β AR phosphorylation leading to subsequent internalization of the β ARs (45). In the failing heart, epinephrine and norepinephrine levels remain high in an attempt to compensate for decreased cardiac output (52). Although

²Research presented in this chapter was reproduced in part with permission from Waldschmidt HV, et al. Structure-Based Design, Synthesis and Biological Evaluation of Highly Selective and Potent G Protein-Coupled Receptor Kinase 2 Inhibitors. J. Med. Chem. 2016; 59(8):3793-807; Waldschmidt HV, et al. Structure-Based Design of Highly Selective and Potent G Protein-Coupled Receptor Kinase 2 Inhibitors Based on Paroxetine. J. Med. Chem. 2017; 60:3052-69; and Bouley R, et al. Structural Determinants Influencing the Potency and Selectivity of Indazole-Paroxetine Hybrid G Protein-Coupled Receptor Kinase 2 Inhibitors. Mol. Pharmacol. 2017; 92:707-17.

initially beneficial for increasing heart contractility, prolonged exposure to catecholamines exacerbates the problem as evidenced by increased GRK2 and GRK5 levels, a decreased number of β ARs at the cell surface, and initiation of a pathological hypertrophic stress response (43). β AR antagonists (β -blockers) are currently used to treat heart failure, but an increasing number of studies suggest that inhibition of GRK2, GRK5, or both could improve the currently available heart failure therapies (49, 54-58, 62, 98).

Although both GRK2 and GRK5 can phosphorylate β ARs, there is growing evidence that GRK2 and GRK5 have distinct pathological roles within the failing heart (47, 50, 51, 60, 99). Increased GRK2 levels are primarily responsible for the decrease in cell-surface β ARs and the prolonged sympathetic nervous system activation, leading to decreased contractility (99). GRK5 is unique among GRKs in that it has a Ca^{2+} -calmodulin-dependent nuclear localization signal (NLS) that allows GRK5 to translocate into the nucleus where it phosphorylates histone deacetylase 5 (HDAC5), turning on the transcription of hypertrophic genes (60). Indeed, cardiac-specific GRK2 knockout mice have improved contractility and increased cell-surface β ARs post-myocardial infarction (55), and GRK5 knockout mice are protected from cardiac hypertrophy following controlled cardiac stress (61). The extent of the functional differences in GRK2 and GRK5 within cardiomyocytes remains to be elucidated, but selective inhibition of each of these kinases would offer the opportunity to further understand each of their roles in the progression of heart failure. In addition, the selective inhibition of GRK2 or GRK5 presents the possibility of treating different aspects of heart failure without compromising the entire cardiac regulatory system.

In the following two chapters, I discuss our progress towards the development, structural and pharmacological characterization, and improvement of GRK2- and GRK5-selective

inhibitors that we envision will be useful as selective probes for the distinct activities of these two closely related kinases. In addition, our top compounds will serve as starting models for the development of inhibitors that have exciting therapeutic potential for treating heart failure. Finally, the structural characterization of GRK-inhibitor complexes has offered a wealth of information about GRK structure, function, and the conformational changes that are associated with opening and closure of the kinase domain that are discussed in more detail in Chapter 2. Chapter 4A and 4B address our progress towards developing highly potent and selective GRK2 inhibitors based on the GSK180736A (4A) and paroxetine (4B) scaffolds, and Chapter 5 discusses the development of GRK5 inhibitors that gain their specificity through covalent interaction with the AST-loop.

4.2. Structure-Based Design, Synthesis, and Biological Evaluation of Highly Selective and Potent GRK2 Inhibitors Based on GSK180736A

4.2.1. Foreword

Ideas and conclusions presented in Chapter 4A are published in the *Journal of Medicinal Chemistry* (100), including selected sections and figures which are copied verbatim. The publication was originally written primarily by Dr. Helen Waldschmidt and me, along with our mentors Dr. John Tesmer and Dr. Scott Larson. Dr. Helen Waldschmidt synthesized all compounds and performed pharmacological assays with GRK1, 2, and 5. Dr. Kristoff Homan purified PKA, GRK2, and $G\beta\gamma$, and collected diffraction data for the GRK2- $G\beta\gamma$ -CCG224062 complex. Dr. Osvaldo Cruz optimized the ROCK1 inhibition assay procedure. I performed the ROCK1 and PKA inhibition assays presented in this study. Along with Jessica Waninger, a rotation student at the time, I purified, crystallized, and collected data for GRK2- $G\beta\gamma$ co-crystal

structures with CCG215022, CCG224406, and CCG224411. In collaboration with Dr. John Tesmer, I refined models for co-crystal structures with CCG224062, CCG215022, CCG224406, and CCG224411, and I performed all structural analysis presented below. Drs. Alessandro Cannavo, Jianliang Song, Joseph Cheung, and Walter Koch isolated adult cardiomyocytes from mice and performed contractility assays.

4.2.2. Background

GRKs are members of the larger superfamily of AGC kinases, which are related by a structurally similar kinase domain fold (33). A significant challenge in developing GRK-specific inhibitors is that the ATP-binding site is highly structurally conserved among all 60 AGC kinase members, so ATP-competitive inhibitors tend to have poor selectivity and a high potential for off-target effects. Despite high structural similarity in the active site, there is precedent for successful kinase inhibitor specificity. GSK180736A (**Figure 4.1**) was originally developed as an inhibitor of the AGC kinase, Rho-associated, coiled-coil containing protein kinase 1

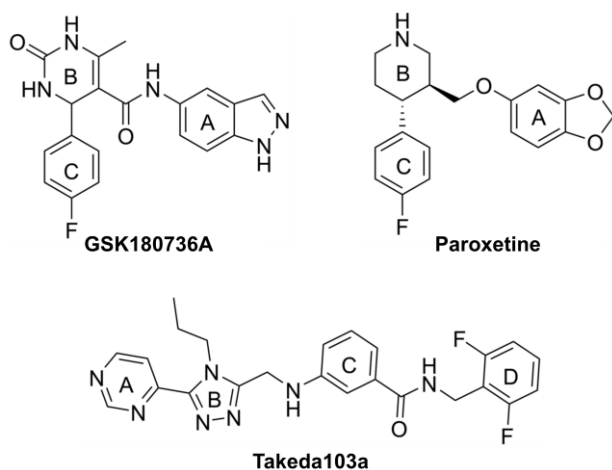


Figure 4.1. GRK2-selective inhibitors. Precedent for GRK2-selective inhibition is demonstrated by these three lead compounds. A, B, C, and D ring systems align in the adenine, ribose, polyphosphate, and hydrophobic subsites of the GRK kinase domain, respectively. The A ring interacts with the hinge, whereas the D ring interacts in a pocket defined by the P-loop, α B, and α C helices in the kinase domain small lobe, and by the DFG-loop in the large lobe.

(ROCK1), with an IC_{50} of 100 nM (101).

When screened against representative members of the three GRK subfamilies in the Tesmer lab, it was also found to have modest potency and high selectivity for GRK2 over the other GRKs, with a GRK2 IC_{50} of 770 nM and GRK1 and GRK5 IC_{50} s $>100 \mu M$ (102).

Poor bioavailability of GSK180736A and high potency for ROCK1 has limited

its therapeutic potential as a GRK2 inhibitor. In addition, Takeda103A (**Figure 4.1**) was developed as a GRK2-selective compound and thus demonstrates even higher GRK2 potency, with an IC_{50} of 20 nM, while maintaining GRK2 selectivity among the other GRKs (70-fold selectivity) and ROCK1 (500-fold selectivity) (103). Takeda103A has very poor bioavailability, so despite its high potency and selectivity for GRK2, it is not a good candidate to pursue for clinical trials. In a screen performed by the Tesmer lab, the selective serotonin reuptake inhibitor

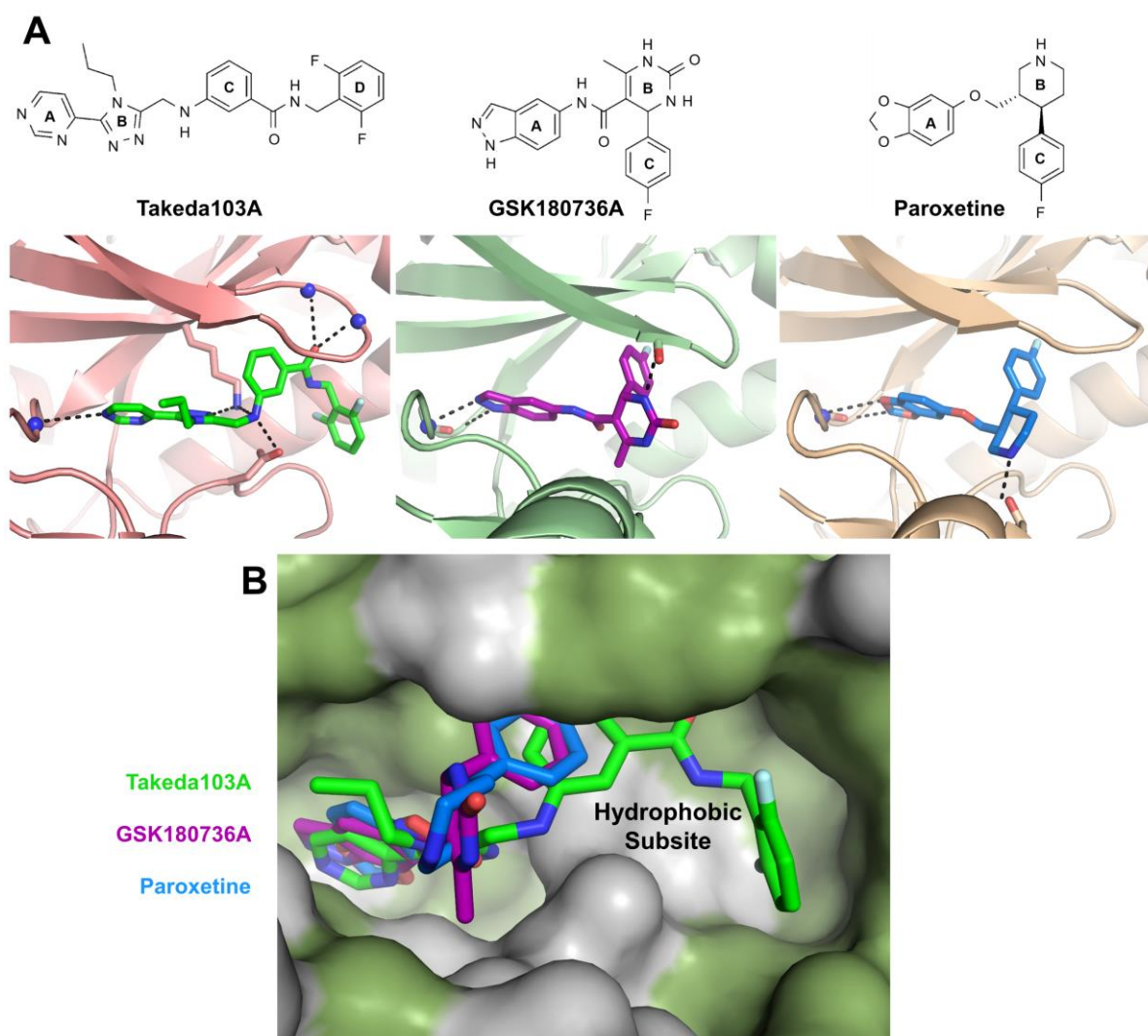


Figure 4.2. Structural models of GRK2-G $\beta\gamma$ in complex with the three lead compounds. A) Takeda103A (3PVW) (103), GSK180736A (4PNK) (104), and paroxetine (3V5W) (58) all bind in the ATP-binding site where they make interactions with the kinase domain hinge and pack under the P-loop. B) Structural alignment of the three co-crystal structures shows their strikingly similar binding poses within the GRK2 binding site. Notably, only Takeda103A extends into the hydrophobic subsite.

(SSRI), paroxetine (**Figure 4.1**), was also identified as a modest GRK2 inhibitor with 1.4 μM potency and 10- to 100-fold selectivity over other GRKs, ROCK1, and PKA (58). As an FDA-approved drug with good pharmacokinetic properties (59), paroxetine was identified as a promising lead, although GRK2 potency needed to be increased and selectivity maintained in order to make it a more attractive drug candidate.

Previous Tesmer lab members were successful in determining high resolution GRK2 co-crystal structures with GSK180736A (4PNK) (104), Takeda103A (3PVW) (103), and paroxetine (3V5W) (58) (**Figure 4.2**). Importantly, these crystal structures demonstrated that the three inhibitors bind with similar poses in the ATP-binding pocket of GRK2, making stabilizing hydrogen bond interactions with protein backbone atoms in the kinase domain hinge and packing under the P-loop. Although these compounds are chemically unrelated, GSK180736A, Takeda103A, and paroxetine make analogous interactions with GRK2 in the adenine subsite, ribose subsite, and polyphosphate subsite (105). Only Takeda103A, which has the highest GRK2 potency, extends into the hydrophobic subsite of the GRK2 active site pocket, and we believe that the improved GRK2 potency of Takeda103A is in part conferred by the additional buried surface area and stabilizing hydrogen bonds made in this region (103).

We hypothesized that we could develop highly potent and selective GRK2 inhibitors by combining the desirable properties of GSK180736A and Takeda103A. A series of moieties of differing bulk and chemical properties that were meant to mimic characteristics of the Takeda103A arm reaching into the GRK2 hydrophobic subsite were appended onto the GSK180736A parent molecule, and we assessed their structure-activity relationships (SAR) using X-ray crystallography and pharmacological assays. Finally, we explored the biological effects of our top inhibitors in an *ex vivo* mouse cardiomyocyte contractility assay.

4.2.3. Materials and Methods

4.2.3.1. Library Construction

Starting from the GSK180736A parent molecule, a library of derivative compounds was synthesized by Helen Waldschmidt by appending a variety of amide-linked moieties with differing bulk, linker length, flexibility, and chemical properties.

4.2.3.2. Pharmacological Assays

IC₅₀s for GRK1, 2, and 5 were determined using a radiometric assay performed by Helen Waldschmidt. IC₅₀s for PKA and percent inhibition calculations for ROCK1 were performed using the ADP-Glo Kinase Assays system (Promega) in accordance with the manufacturer's recommendations with the following modifications. For determination of PKA IC₅₀s, reactions containing 438 μ M of the catalytic subunit of PKA, 58 μ M CREBtide substrate, and 100 pM–10 μ M inhibitor were initiated by the addition of 100 μ M ATP. For ROCK1 single dose response at 10 μ M, reactions containing 60 nM ROCK1 (Promega), 60 μ M S6K substrate, and 10 μ M inhibitor were initiated by the addition of 60 μ M ATP. For both PKA and ROCK1, reactions were stopped at 30 min by addition of ADP-Glo reagent and allowed to incubate for 40 min. Kinase Detection reaction was added and allowed to incubate for 30 min, and luminescence was measured using a BMG Labtech PHERAstar imaging system. PKA dose response curves were fit to the four-parameter (variable slope) log(inhibitor) vs. response model using GraphPad Prism. Percent ROCK1 inhibition at 10 μ M was calculated by normalizing single dose response values for each inhibitor to no inhibitor (negative control, 0% inhibition) and GSK180736A (positive control, 100% inhibition) controls.

4.2.3.3. Plasmid Preparation and Insect Cell Expression of Bovine GRK2 and Human G β γ

Bovine GRK2-S670A with a non-cleavable C-terminal His₆ tag was cloned into the polyhedrin promoter of the pFastBac Dual expression vector (ThermoFisher) using restriction cloning by engineered N-terminal BamHI and C-terminal XbaI restriction sites. A soluble variant of the human G β γ 2 containing an N-terminally His₆-tagged β 1 subunit and carrying a C68S mutation on the γ 2 subunit in the pVL1392 dual promoter expression vector was a gift from Dr. Brian Kobilka. P0 virus preparation for expression in insect cells was carried out by following Bac-to-Bac Baculovirus Expression System (ThermoFisher) instructions for GRK2 or BaculoGold Baculovirus Expression System (BD Biosciences) instructions of G β γ 2-C68S. Virus titer and volume was amplified to the P2 stage by infecting *Spodoptera frugiperda* cells at low titer and harvesting the amplified lysate after clear signs of cell infection but before total cell lysis (4-5 days post-infection). BTI-Tn-5B1-4 (High Five) insect cells at 1 million cells/mL were infected with P2 virus, and cells overexpressing GRK2 or G β γ 2-C68S were harvested 48 h post-infection.

4.2.3.4. Protein Purification

GRK2 was purified from the clarified lysate using NiNTA affinity and cation exchange (Source 15S) chromatography and subsequently gel filtered into 20 mM HEPES pH 7.5, 100 mM NaCl, and 1 mM DTT using a Superdex 200 10/300 column (GE Healthcare). G β γ 2-C68S was purified from clarified lysate using NiNTA affinity and anion exchange chromatography (HiPrep Q XL 16/10, GE Healthcare). Fractions containing G β γ 2-C68S were pooled and gel filtered into 20 mM HEPES pH 8.0, 100 mM NaCl, and 1 mM DTT using a tandem Superdex 200 10/300 -- Superdex 75 10/300 (GE Healthcare) column assembly. For both GRK2 and G β γ 2-C68S, highest purity gel filtration samples as assessed by Bio-Safe Coomassie stained SDS-PAGE gels

were pooled and concentrated to 10-12 mg/mL, as determined by Bradford analysis, flash frozen in liquid nitrogen, and stored at -80 °C.

4.2.3.5. Crystallization and Data Processing

For crystallization trials, GRK2 and G β ₁ γ ₂-C68S were mixed in a 1.2:1 molar ratio of GRK2: G β γ with a final total protein concentration of 9–11 mg/mL. A final concentration of 500 μ M inhibitor was added from a 25 mM stock in 100% DMSO. A final concentration of 2 mM MgCl₂ was then added from a 120 mM stock. The complex was stored on ice for 30 min prior to filtration through a 0.2 μ m Nanosep centrifugal device. All inhibitor complexes were crystallized at 4 °C by vapor diffusion using hanging drops consisting of 0.8 μ L GRK2-G β γ -inhibitor complex and 0.8 μ L reservoir solution which contained 50 mM MES pH 6.0, 0.8–1.2 M NaCl, and 8–16% PEG 3350. Crystals appeared after 3 days and continued to grow for 1–2 weeks. Crystals were harvested in a cryoprotectant solution containing the contents of the reservoir solution supplemented with 25% ethylene glycol and 500 μ M inhibitor and were flash frozen in liquid nitrogen. Diffraction data were collected at the Advanced Photon Source on the LS-CAT beamline 21-ID-G at a wavelength of 0.97857 Å. Crystallization trials, crystal harvesting, and data collection were completed with the assistance of Jessica Waninger. Data reduction was performed using HKL2000 (106). Phases for each of the structures were initially estimated using molecular replacement in the Phaser module of CCP4 (107) using the GRK2-GSK180736A structure (PDB ID 4PNK) (104) as the search model. Refinement was conducted by alternating between manual real-space refinement and reciprocal space refinement using both the Refmac5 module of CCP4 (108) and the phenix.refine program of the PHENIX suite (109). Model building was performed using Coot (110). The final models were validated with MolProbity

(111) prior to deposition into the Protein Data Bank under accession codes 5HE0 (CCG215022), 5HE1 (CCG224062), 5HE2 (CCG224406), and 5HE3 (CCG224411).

4.2.3.6. Mouse Cardiomyocyte Shortening Assays

Myocyte shortening assays were performed in collaboration with Dr. Walter Koch's laboratory as described previously (77).

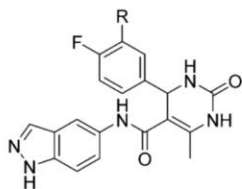
4.2.4. Results

4.2.4.1. Structure-Activity Relationships of the GSK180736A Derivative Compounds

In this study, we investigated the effects of varying the appendage designed to occupy the GRK2 hydrophobic subsite on inhibitor potency towards a representative member of each GRK subfamily (GRK1, 2, and 5), as well as a representative member of the AGC kinase superfamily (PKA), and ROCK1, because the GSK180736A scaffold was originally designed as a potent ROCK1 inhibitor (0.1 μM) (**Table 4.1**). Because Takeda103A, a potent GRK2 inhibitor, has an aromatic ring occupying the hydrophobic subsite, we first assessed the effects of appending a benzene into the position henceforth referred to as the D-ring. The addition of a benzene in the D ring position (**12b**) was essentially equipotent to the GSK180736A parent compound for both GRK2 (0.69 μM) and ROCK1 (0.069 μM), but this substitution did eliminate the already low inhibitory activity towards PKA, suggesting that increased bulk can be used to build out selectivity for PKA. Indeed, we lost all potency for PKA when anything larger than a carboxylic acid was appended to this position on the scaffold.

Restricting the conformational flexibility of the D ring was tested by inserting a 2-methoxy substituent onto the benzyl ring (**12e**). This substitution improved GRK2 potency about 10-fold (0.06 μM) from the unsubstituted benzene (**12b**), although the ROCK1 potency was unaffected (0.057 μM) and GRK1 (16 μM) and GRK5 (2.3 μM) potency was enhanced.

Table 4.1. Inhibitory activity of the GSK180736A derivative compounds



Compound	R	GRK2 IC ₅₀ (μM)	GRK1 IC ₅₀ (μM)	GRK5 IC ₅₀ (μM)	PKA IC ₅₀ (μM)	ROCK IC ₅₀ (μM)
Paroxetine	-	1.38±1.00	>100	>100	>100	10%*
Takeda103A	-	0.02±0.001	9.0±3.2	2.2±0.92	ND	10%*
GSK180736A	H	0.77±0.5	>100	>100	30±19	0.10±0.09
10	COOH	20±10	>100	>100	78.1±72	0.19±0.14
12a	CONHMe	4.3±0.7	>100	>100	>100	0.56±0.68
12b	CONHBn	0.69±0.3	71±2	4.7±1.9	>100	0.069±0.044
12c		0.20±0.1	11.9±2.3	0.80±0.0.1	>100	0.021±0.13
12d		0.22±0.2	>100	5.0±1.2	>100	0.11±0.084
12e		0.060±0.03	16±6.4	2.3±2.7	>100	0.057±0.044
12f		0.42±0.05	>100	3.8±0.9	>100	0.097±0.076
12g		0.46±0.3	>100	8.1±4.7	>100	0.050±0.011
CCG215022		0.15±0.07	3.9±1.0	0.38±0.06	>100	0.011±0.013
12i		0.28±0.1	>100	6.2±3.8	>100	0.023±0.022
12j		4.8±1.9	>100	40.0±14	>100	0.084±0.009
CCG224062		0.28 ±0.06	0.10±0.05	1.8±0.54	ND	0.012±0.004
12l		0.13±0.03	>100	>100	>100	6.7±8.2
12m		0.07±0.01	>100	63±32	>100	5.8±5.5
CCG224406		0.13±0.03	>100	>100	>100	0%*
12o		1.2±0.7	>100	>100	>100	22%*
12p		2.7±2.3	>100	>100	>100	1.9±0.25
12q		1.9±1.3	>100	68±26	>100	0.15±0.05
CCG224411		0.23±0.05	>100	58±13	>100	0.29±0.033
13a		25±12	>100	88±60	>100	0.45±.28
13b		>100	>100	>100	>100	0.40±0.32
13c		0.45±0.29	>100	>100	>100	0.20±0.05

All IC₅₀ values are an average of *n* = 3 experiments. Errors shown represent standard error of the mean.

*Percent inhibition at 10 μM ROCK1. ND, not determined.

Movement of the methoxy group around the benzyl ring (**12f-g**) indicated that the 2-benzyl (**12e**), or *ortho* position, was the most favorable for GRK2 potency.

With that in mind, we then further

assessed the *ortho* position with a 2-

pyridyl analog (CCG215022) and found

that this D ring moiety is well-tolerated

in all of the GRKs and ROCK1, making

it a pan-inhibitor. Increasing the bulk by

substituting the pyridine of CCG215022

with an isoquinoline to make

CCG224062 resulted in a higher potency

pan-GRK and ROCK1 inhibitor,

suggesting that increasing the van der

Waals contacts at the hydrophobic

subsite is favorable for potency, at least

within the GRK family.

To further understand the effects

of increasing bulk and decreasing

conformational flexibility at the D ring

position, we added a second methoxy

substituent to the 2-methoxybenzyl

analog (**12e**) to create the 2,6-dimethoxybenzyl derivative (CCG224406). This compound was our top compound for GRK2-selectivity, as it completely eliminated potency for GRK1, GRK5, PKA, and ROCK1. Comparing the single methoxy-substituted compound (**12e**, GRK2 IC₅₀ = 60 nM, ROCK1 IC₅₀ = 57 nM) to the dimethoxy-substituted compound (CCG224406, GRK2 IC₅₀ = 130 nM, ROCK1 IC₅₀ > 10 μM) suggests that increasing the bulk and decreasing the conformational flexibility at the D ring position is a method of mitigating ROCK1 inhibition while retaining excellent GRK2 potency.

Finally, we investigated the effects of elongating the linker by inserting a methylene either between the amide and the C ring (**13a-c**) or between the amide and the D ring (**12i-j** and CCG224411). In all compounds tested, GRK2 potency decreased and sub-μM ROCK1 activity returned when the linker was elongated. For example, when we directly compared 2,6-dimethylbenzyl derivatives with either a short methyl (**12m**) or longer ethyl (CCG224411) linker between the amide and the D ring, we found that GRK2 potency is decreased 3-fold (70 nM in **12m**, 230 nM in CCG224411) and the ROCK1 potency is increased 20-fold (5.8 μM in **12m**, 290 nM in CCG224411).

4.2.4.2. GRK2-Gbg co-crystallization with CCG215022, CCG224062, CCG224406, and CCG224411

Bovine GRK2-S670A (**Figure 4.3A**) and human Gβ₁γ₂-C68S (**Figure 4.3B**) were expressed in High Five insect cells, purified to homogeneity, and co-crystallized with three of the GSK180736A-derived inhibitors (CCG215022, CCG224406, and CCG224411). An additional X-ray data set of bovine GRK2–human Gβ₁γ₂-C68S co-crystallized with CCG224062 was provided by Kristoff Homan.

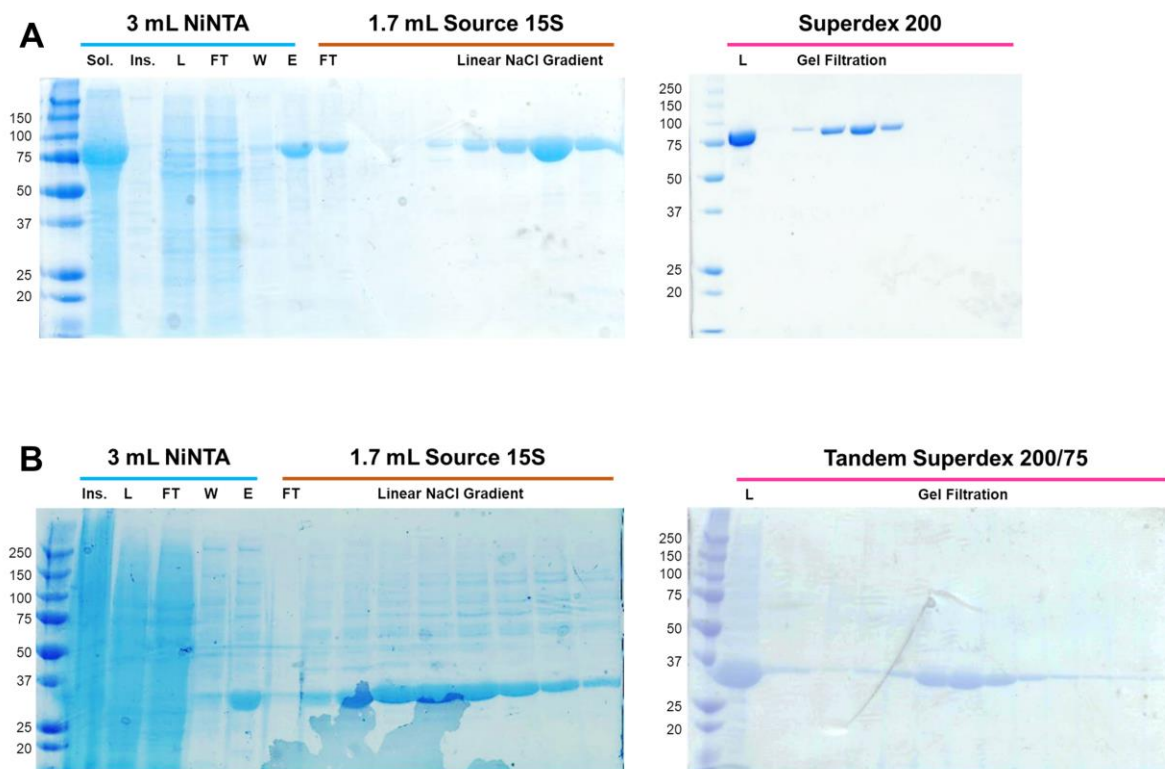


Figure 4.3. Representative purifications of bovine GRK2 and human Gβγ-C68S used in crystallization trials. SDS-PAGE analysis of **A**) bovine GRK2 NiNTA (blue bar), Source 15S (orange bar), and S75 size exclusion (pink bar) and **B**) human Gβγ NiNTA (blue bar), HiPrep Q XL (orange bar), and tandem S200/S75 size exclusion (pink bar) are indicated.

All four inhibitor complexes crystallized in space group $C222_1$ with nearly identical unit cell constants with resolution ranges of 2.56–3.26 Å (**Table 4.2**). In comparison to the previously reported structure of GSK180736A in complex with GRK2–Gβγ, all four inhibitor complexes exhibit nearly identical kinase domain conformations with differences in relative rotations between the large and small lobes no greater than 1°. This result is consistent with the idea that the indazole, which occupies the adenine subsite and forms two hydrogen bonds with the hinge of the kinase domain, dictates the overall conformation of the large and small lobes (79)(89).

As expected, the four inhibitors bind in the ATP pocket of GRK2 in essentially the same manner as the parent compound, GSK180736A, with the exception that the amide bond connecting the indazole and the dihydropyrimidine is flipped relative to the model of

Table 4.2. Refinement statistics of GRK2-G β γ -indazole inhibitor complexes

Inhibitor	CCG215022	CCG224062	CCG224406	CCG224411
X-ray source	APS 21-ID-G	APS 21-ID-G	APS 21-ID-G	APS 21-ID-G
wavelength (Å)	0.97857	0.97857	0.97857	0.97857
D_{\min} (Å)	30–2.6 (2.64–2.56)	30–3.2 (3.26–3.2)	30–2.8 (2.85–2.8)	30–2.8 (2.85–2.8)
space group	$C222_1$	$C222_1$	$C222_1$	$C222_1$
cell constants (Å)	$a=60.6, b=239.9,$ $c=208.9$	$a=62.0, b=241.4,$ $c=213.0$	$a=60.7, b=242.0,$ $c=213.7$	$a=60.0, b=239.4,$ $c=208.6$
unique reflections	47002 (2068)	27203 (1277)	37227 (1655)	36395 (1800)
R_{sym} (%)	6.7 (39.1)	14.6 (0.0)	5.5 (76.0)	10.4 (93.6)
completeness (%)	97.0 (86.1)	96.7 (92.3)	94.0 (84.5)	93.3 (93.5)
$\langle I \rangle / \langle \sigma \rangle$	25.8 (2.6)	17.8 (1.5)	20.3 (1.6)	19.6 (1.9)
redundancy	3.5 (2.5)	7.3 (6.9)	3.6 (2.7)	4.6 (4.5)
refinement resolution (Å)	30–2.6 (2.64–2.56)	30–3.2 (3.26–3.2)	30–2.8 (2.85–2.8)	30–2.8 (2.85–2.8)
total reflections used	44654	25783	35332	34492
RMSD bond lengths (Å)	0.0134	0.0115	0.0115	0.0122
RMSD bond angles (°)	1.6461	1.5718	1.5479	1.5667
est. coordinate error (Å)	0.254	0.373	0.311	0.291
Ramachandran Plot:				
most favored, outliers (%)	92.3, 0.8	89.3, 1.3	91.3, 0.5	90.3, 1.2
R_{work}	0.2048	0.1718	0.2021	0.1981
R_{free}	0.2640	0.2501	0.2773	0.2571
protein atoms	8178	8171	8218	8183
water molecules	29	34	31	40
inhibitor atoms	37	41	41	40
average B -factor (Å ²)	71.293	100.086	70.597	75.491
protein	71.545	100.593	71.040	75.617
inhibitor	65.215	112.409	61.873	119.909
MolProbity score	2.32	2.39	2.14	2.59
MolProbity $C\beta$ deviations	1	1	0	0
MolProbity bad backbone bonds	0	1	0	1
MolProbity bad backbone angles	1	1	1	0
PDB entry	5HE0	5HE1	5HE2	5HE3

GSK180736A (**Figure 4.4**). However, the electron density for this amide in the complex with GSK180736A is ambiguous, and hence the linker may adopt multiple configurations in the previous structure. As seen with GRK2-G β γ -GSK180736A, the indazole rings bind in the adenine subsite forming two hydrogen bonds with backbone atoms of the hinge residues Asp272 and Met274, and the dihydropyrimidine and fluorophenyl rings fill the ribose and polyphosphate subsites, respectively. However, the presence of the D rings, and presumably their interactions in the hydrophobic subsite, seems to alter the conformation of the A–C rings to some extent among the four complexes. Compared to the GRK2-G β γ -GSK180736A complex, the CCG215022,

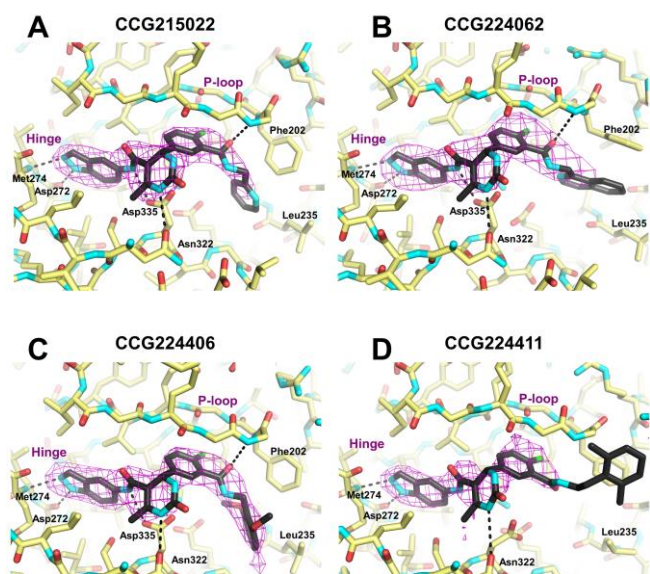


Figure 4.4. Co-crystal structures reveal that the inhibitors bind in the ATP-binding pocket in a similar conformation as the GSK180736A parent structure. 3σ $|F_o| - |F_c|$ omit maps of compounds A) CCG215022, B) CCG224062, C) CCG224406, and D) and a 2σ $|F_o| - |F_c|$ omit map of CCG224411 are represented as magenta wire cages superimposed onto the refined X-ray crystal structures. Hydrogen bonds with the labeled GRK2 residues are shown as black dashed lines. The P-loop and hinge region are indicated for reference.

CCG224062, and CCG224406 compounds form additional hydrogen bonds in the ribose subsite with Asp335 and Asn322. As predicted, their variable amide-linked D rings occupy the hydrophobic subsite of GRK2, and the carbonyls of the amide bond linker *ortho* to the fluorine atom in the C ring form a hydrogen bond with the backbone nitrogen of Phe202 in the P-loop. The D ring of CCG224411, however, flips out of the hydrophobic site towards the solvent, and there is no interpretable electron

density beyond the amide linker.

The largest conformational changes induced by the various inhibitors occur in the P-loop (**Figure 4.5**). Relative to GSK180736A, each of the four inhibitors causes the P-loop to shift away from the polyphosphate subsite as if to accommodate the terminal aromatic rings. Compounds CCG215022, CCG224406, and CCG224411 each have a maximum P-loop shift of 2.2 Å at the Gly201 $C\alpha$ relative to the parent structure. Compound CCG224062 demonstrates the largest P-loop shift of 3.0 Å, possibly because it has the bulkiest substituent. In addition, the benzene ring of Phe202 rotates to allow space for the terminal aromatic substituents depending on their orientation. Notably, AST-loop residues 487–493, which are typically ordered in active conformations of AGC kinases, but are disordered in most GRK2 kinase domain structures to

date, are visible in the CCG224406 electron density map and pack on top of the P-loop. The reason for these residues being more ordered in the CCG224406 complex relative to the others is unclear, but the density may simply reflect the higher quality of this particular crystallographic data set.

4.2.4.3. Molecular Basis for GRK2 Potency and Selectivity by the GSK180736A Derivatives

Analysis of these four crystal structures in comparison to structures of other AGC kinase domains provides insight into the molecular basis for their relative potencies and selectivities.

Consistent with previous studies (105, 112-113), the number of hydrogen bonds does not

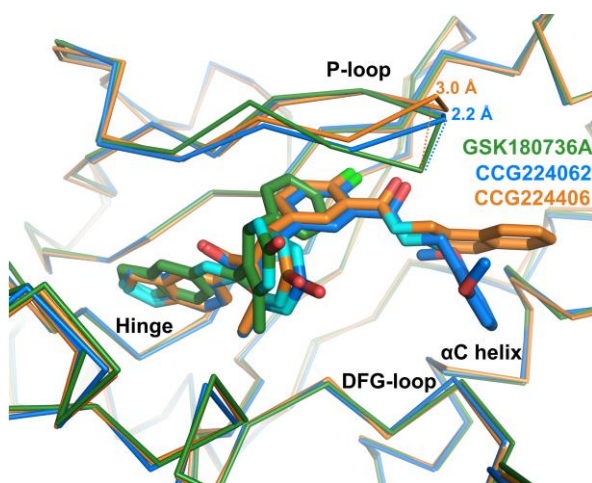


Figure 4.5. Adaptive structural changes in the GRK2 P-loop. Compared to the P-loop conformation when bound to compound GSK180736A (green), the C α carbon of Gly201 shifts away from the binding site by 2.2 Å when bound to CCG224406, CCG215022, or CCG224411 (not shown) and by 3.0 Å when bound to CCG224062 (orange). The magnitude of the shift thus appears to depend on the size of the D ring.

correlate well with inhibitor binding affinity in AGC kinases. For example, compound CCG224406 has the second highest affinity of the four crystallized compounds from this study and the parent compound GSK180736A, but only forms three hydrogen bonds. Plotting the K_i of 10 potent GRK2 inhibitors (calculated from the IC_{50} values using the Cheng–Prusoff transformation) versus both the number of hydrogen bonds and the buried

accessible surface area exhibited no correlation between the number of hydrogen bonds and K_i but did show a correlation between buried surface area and K_i (**Figure 4.6**). The buried accessible surface area is the most consistent determinant of inhibitor potency, as previously noted for GRK2 (105).

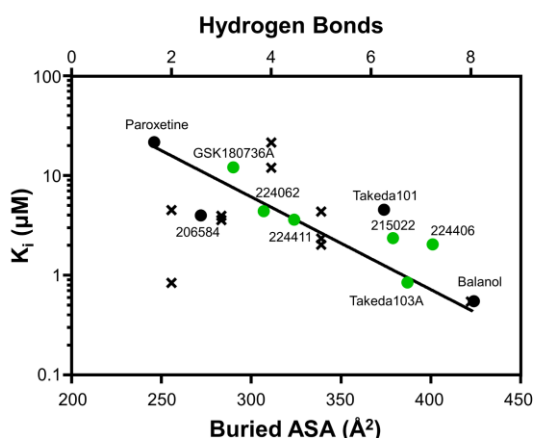


Figure 4.6. Structural determinants of inhibitor potency for GSK180736A derivative compounds. Inhibitor potency for GRK2 correlates with buried ASA ($R^2 = 0.8$) but not the number of hydrogen bonds ($R^2 = 0.01$). K_i values were calculated from experimentally determined IC_{50} values of the GRK2 inhibitors for which there is a crystal structure using the Cheng–Prusoff transformation and plotted as a function of both their buried ASA (circles) and the number of hydrogen bonds they form with GRK2 (\times 's). Buried ASA for inhibitors from this study are shown in green.

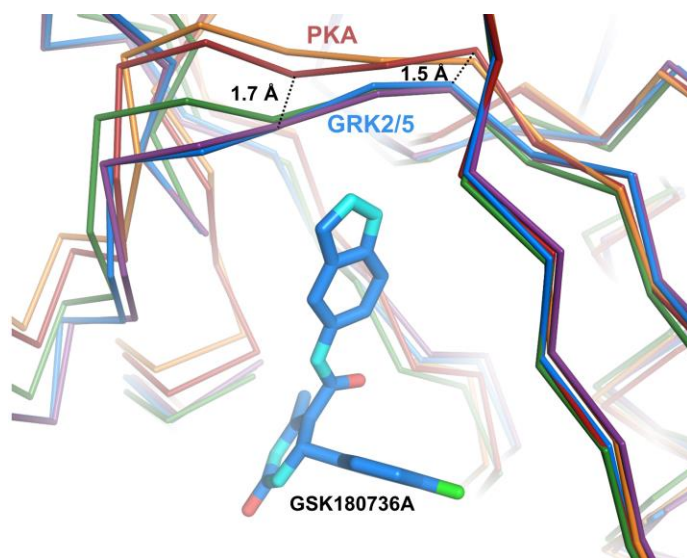


Figure 4.7. Structural differences in the hinge regions of PKA, GRK2, and GRK5. α traces of PKA bound to AMP-PNP (PDB ID 4HPT, red) or balanol (PDB ID 1BX6, orange), superimposed onto GRK2-GSK180736A (PDB ID 4PNK, blue). GRK2-CCG224406 (purple) and GRK5-CCG215022 (green) are also shown for comparison. Hinge residues that form hydrogen bonds with the indazole nitrogens of GSK180736A and its derivatives are 1.5–1.7 Å closer to the inhibitor in the structures of GRK2 and GRK5 relative to those of PKA.

Interestingly, neither GSK180736A nor any of its derivative compounds reported in this study inhibit PKA below concentrations of 30 μ M despite its kinase domain being highly homologous to those of GRKs and ROCK1. Comparison to both the PKA·AMPPNP substrate analog structure (PDB ID 4HPT) (114) and the PKA·balanol complex (PDB ID 1BX6) (7) indicates that the GSK180736A derivatives should not be sterically blocked from binding in the PKA binding site. However, the hinge in the structures of PKA is shifted 1.5–1.7 Å away from the adenine subsite relative to the position of the hinge in both GRK2 and GRK5 (Figure 4.7). This difference may prevent the formation of favorable contacts between hinge backbone atoms and the indazole ring common to GSK180736A and all of its derivatives.

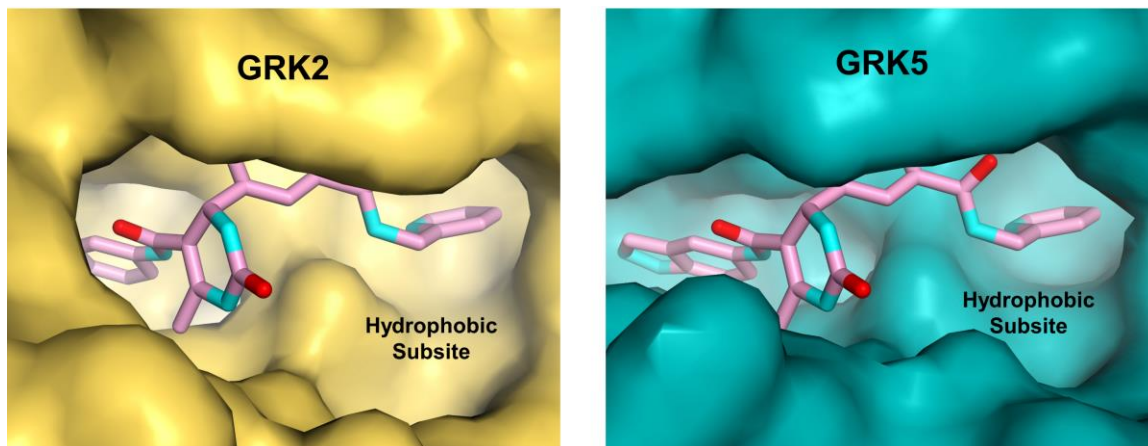


Figure 4.8. Comparison of GRK2 and GRK5 hydrophobic subsites when bound to CCG215022. A) GRK2 (PDB ID 5HE0, gold) (100) has a much wider and shallower binding pocket than B) GRK5 (PDB ID 4WNK, deep teal) (92).

Compounds GSK180736A, CCG224411, and CCG224406 do not bind tightly to either GRK1 or GRK5, but CCG215022 and CCG224062 inhibit these kinases with potencies in the low μM or nM range. To explore the molecular basis of this selectivity among GRK subfamilies, the structures of GRK5·CCG215022 (PDB ID 4WNK) (92) and GRK2·CCG215022 were compared. The hydrophobic subsite in GRK5 is deeper and narrower than that of GRK2 (92) (**Figure 4.8**). Thus, one would predict that compounds with larger D ring substituents would tend to be excluded from the hydrophobic subsite of GRK5. In the GRK5·CCG215022 complex, a hydrogen bond is formed between the catalytic lysine (Lys215 in GRK5) and the pyridine nitrogen of the inhibitor. In the crystal structure of GRK2·CCG215022, the pyridine nitrogen is modeled as facing the solvent because it is not in close enough proximity to any atoms capable of making hydrogen bonds (**Figure 4.4**). The fact that CCG215022 buries nearly identical surface area in each complex (only 5 \AA^2 additional buried surface area when bound to GRK5) is consistent with its similar potencies against GRK2 and GRK5 and its behavior as a pan-GRK inhibitor.

Based on the hydrophobic subsite hypothesis above, the isoquinoline ring of CCG224062 was predicted to select against GRK5 and its close homolog GRK1. However, it was an

efficacious inhibitor of all three GRKs as well as ROCK1, with 56-fold and 1000-fold increases in potency against GRK5 and GRK1 relative to the parent compound, GSK180736A. The crystal structure shows that the isoquinoline reorganizes local structure in the hydrophobic subsite of GRK2, in particular the P-loop, such that its benzyl ring forms a π - π stacking interaction with the side chain of Phe202. Superimposing CCG224062 from the GRK2-G $\beta\gamma$ structure in the active sites of GRK1 and GRK5 illustrates that the isoquinoline group would be compatible with their hydrophobic subsites as well, provided their P-loops can similarly reorganize. This modeling exercise also suggests that the nitrogen of the isoquinoline ring could form an additional hydrogen-bond with the active site lysine as CCG215022 does in GRK5. A greater degree of kinase domain closure in GRK1 and GRK5 relative to GRK2 may also account for why enhancement of potency is higher for GRK1 and GRK5.

The dimethoxybenzyl D ring of the most selective inhibitor, CCG224406, binds snugly in the hydrophobic subsite of GRK2 with one methoxy group packing deep in the pocket and the other projecting towards solvent (**Figure 4.4**). Docking the compound in the active site of GRK5 demonstrates that the 2,6-dimethoxybenzyl substituent of CCG224406 would collide with the

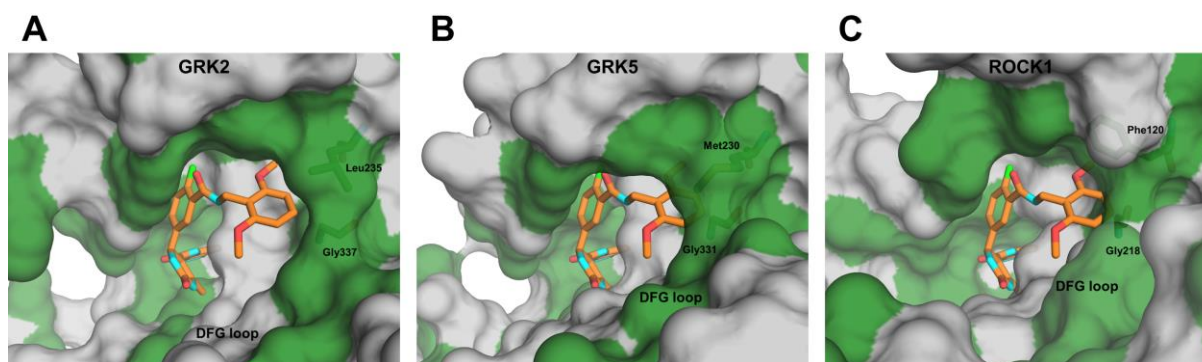


Figure 4.9. Molecular origins of selectivity for CCG224406. Surface representations of **A)** GRK2-CCG224406, **B)** GRK5 (PDB ID 4WNK), **C)** and ROCK1 (PDB ID 3V8S) with hydrophobic and polar/charged residues colored green and gray, respectively. CCG224406 is superimposed onto GRK5 and ROCK1 to demonstrate potential clashes. **B)** In GRK5, CCG224406 appears to clash with both Met230 from the α C helix (Leu235 in GRK2) and Gly331 from the DFG-loop (Gly337 in GRK2). **C)** In ROCK1, CCG224406 may clash with Phe120 (Leu-235 in GRK2) and backbone atoms of Gly218 in the DFG-loop (Gly337 in GRK2). For this modeled complex, ROCK1-Asp216 was changed to the rotamer of the analogous residue in the GRK2-CCG224406 complex (Asp335).

DFG-loop, which is shifted towards the hydrophobic subsite due to a greater degree of kinase domain closure in GRK5 than in GRK2 (**Figure 4.9**). The packing of CCG224406 is likely mimicked by the analogous potent *ortho*-methoxy hybrid. Movement of the methoxy substituent to the *meta* and *para* positions would cause the methoxy to collide with the α C-helix or DFG-loop, respectively, explaining their less favorable binding to GRK2.

Of the four inhibitors structurally characterized in this study, only CCG224406 achieves selectivity over both the GRK1 and GRK4 subfamilies and ROCK1. Upon superimposing these inhibitor structures on ROCK1 in complex with an indazole derivative similar to GSK180736A (3V8S) (115), it is apparent that ROCK1-Phe120 (Leu235 in GRK2) sterically clashes with each of the four structurally characterized inhibitor D rings (**Figure 4.9**). However, ROCK1-Phe120 must be able to adopt a rotamer more similar to that of GRK2-Leu235 because CCG215022, CCG224062, and CCG224411 all inhibit ROCK1 with high potency. Compound CCG224406, however, also sterically clashes with the backbone carbonyl of ROCK1-Gly218 (Gly337 in GRK2) in the DFG-loop, which is shifted towards the hydrophobic subsite by 2.9 Å in ROCK1 relative to GRK2. The other inhibitors avoid generating this collision but CCG224406 cannot, as a consequence of its two methoxy substituents, which greatly restrict its ability to alter its conformation within the hydrophobic subsite.

Electron density for the 2,6-dimethyl phenethyl moiety of CCG224411 is not evident after the amide linker (**Figure 4.4**), suggesting that this arm of the inhibitor is flexible while bound to GRK2. This flexibility likely results from the extra degree of rotational freedom conferred by the longer ethylene linker and its inability to be accommodated within the hydrophobic subsite. For the same reasons, the D ring of CCG224411 likely would not be able to occupy the hydrophobic subsites of GRK1 and GRK5. Thus, the compound would bind no better

than GSK180736A alone, consistent with the relatively poor binding of CCG224411 to GRK1 and GRK5.

4.2.4.4. Contractility in Mouse Cardiomyocytes with GSK180736A Derivatives

To ascertain the ability of these inhibitors to produce a myocardial effect, they were incubated with cardiomyocytes isolated from adult mice, and then stimulated with the β AR agonist isoproterenol as described previously (92). In the presence of a GRK2 inhibitor, the strength of the resulting contraction should increase as there is more β AR signaling. Previously, it was shown that paroxetine induces a significant increase in contractility in comparison to the DMSO control when dosed at 10 μ M (58). In comparison, GSK180736A showed similar efficacy as paroxetine when dosed at 1 μ M

(Figure 4.10), consistent with the increased potency of this compound towards GRK2 relative to paroxetine. Four hybrid molecules were evaluated for their effects on cardiomyocyte contractility: 12d,

CCG21522, 12m, and CCG224406. Two of these were highly selective for GRK2 (12m and CCG224406), while the other two were more balanced GRK2/GRK5 inhibitors (12d

and CCG215022). All of the hybrids proved to be equivalent to or slightly more potent than the lead GSK180736A at stimulating cardiomyocyte contraction. Unfortunately, it is not possible to draw any firm conclusions from this limited study regarding whether different levels of

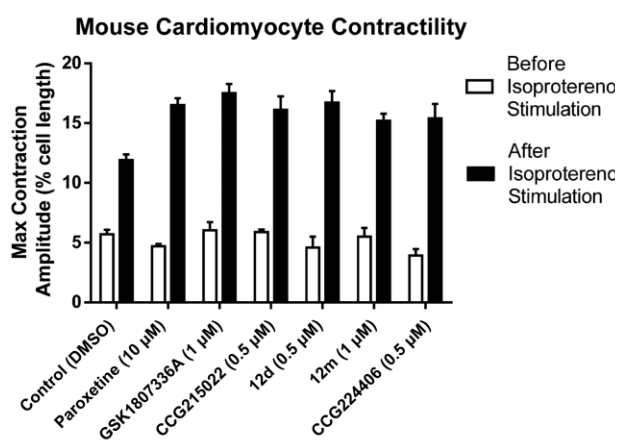


Figure 4.10. Cardiomyocyte contractility of GSK180736A derivatives. Maximum contraction amplitudes of the known GRK2 inhibitor paroxetine, GSK180736A, CCG215022, 12d, 12m, and CCG224406 before and after isoproterenol stimulation. Doses shown are the minimum inhibitory concentrations that exhibited a p-value <0.05 versus control. Values represent the mean \pm SEM for 8–10 cardiomyocytes.

selectivity for GRK2 vs. GRK5 lead to greater or lesser efficacy in the cardiomyocytes. The GRK2 selectivities in this group ranged from 2-fold (CCG215022) to >700-fold (12m and CCG224406), but no clear differences in cardiomyocyte potency are apparent. Interpretation of these results is further complicated by unknown differences in cell permeability of the hybrid analogs. Future studies may require the careful determination of IC₅₀ values with probes of known equivalent cell permeabilities to provide a definitive answer to what GRK inhibition selectivity profile is optimum for achieving maximum efficacy in cardiomyocytes.

4.2.5. GSK180736A Derivatives Summary

Utilizing a hybrid approach, we envisioned development of selective and potent GRK2 inhibitors constructed from the potent ROCK1 inhibitor GSK180736A and the selective GRK2 inhibitor Takeda103A. Overlaying the binding poses of the two compounds in the active site of GRK2 revealed that it may be possible to utilize the hydrophobic binding site of GRK2 to achieve selectivity over other AGC kinases (**Figure 4.2**). A small library of compounds was thus synthesized in which a variety of amide substituents were appended to the fluoro-aromatic ring of GSK180736A to mimic the difluorobenzyl amide of Takeda103A (**Table 4.1**). The major SAR findings from this study were that small benzyl amide substituents lead to significant inhibition of GRK5 in addition to GRK2 and that addition of steric bulk to the benzyl amides favors GRK2 selectivity over all of the other AGC kinases tested. This ultimately led to the identification of CCG224406, a 2,6-dimethoxybenzylamide with remarkable potency against and selectivity for GRK2 and complete loss of the ROCK inhibitory activity seen in GSK180736A. We also identified some potent pan-inhibitors of GRK1, 2 and 5, including 2-pyridyl amide CCG215022. Collectively these new hybrid analogs represent an important start in the design of

small molecule probes that can be used to explore the physiological roles of the individual GRKs.

Co-crystal structures of four representative analogs bound to GRK2 were determined to help define the molecular basis for their differing selectivities (**Figure 4.4**). Comparison of the GRK2·CCG215022 structure with the previously determined GRK5·CCG215022 crystal structure showed that the hydrophobic subsite of GRK5 is much narrower and deeper than the shallower, wider subsite of GRK2, helping to rationalize the increased GRK2 selectivity seen with bulkier D ring appendages (**Figure 4.8**). In addition, three other GRK2 inhibitor complexes were crystallized: GRK2-CCG224062, GRK2-CCG224406, and GRK2-CCG224411. Overall, the structures confirm that the size and shape of the hydrophobic subsite, which is in part dependent on the degree of kinase domain closure, put constraints on the chemical nature of the D ring amide substituent that can be accommodated. Larger substituents, such as the 2,6-dimethoxy benzyl of CCG224406, can fit into GRK2 more readily than the other AGC kinases tested in this study. These conclusions were supported by overlays of the bound poses of our analogs in GRK2 with other published kinase structures (**Figure 4.9**). Based on the published GRK5·CCG215022 structure and the selectivity data we observed, we also conclude that smaller hydrogen-bonding benzyl amides can interact effectively with the hydrophobic subsite of GRK5, conferring potent inhibitory activity to the GRK5-inactive GSK180736A.

Finally, evaluation of selected inhibitors in cardiomyocytes (**Figure 4.10**) suggests that pan-GRK inhibition or dual GRK2/GRK5 inhibition is just as effective as GRK2 inhibition alone at stimulating contraction in the failing heart, but further studies will be needed to confirm this hypothesis.

4.3. Structure-Based Design, Synthesis, and Biological Evaluation of Highly Selective and Potent GRK2 Inhibitors Based on Paroxetine

4.3.1. Foreword

Ideas and conclusions presented in Chapter 4B are published in the *Journal of Medicinal Chemistry* (116) and *Molecular Pharmacology* (117), including selected sections and figures which are copied verbatim. The first publication (116) was originally written primarily by Dr. Helen Waldschmidt and me, along with our mentors Dr. John Tesmer and Dr. Scott Larson. The second publication (117) was primarily written by Dr. Renee Bouley, Dr. Waldschmidt, and Dr. John Tesmer, with structural analysis contributions from me. Dr. Waldschmidt synthesized all compounds and performed radiometric IC₅₀ experiments with GRK1, 2, and 5. Dr. Kristoff Homan purified GRKs, Gβγ, and PKA, and crystallized and collected diffraction data for GRK2–Gβγ·CCG211998 and GRK2–Gβγ·CCG222886. Dr. Osvaldo Cruz purified, crystallized, and collected diffraction data for GRK2–Gβγ·CCG258208. Dr. Bouley crystallized, collected diffraction data, refined, and interpreted GRK2–Gβγ·257784 and GRK2–Gβγ·258748. With assistance from Dr. Cruz (CCG258208) and along with Dr. Tesmer, I refined and interpreted GRK2–Gβγ·CCG211998, GRK2–Gβγ·CCG222886, GRK2–Gβγ·258208, and GRK2–Gβγ·CCG224061. I performed ROCK1 and PKA inhibition assays. Drs. Alessandro Cannavo, Jianliang Song, Joseph Cheung, and Walter Koch isolated adult cardiomyocytes from mice and performed contractility assays. Dr. Cannavo and Dr. Koch analyzed the cardiomyocyte contractility data. Dr. Xin-Qiu Yao performed principal component analysis experiments.

4.3.2. Background

Because we had success with improving GRK2 potency and selectivity by modifying the GSK180736A scaffold to contain bulky substituents that form favorable van der Waals contacts within the hydrophobic subsite and are uniquely well-tolerated in GRK2, we next wanted to determine whether we could make similar improvements to the paroxetine scaffold. Paroxetine is an FDA-approved SSRI and, as such, has remarkably better pharmacokinetic properties than GSK180736A and its derivatives (118). Indeed, an *in vivo* assessment of paroxetine activity in mice after induction of myocardial infarction demonstrated improved left ventricular function, a decrease in maladaptive hypertrophy, and restored levels of circulating catecholamines and β AR density in mice treated with paroxetine for six weeks as compared to the vehicle (no treatment) and fluoxetine (an SSRI that does not inhibit GRK2 kinase activity) controls (58). In addition, paroxetine treatment preserved the heart function better than the current standard of care for heart failure, the β_1 AR blocker metoprolol (59). We were therefore eager to improve the GRK2 potency and selectivity of paroxetine with an eye towards developing improved therapeutics for heart failure.

4.3.3. Materials and Methods

4.3.3.1. Paroxetine Derivatives Library Construction

As with the GSK180736A derivative compounds, Dr. Waldschmidt synthesized a library of paroxetine derivative compounds by appending various amide-linked substituents of differing length, bulk, and chemical properties.

4.3.3.2. Pharmacological Assays

Dr. Waldschmidt determined IC₅₀s for GRK1, 2, and 5 using a radiometric assay. I determined PKA IC₅₀s and ROCK1 percent inhibition at 10 μ M inhibitor as described in Chapter 4A.

4.3.3.3. Structure Determination

I performed the structural refinement and analysis of four GRK2–G $\beta\gamma$ -inhibitor co-crystal structures whose X-ray data sets were collected by the previous Tesmer lab members who crystallized them (Dr. Homan, CCG211998, CCG222886, CCG224061; Dr. Cruz, CCG258208) but whose data refinement and analysis was not completed.

4.3.3.4. Mouse Cardiomyocyte Shortening Assays

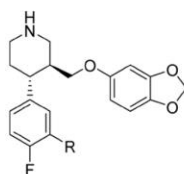
Myocyte shortening assays were performed in collaboration with Dr. Walter Koch's laboratory as described previously (100).

4.3.4. Results

4.3.4.1. Structure-Activity Relationships of the Paroxetine Derivative Compounds

Based on the GRK2–G $\beta\gamma$ -paroxetine crystal structure (3V5W) (58), we predicted that addition of an amide substituent *ortho* to the fluorine in the fluorophenyl ring of the paroxetine scaffold would result in a hydrogen-bond with the backbone nitrogen of Phe202, as we saw with the GSK180736A series (100). A methyl amide had a 2-fold decrease in GRK2 potency, but increasing the bulk and lipophilicity to a benzyl methylamide showed a 2-fold increase in GRK2 potency (**Table 4.3**). However, when we increased the lipophilicity by elongating the linker from methyl to ethyl or increased the bulk by fluorinating the 2- and 6-benzyl ring positions, GRK2 potency was decreased and some potency for GRK5 and ROCK1 was picked up, suggesting that increased bulk and lipophilicity are not sufficient to enhance GRK2 potency and selectivity in

Table 4.3. Inhibitory activity of paroxetine derivative compounds



R	Compound	GRK2 IC ₅₀ (μM) ^a	GRK1 IC ₅₀ (μM) ^a	GRK5 IC ₅₀ (μM) ^a	PKA IC ₅₀ (μM) ^a	ROCK1* IC ₅₀ (μM) ^a
H	Paroxetine	1.38±1.00	> 100	> 100	> 100	10%
n/a	Takeda103A	0.02±0.001	9.1±3.2	2.2±0.9	ND	ND
n/a	GSK180736A	0.03±0.006	52.1±26.3	9.2±3.0	ND	ND
n/a	3	0.77±0.5	> 100	> 100	30±19	65%
n/a	4	0.13±0.03	>100	>100	>100	0%*
	14aa	2.1±0.72	> 100	> 100	> 100	11%
	14ab	0.77±0.17	> 100	84.3±35.8	> 100	17%
	14ac	2.68±2.11	> 100	> 100	> 100	22%
	14ad	1.53±0.49	> 100	37.2±28.9	> 100	34%
	14ae	2.03±0.33	> 100	10.2±1.8	> 100	0%
	14af	12.4±7.7	> 100	75.7±39.9	> 100	5%
	14ag	2.17±0.79	24.5±19.6	42.3±16.3	> 100	0%
	14ah	1.76±1.43	25.8±16.1	33.2±2.48	> 100	0%
	14ai	2.04±1.02	32.0±14.0	38.4±16.1	>100	13%
	14aj	37.7±9.14	> 100	> 100	> 100	1%
	14ba	2.37±2.27	> 100	> 100	25.8±25	18%
	CCG211998	0.61±0.12	> 100	17.1±5.9	> 100	6%
	14al	1.52±0.78	> 100	76.3±15.3	> 100	6%
R	Compound	GRK2 IC ₅₀ (μM) ^a	GRK1 IC ₅₀ (μM) ^a	GRK5 IC ₅₀ (μM) ^a	PKA IC ₅₀ (μM) ^a	ROCK1* IC ₅₀ (μM) ^a
	14am	2.04±0.74	> 100	> 100	> 100	8%
	14an	3.28±1.8	> 100	> 100	> 100	15%
	14ao	3.02±0.99	> 100	> 100	> 100	18%
	14ap	3.24±1.0	> 100	> 100	> 100	21%
	14bb	6.01±2.08	60.0±2.07	> 100	48.2±35	0%
	14bc	5.9±3.2	> 100	> 100	> 100	0%
	14aq	0.75±0.32	> 100	14.8±3.2	> 100	18%
	14ar	0.6±0.21	> 100	> 100	> 100	11%
	CCG258208	0.03±0.001	87.3±27.9	7.09±0.73	> 100	9%
	14at	0.77±0.20	> 100	> 100	> 100	18%
	14au	0.03±0.02	86.5±7.0	4.0±0.52	> 100	12%
	14av	1.25±0.30	> 100	> 100	> 100	17%
	14aw	2.11±0.52	> 100	> 100	> 100	14%
	14ax	0.39±0.11	> 100	> 100	> 100	19%
	14ay	16.7±5.4	> 100	> 100	> 100	13%
	CCG222886	0.63±0.33	> 100	> 100	> 100	27%

All IC₅₀ values are the average of $n = 3$ experiments. Error shown represents standard error of the mean. *Percent inhibition at 10 μM ROCK1.

the context of the paroxetine scaffold. When we directly compared the appendages that gave the best improvements in GRK2 potency and selectivity from our GSK180736A series (2,6-dimethyl, 2,6-dichloro, and 2,6-dimethoxy benzyl methylamide) to the paroxetine scaffold, we found that they all decreased GRK2 potency and picked up significant inhibitor activity towards the other GRKs, showing that the GSK180736A SAR is not translatable to the paroxetine

scaffold despite very similar binding poses of the bare scaffolds to GRK2. We believe that differences in the indazole (GSK180736A) and benzodioxole (paroxetine) A ring hinge binding moieties affect the orientation of the scaffold extensions and their ability to engage with the hydrophobic subsite. Indeed, comparison of GRK2– $G\beta\gamma$ ·GSK180736A (4PNK) and GRK2– $G\beta\gamma$ ·paroxetine (3V5W) crystal structures shows that the kinase domain adopts a more closed conformation in the GSK180736A complex because of differences in their hinge binding moieties, which translates to small but significant structural differences at the ribose and polyphosphate subsites.

Because the GSK180736A scaffold extensions did not translate to improved GRK2 potency and selectivity, we next explored more polar ring systems. In the previously determined GRK5·215022 crystal structure (4WNK) (92), which contains a 2-pyridyl methylamide, the pyridyl nitrogen engages in a stabilizing hydrogen-bond with the catalytic Lys 220 (Lys215 in GRK2). We thus examined the analogous hydrophobic substituent on the paroxetine scaffold (CCG211998) and found a 2-fold increase in potency for GRK2. Although this compound lost GRK2 selectivity because it picked up potency for GRK5, this polar ring substituent was our first indication of improved GRK2 potency within the paroxetine derivative compounds. To test the importance of the 2-pyridyl position, we either moved the nitrogen around the ring or elongated the linker and found that in all cases, potency for GRK2 was decreased, suggesting that the position of the 2-pyridyl nitrogen relative to the fluorophenyl ring is essential for its inhibitor activity in GRK2.

Encouraged by the improvement in GRK2 potency we saw with the 2-pyridyl methylamide of CCG211998, we investigated other hydrogen-bond acceptors predicted to take the position of the 2-pyridyl nitrogen in CCG211998. First we assessed the activity of 2-

imidazolyl methylamides and found that they are essentially equipotent with CCG211998. A non-homologated 2-imidazolyl methylamide is also equipotent with CCG211998 for GRK5, perhaps by making the analogous hydrogen-bond with the catalytic lysine as seen in the GRK5·CCG215022 crystal structure. Next, we replaced the imidazolyl methylamide with 3-pyrazolyl methylamide to create CCG258208 and observed a drastic improvement in GRK2 potency ($IC_{50} = 30$ nM). This high potency in combination with the >200-fold selectivity over the other GRKs tested and >2500-fold selectivity over ROCK1 and PKA make CCG258208 our most potent and selective GRK2 inhibitor from this study. The proper positioning of both nitrogens in the pyrazole ring is essential for the potency of GRK2, as either elongating the linker or methylating either of the two ring nitrogens drastically reduced GRK2 potency. Also, transposition of the pyrazole nitrogens around the ring reduced GRK2 potency, and homologating the linker to create CCG222886 could not rescue inhibition. Taken together, these results suggest that both pyrazole nitrogens of CCG258208 are involved in making important polar interactions with GRK2.

4.3.4.2. GRK2–G $\beta\gamma$ Co-crystal Structure Analysis with CCG211998, CCG222886, and CCG258208

The co-crystallization of GRK2–G $\beta\gamma$ with CCG211998, CCG222886, and CCG258208 were instrumental in providing structural explanations for the differences in potency and selectivity among the paroxetine derivatives. Additionally, CCG224061, which has no hydrophobic site extension and is a hybrid between the paroxetine and GSK180736A scaffolds, was structurally characterized to more directly assess the importance of interactions at the hinge.

CCG222886 and CCG258208 crystallized in *C2* at 2.2 and 3.0 Å resolutions, respectively. CCG211998 was unusual in that it crystallized at 2.6 Å in *P2*, a space group we had

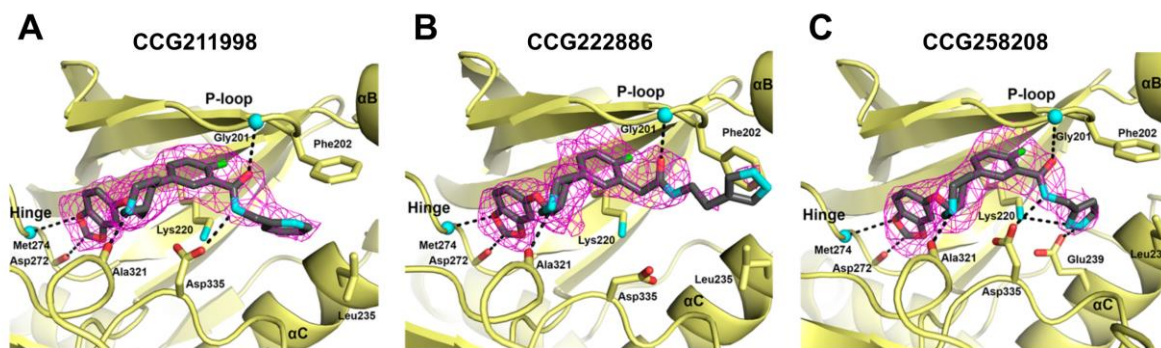


Figure 4.11. GRK2-G $\beta\gamma$ -inhibitor co-crystal structures with paroxetine derivative compounds. Omit map density is shown as magenta wire cages for A) CCG211998, B) CCG222886, and C) CCG258208.

not observed in any other GRK crystal structure, perhaps explaining several unique conformational changes in its kinase domain (**Table 4.4**). All three inhibitors bind similarly to the paroxetine parent molecule, although differences in their D ring substituents cause minor rearrangements in their A, B, and C rings (**Figure 4.11**). Consistent with the paroxetine structure, all three inhibitors form the predicted hinge interactions through their benzodioxole A rings, with the piperidine B ring sitting puckered in the ribose subsite making a hydrogen bond with the backbone carbonyl of Ala321 and the fluorophenyl C ring packing under the P-loop in the polyphosphate subsite. As seen in our GSK180736A derivatives, the carbonyl of the amide linker in all three inhibitors forms a hydrogen bond with the backbone nitrogen of Gly201 in the P-loop. Beyond the amide of CCG222886, the electron density of the linker and pyrazole substituent is poor, likely because it extends out of the active site into the solvent. The extra methylenes between both the amide and C ring and the amide and D ring in CCG222886 increase the linker so much that it cannot pack into the hydrophobic subsite. In contrast, the CCG211998 and CCG258208 D rings do engage with the hydrophobic subsite. The amide nitrogens in CCG211998 and CCG258208 can also make an extra hydrogen bond with the side chain of Asp335 that is not seen in CCG222886, which is also a consequence of the homologated linker in CCG222886 which moves its amide nitrogen out of reach of Asp335.

Table 4.4. Refinement statistics of GRK2-G β γ -benzodioxole inhibitor complexes

Ligand	CCG211998	CCG222886	CCG258208	CCG224061
X-ray source	APS 21-ID-G	APS 21-ID-G	APS 21-ID-D	
wavelength (Å)	0.9785	0.9786	0.9785	1.1271
D_{\min} (Å)	50.00-2.60 (2.64-2.60)	50.00-2.15 (2.19-2.15)	30-3.0 (3.04-3.03)	40-3.1 (3.15-3.1)
space group	$P12_1$	$C12_1$	$C12_1$	$C222_1$
unit cell constants (Å)	$a=113.1,$ $b=62.4,$ $c=102.0$ $\alpha=90.0,$ $\beta=92.8,$ $\gamma=90.0$	$a=194.3,$ $b=71.4,$ $c=111.3$ $\alpha=90.0,$ $\beta=110.5,$ $\gamma=90.0$	$a=189.0,$ $b=74.2,$ $c=123.2$ $\alpha=90.0,$ $\beta=115.5,$ $\gamma=90.0$	$a = 61.0,$ $b = 240.1,$ $c = 211.6$
unique reflections	39963 (1987)	77337 (3805)	29942 (4657)	28709 (1399)
R_{sym} (%)	9.8	16.1	12.9	3.9 (3.9)
completeness (%)	85.8	99.0	98.5	7.5 (34.8)
$\langle I \rangle / \langle \sigma \rangle$	9.2 (0.8)	24.9 (1.4)	12.8 (2.0)	98 (99)
redundancy	2.6 (2.5)	18.3 (11.2)	6.8 (6.8)	20.8 (2.7)
refinement resolution (Å)	30.00-2.60 (2.69-2.60)	30.00-2.15 (2.23-2.15)	30.00-3.03 (3.14-3.03)	39.98-3.1
total reflections used	35989	73370	207836	28248
RMSD bond lengths (Å)	0.011	0.018	0.012	0.002
RMSD bond angles ($^\circ$)	1.53	1.90	1.56	0.45
est. coordinate error (Å)	0.360	0.142	0.404	
Ramachandran Plot:				
most favored, allowed, outliers (%)	92.5, 5.6, 1.9	95.3, 3.8, 0.9	93.2, 5.3, 1.8	95, 0.4, 0
R_{work}	0.2207	0.1821	0.1971	0.1877
R_{free}	0.2807	0.2275	0.2516	0.2323
protein atoms	8089	8261	8192	8162
water molecules	43	388	23	4
inhibitor atoms	34	35	33	25
average B -factor (Å ²)	80.2	55.2	105.0	87.98
protein	80.3	55.6	105.0	88.01
inhibitor	70.2	69.3	123.3	85.59
MolProbity score	2.01	1.70	1.74	ND
MolProbity % $C\beta$ deviations	0	0.52	0	ND
MolProbity % bad backbone bonds	0	0.04	0.01	ND
MolProbity % bad backbone angles	0	0.05	0.01	ND
PDB entry	5UKK	5UKL	5UKM	5WG5

4.3.4.3. Molecular Determinants of GRK2 Potency and Selectivity by the Paroxetine

Derivatives

The conformation of GRK2 from the CCG222886 complex was the most analogous to the parent paroxetine complex, with an r.m.s.d. of 0.22 Å for the $C\alpha$ atoms in the small lobe of the kinase domain between the two structures. The close structural alignment is consistent with

our SAR, as CCG222886 has only a 2-fold increase in potency over paroxetine but retains selectivity over GRK1 and GRK5. This small increase in GRK2 potency with CCG222886 is most likely a result of additional buried surface area, a key feature for GRK2 inhibitors as seen in the GSK180736A derivatives (100).

CCG211998 adopts a unique space group (*P2*), which may explain several structural differences unique to this complex. It has the largest overall structural variation from GRK2–*Gβγ*-paroxetine, with an r.m.s.d. of 0.76 Å, and the relative orientation of the small and large lobes of the kinase domain differs by 15° (**Figure 4.15B**). Packing of the 2-pyridine substituent into the hydrophobic subsite causes a 1.3 Å shift of the α B-loop and its adjoining loops away from the active site. These changes are probably responsible for the unique crystal form that this complex adopts. Our SAR demonstrated that the position of the nitrogen was essential for activity, as moving the nitrogen to the 3- and 4- positions decreased GRK2 potency, leading us to hypothesize a hydrogen bond with the catalytic Lys220 as seen in the GRK5·CCG215022 crystal structure. However, we have the pyridine nitrogen modeled facing the solvent because it would be too distant (4.5 Å) and not in the proper orientation to form a hydrogen bond with Lys220 if the ring were rotated. The loss in GRK2 potency upon migrating this nitrogen around the pyridine ring may be a consequence of the loss of lipophilicity at those positions, which can make van der Waals contacts with the hydrophobic subsite as it is modeled in the CCG211998 structure.

The non-homologated pyrazole substituent of CCG258208 packs into the hydrophobic subsite, although it sits lower in the site than the pyridine of CCG211998. As we predicted from our SAR, both pyrazole nitrogens make important contacts as seen by their hydrogen bonds with Glu239 and Lys220. The α B-helix in the CCG258208 is not pushed away from the active site as

was seen with CCG211998, and instead aligns much more closely with α B-helix from the GRK2–G β γ -paroxetine structure, suggesting that binding of the pyrazole in the hydrophobic subsite does not require the conformational change of the kinase domain seen for CCG211998. Overall, we conclude that the drastic increase in GRK2 potency observed with CCG258208 is a consequence of its increased buried surface area and extra hydrogen bonds made between both pyrazole nitrogens with Lys220 and Glu239 that lock it in a stable conformation within the active site.

Without a crystal structure of GRK5 in complex with one of our paroxetine-derived compounds, the ability of these paroxetine derivatives to retain such high selectivity over GRK5 remains unclear. We have observed that the hydrophobic subsite in GRK2 can accommodate bulkier D rings than GRK5 (92, 100, 118). Furthermore, of the compounds reported here, only those with non-homologated amide linkages exhibit any potency for GRK5, suggesting that the hydrogen bond formed between the amide nitrogen and GRK2-Asp335 (GRK5-Asp329) is important for potency against GRK5. Inhibitory activity of the non-homologated paroxetine derivatives towards GRK5 may also be a consequence of the shorter linker, which may allow them to pack into the hydrophobic subsite where they can make stabilizing interactions. The non-homologated methylene-linked pyrazole, CCG258208, exhibits the highest potency for GRK5 (but retains over 100-fold selectivity for GRK2), consistent with the idea that hydrogen bond formation by the amide linker in combination with favorable polar contacts is similarly important for GRK5 potency. Thus, it seems most likely that differences in the kinase domain hinges and, consequently, the overall conformation of the GRK2 and GRK5 kinase domains, are responsible for the observed selectivity in the paroxetine-derived compounds. For example, if one overlays the small lobe of the GRK2–G β γ -CCG258208 complex with that of the GRK5-CCG215022

complex, the glycine in the DFG-loop of the large lobe of GRK5 would sterically collide with the pyrazole of CCG258208. The preferred conformation of the GRK5 hinge may engender less optimal interactions with the benzodioxole of paroxetine derived inhibitors.

4.3.4.4. Mouse Cardiomyocyte Contractility Assays with Paroxetine Derivatives

As an underlying mechanism of heart failure is the inability of the heart to properly contract, we selected compounds CCG211998 and CCG258208 in addition to Takeda101 (a close homolog of Takeda103A) for evaluation in an *ex vivo* contractility assay. Following

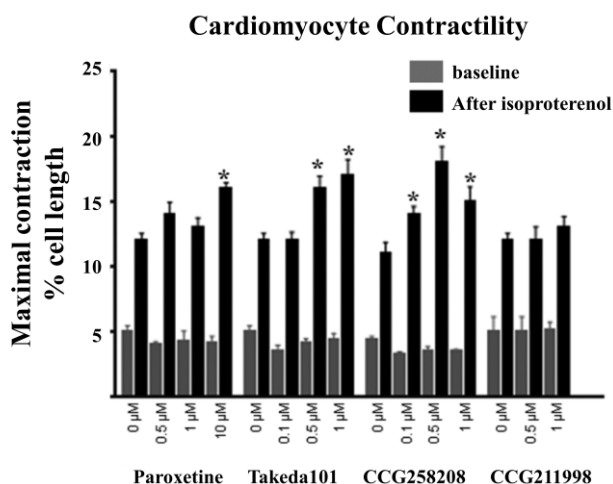


Figure 4.12. Cardiomyocyte contractility of paroxetine-derivative compounds. Contractility in murine cardiomyocytes of paroxetine, Takeda101, CCG258208, and CCG211998 at varying concentrations. After addition of the β AR agonist, isoproterenol, an increase in maximal contraction is observed (black bars) with respect to no isoproterenol stimulation (gray). Values represent the mean \pm SEM for 6–8 cardiomyocytes. Statistically significant difference was determined by a one-way ANOVA followed by Dunnett’s test. Statistical significance (*) was accepted at $p < 0.05$ vs DMSO control.

incubation with varying doses of the inhibitors to give a baseline contraction, mouse cardiomyocytes were then stimulated with the β AR agonist isoproterenol. The resulting maximal increase in contraction was then measured (Figure 4.12) (92). As inhibition of GRK2 should increase the number of activated β ARs, we would expect our inhibitors to enhance the maximal increase in comparison to a DMSO control. Previously, we showed

that both paroxetine and GSK180736A produce an increase in contractility. The minimum dose needed for paroxetine to produce a significant response was 10 μ M, whereas GSK180736A showed similar efficacy at 1 μ M (58, 100). These results agree with the higher potency of GSK180736A relative to paroxetine.

Evaluation of CCG211998 in the cardiomyocyte contractility assay did not show a significant increase in contractility at 0.5 or 1 μM , consistent with its modest 2-fold increase in GRK2 inhibition potency. The highly potent CCG258208, on the other hand, showed a significant increase in contractility at a concentration of only 0.1 μM , a 100-fold lower concentration than paroxetine, consistent with the approximately 50-fold increase in potency CCG258208 has for GRK2 relative to paroxetine. Additionally, CCG258208 showed a 5-fold improvement over Takeda101, although both compounds had equal potency for GRK2 (30 nM), suggesting that CCG258208 may have better cell permeability. In comparison to our previously reported compound CCG224406, this paroxetine hybrid inhibitor also shows a 5-fold improvement in efficacy (100). Importantly, these results suggest that significant improvement in βAR -stimulated contractility in mouse cardiomyocytes can be achieved with potent GRK2-selective inhibition.

4.3.4.5. Role of the Hinge Binding Moiety

To further investigate the importance of the hinge binding moiety, we investigated a paroxetine–GSK180736A hybrid scaffold, CCG224061, and a library of CCG224061 derivatives predicted to engage the hydrophobic subsite. In this hybrid scaffold, the hinge-binding A ring is

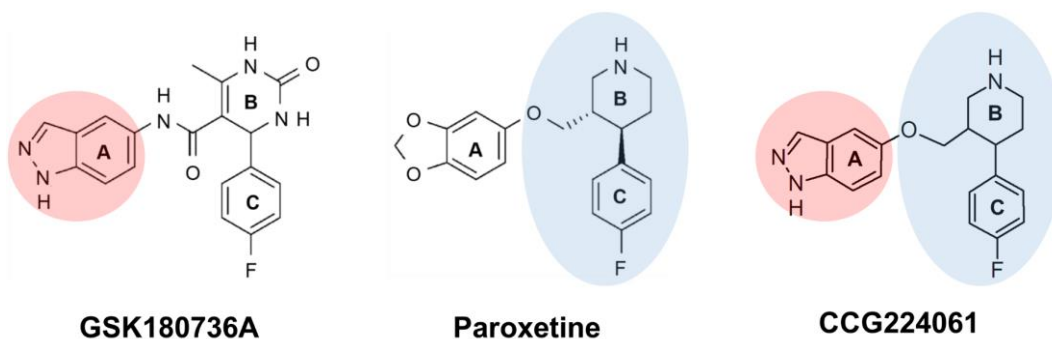
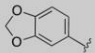
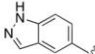
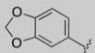
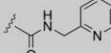
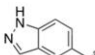
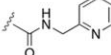
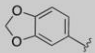
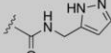
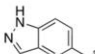
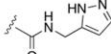


Figure 4.13. CCG224061 is a hybrid between GSK180736A and paroxetine. The benzodioxole of paroxetine is replaced with the indazole hinge binding moiety of GSK180736A.

an indazole as in GSK180736A, and the rest of the scaffold is derived from paroxetine (ether-linked piperidine B ring and fluorophenyl C ring) (**Figure 4.13**). We hypothesized that exchanging the benzodioxole of paroxetine with an indazole would increase potency as a result of its stronger interactions with the GRK hinge through two canonical hydrogen bonds, as opposed to the single hydrogen bond and weaker carbon-oxygen hydrogen bond found in paroxetine and its derivatives (**Figure 4.2**). In general, we found that exchanging the benzodioxole for an indazole increased potency for all of the GRKs tested, leading to an increase in GRK2 potency but a loss in GRK2 selectivity (**Table 4.5**). For example, the GRK2 potency of CCG224061 was increased 50-fold ($IC_{50} = 66 \text{ nM}$) over paroxetine ($IC_{50} = 1.4 \text{ } \mu\text{M}$); however this change to the hinge-binding moiety also resulted in increased potency for GRK1 ($IC_{50} = 6.4 \text{ } \mu\text{M}$), GRK5 ($IC_{50} = 1.3 \text{ } \mu\text{M}$), PKA ($IC_{50} = 3.1 \text{ } \mu\text{M}$), and ROCK1 (100% inhibition at $10 \text{ } \mu\text{M}$), all of which have IC_{50} s $> 100 \text{ } \mu\text{M}$ for paroxetine.

Table 4.5. SAR of the hinge binding moiety

Inhibitor	R ¹	R ²	GRK2 IC_{50} (μM)	GRK5 IC_{50} (μM)	GRK1 IC_{50} (μM)
Paroxetine		H	1.4	>100	>100
224061		H	0.07	1.3	6.4
211998			0.61	17	>100
257284			0.10	0.49	3.9
258208			0.03	7.1	87
258748			0.008	0.24	4.4

indazole hinge-binders in PC1 (117). In contrast, there is much more flexibility in the kinase domain conformations of GRK2 co-crystal structures with the benzodioxole compounds, as seen when their kinase domains are aligned by their small lobes (**Figure 4.15**). The ability of the benzodioxole compounds to bind to a spectrum of open and closed kinase domain conformations, as opposed to the single kinase domain configuration for the indazole compounds, is reflected in a wider variety of crystallization space groups (*C2*: paroxetine, CCG222886, and CCG258208; and *P2*: CCG211998) as well as spanning more conformational space along PC1.

4.3.5. Paroxetine Derivatives Summary

After successfully developing potent and selective GRK2 inhibitors starting from the GSK180736A scaffold by appending bulky substituents designed to occupy the hydrophobic subsite, we used the same approach with the paroxetine scaffold to improve GRK2 potency and selectivity on a molecule with better starting pharmacokinetics. Although we found that the

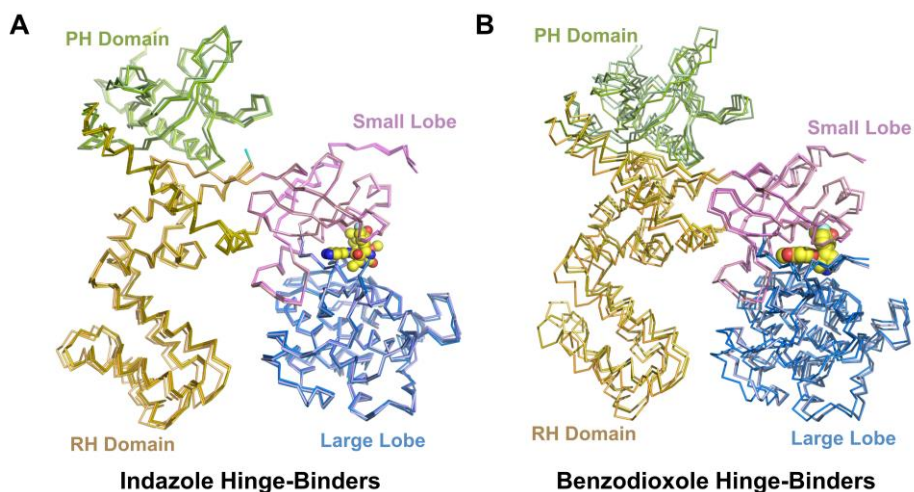


Figure 4.15. Comparison of GRK2 when indazole or benzodioxole hinge-binding compounds are bound. A) Indazole hinge binders have considerably less conformational flexibility than **B)** benzodioxole hinge binders. GRK2 backbone atoms are aligned by their small kinase domain lobes.

GSK180736A SAR was not translatable to the paroxetine scaffold, we discovered that smaller

polar heterocycles were favorable for GRK2 binding, leading to CCG258208 which is even more potent and selective (GRK2 IC_{50} = 30 nM, >200-fold selectivity over GRKs, >2500-fold selectivity over PKA and ROCK1) than our best compound, CCG224406, from the GSK180736A series.

Co-crystal structures with three paroxetine derivatives provided structural evidence for the enhanced selectivity of the paroxetine series. All three paroxetine derivative co-crystal structures described in this study revealed additional hydrogen bonds with the amide linker and additional buried surface area in the hydrophobic subsite as compared to the paroxetine complex, consistent with their higher GRK2 potency. Although non-homologated paroxetine derivatives with short linkers had the ability to gain GRK5 potency, perhaps by engaging with the GRK5 hydrophobic subsite, the paroxetine series maintained high selectivity for GRK2. In particular, stabilizing hydrogen bonds with the catalytic Lys220 and Glu239 made by both nitrogens of the pyrazole ring of our most potent GRK2 inhibitor, CCG258208, emphasized the importance of the positioning of these polar contacts within the hydrophobic subsite. In addition, the paroxetine derivatives demonstrated a more open kinase domain conformation as compared to GSK180736A and its derivatives, perhaps as a consequence of how the benzodioxole group interacts with the hinge through both a canonical hydrogen bond and a weaker carbon-oxygen hydrogen bond. This selectivity for GRK2 through hinge binding suggests that GRK2 has the innate ability to tolerate the weaker interactions with the benzodioxole better than its GRK1 and GRK5 counterparts.

4.4. GRK2-Selective Inhibitor Conclusions

Because GRKs are members of the broader AGC kinase structural superfamily, which is made up of 60 kinases with highly structurally similar kinase domains that all play important

regulatory roles in the cell (32), GRK inhibitor design comes with the challenge of developing compounds that are uniquely complementary to a single ATP-binding site within a sea of closely related kinases. This challenge is worth overcoming, because the selective inhibition of GRK2 has been shown to have positive outcomes for heart failure in a number of *in vivo* mouse models. A growing need for improved heart failure therapeutics is evidenced by the fact that 5.7 million people in the United States suffer from heart failure, and up to 30% of patients hospitalized for heart failure will die within one year of hospitalization. The current standard for heart failure care is the use of beta-blockers, but paroxetine, an SSRI with GRK2 inhibitory activity, has been shown to improve heart function better than the most widely used beta-blocker, metoprolol (59).

GRK2 and GRK5 are the most highly expressed GRKs in the normally functioning heart. In addition, both GRK2 and GRK5 are upregulated in patients with heart failure, contributing to the pathological sympathetic nervous system overdrive response associated with heart failure (48). When the potential therapeutic benefits of GRK inhibition for heart failure were initially discovered, Takeda Pharmaceuticals developed a series of highly potent GRK2-specific inhibitors, including Takeda103A (GRK2 $IC_{50} = 20$ nM) (103). Although these inhibitors demonstrated poor bioavailability, they showed that GRK2 can be specifically targeted despite having close structural relatives in the AGC superfamily. High-throughput screens performed by the Tesmer lab later identified GSK180736A and paroxetine as additional GRK2-selective inhibitors with modest potency; however, GSK180736A was not totally selective, as it had high potency for ROCK1, and paroxetine had only modest GRK2 potency at 1.4 μ M (58, 101). We thus devoted significant effort to designing highly potent and selective GRK2 inhibitors, with the overall goal of developing molecules that may be improve upon the currently available heart failure therapies.

Using the combined medicinal chemistry expertise from Helen Waldschmidt, and pharmacology, X-ray crystallography, and structural analysis expertise from various members in the Tesmer lab, we assessed the structure-activity relationships (SAR) of libraries of compounds starting from GSK180736A and paroxetine scaffolds. SAR from the GSK180736A series showed that bulkier substituents that occupy the more spacious hydrophobic subsite of GRK2 (as compared to its GRK1 and GRK5 counterparts) confer high GRK2 potency and selectivity. This led to our most potent and selective compound from the GSK180736A series (CCG224406), which showed a 6-fold improvement in potency ($IC_{50} = 130$ nM) over GSK180736A ($IC_{50} = 770$ nM) and over 700-fold selectivity over representative members of the other GRK subfamilies, PKA, and ROCK1 (100). SAR of the paroxetine series showed that, although the same substituents from the GSK180736A library did not always confer higher potency in GRK2, the addition of small, polar heterocycles was favorable. In particular, CCG258208 was found to engage with the hydrophobic subsite through non-polar contacts, as well as make two additional stabilizing hydrogen bonds through carefully positioned nitrogens in its pyrazole ring. This compound had even better potency ($IC_{50} = 30$ nM) and selectivity for GRK2 (>200-fold over other GRKs, and >2500-fold over ROCK1 and PKA) (119).

Importantly, structural comparison of co-crystal structures with all of our paroxetine (benzodioxole), GSK180736A (indazole), and hybrid scaffolds and their derivative compounds provided significant insight into the importance of the hinge-binding moiety on the conformation adopted by the kinase domain. We found that the more stable hydrogen bonds made by the indazole hinge-binders were well-tolerated in all of the GRKs and other AGC kinases, although GRK2 selectivity could be maintained through particular extensions into the hydrophobic subsite. Thus, indazole hinge-binders led to our most potent GRK2 inhibitors, but with decreased

GRK2 selectivity. In addition, some indazole hinge-binding compounds were found to be pan-GRK inhibitors that may be useful as more promiscuous chemical probes. In contrast, weaker interactions with the hinge made by the single canonical hydrogen bond and less favorable carbon-oxygen hydrogen bond of the benzodioxole hinge-binding moiety conferred high specificity to GRK2, which seems to have the innate ability to tolerate this weaker hinge interaction better than other AGC kinases and GRKs tested. We believe the ability of GRK2 to tolerate the benzodioxole is a result of its increased kinase domain conformational flexibility which can adjust to accommodate different chemical probes (117).

Finally, we were able to gain additional insight into the global kinase domain conformations adopted by these two series of compounds by plotting their co-crystal structures on the PC subspace introduced in Chapter 2. In agreement with the structural analyses of our co-crystal structures, we found that all of the GSK180736A derivatives cluster in a small region of PC1, while the higher conformational flexibility of the kinase domain with the paroxetine derivatives allows those structures to have much higher variance along PC1. These insights have been essential to understanding how unique features of GRK2, such its more spacious hydrophobic subsite and ability to adjust its kinase domain conformation, determine its ability to selectively bind small molecule inhibitors with high potency.

Chapter 5: Design and Pharmacological Characterization of Covalent GRK5-Selective Inhibitors

Foreword

Ideas and conclusions presented in Chapter 5 are in preparation for publication. Also, some preliminary results were previously published in the dissertation for the degree of Doctor of Philosophy (Medicinal Chemistry) from the University of Michigan by Helen Waldschmidt (120). Helen Waldschmidt designed and synthesized the preliminary set of compounds (CCG258903, CCG258904, CCG262603, CCG264606, CCG263045, and CCG263115). Rachel Rowlands designed and synthesized the remainder of compounds presented in this study (CCG264099-265648). Rachel Rowlands generated the GRK5/GRK6 homology model, performed virtual screening, and performed intact and tandem mass spectrometry experiments. GRK5 and GRK5-C474S were provided by Renee Bouley, and GRK6 was provided by Kristoff Homan. I performed all pharmacological assays, time dependence experiments, and contributed analysis of structure-activity relationships.

5.1. Introduction

GRK2 and GRK5 are the predominantly expressed GRKs in normally functioning cardiomyocytes, and they aid in the signal regulation propagated by β ARs (48). In heart failure, both GRK2 and GRK5 expression levels are increased (53), which exacerbates the already poor responsiveness to circulating catecholamines by reducing the density of β ARs at the

cardiomyocyte membrane through GRK-mediated phosphorylation-dependent endocytosis (45). Although both GRK2 and GRK5 can phosphorylate β ARs, there is growing evidence that they have distinct roles in the normally functioning heart as well as in the progression of heart failure. For example, there is evidence that GRK2 upregulation in heart failure directly affects the density of β ARs available for signaling at the membrane, which in turn contributes to the pathological sympathetic overdrive in patients with heart failure (52, 98-99). GRK5 upregulation seems to primarily affect more long-term structural rearrangements in the heart by using its Ca^{2+} -calmodulin-dependent nuclear localization and transcriptional regulation to stimulate gene expression that drives maladaptive cardiac hypertrophy (60).

Although it has become clear that GRK2 and GRK5 do not have redundant β AR phosphorylation activities in the heart, the extent of their independent functions is not well-characterized. Selectively inhibiting GRK2 or GRK5 activity using highly selective chemical probes is one route to understanding their different roles in both the normally functioning heart and the progression of heart failure. In addition, GRK2- and GRK5-selective inhibitors have the exciting potential to be optimized for solubility and cell permeability for use as heart failure therapeutics. This selective inhibition could allow either GRK2- or GRK5-mediated pathologies to be specifically targeted in heart failure patients without compromising the entire β AR signaling pathway.

With 64% sequence similarity (46% identity) in the GRK2 and GRK5 kinase domains, targeting the conserved ATP-binding site is a significant challenge. Despite high structural similarity at the active site of all GRKs, we have previously had success in developing potent and selective GRK2 small molecule inhibitors that improve contractility in isolated adult mouse cardiomyocytes as discussed in Chapter 4, in part because GRK2 adopts a distinct inactive pose

from other GRK subfamilies (69, 100, 116-117). Comparison of GRK2 and GRK5 crystal structures revealed a more spacious ATP-binding pocket in GRK2 that was able to accommodate bulkier chemical substituents (92), thus allowing us to build out GRK5 binding. We have also developed a pan-GRK inhibitor (CCG-215022) with high nanomolar potency for both GRK2 and GRK5 (100), but so far we have not been successful in developing GRK5-selective binding inhibitors using a canonical reversible binding model. Thus, to selectively target GRK5 we have explored the use of irreversible covalent inhibitors. In particular, we utilized a reactive free thiol from a cysteine in the active site tether (AST) loop (Cys474 in GRK5) that is conserved in GRK4, 5, and 6, but is not found in the GRK1 or GRK2 subfamilies.

In recent years, the popularity of covalent warheads has risen within the pharmaceutical industry because they offer the possibility of both more potency and more selectivity than traditionally reversible inhibitors (121). In particular, specifically targeting non-conserved cysteines in the ATP-binding pocket of kinases has demonstrated utility (122–124). The most successful irreversible modifiers have come from modifying a reversibly binding compound with already low or sub- μ M affinity to contain a covalent warhead that is within reach and in the proper orientation to interact with the free thiol nucleophile of a nearby cysteine. The most widely used reaction to achieve irreversible covalent attachment onto a cysteine is the Michael addition, using electrophilic warheads such as acrylamides, vinyl sulfones, and alkynes (124). Examination of the crystal structure of GRK6 in what is believed to be a close to active configuration (PDB 3NYN) (37) revealed that the thiol from Cys474, located within the flexible AST-loop, is positioned adjacent to the ATP-binding site (**Figure 5.1A**). Furthermore, this cysteine is unique to GRK4-subfamily enzymes, and GRK2 lacks an analogous cysteine in its AST-loop (**Figure 5.1B**). We thus hypothesized that GRK5-Cys474 could be exploited as a

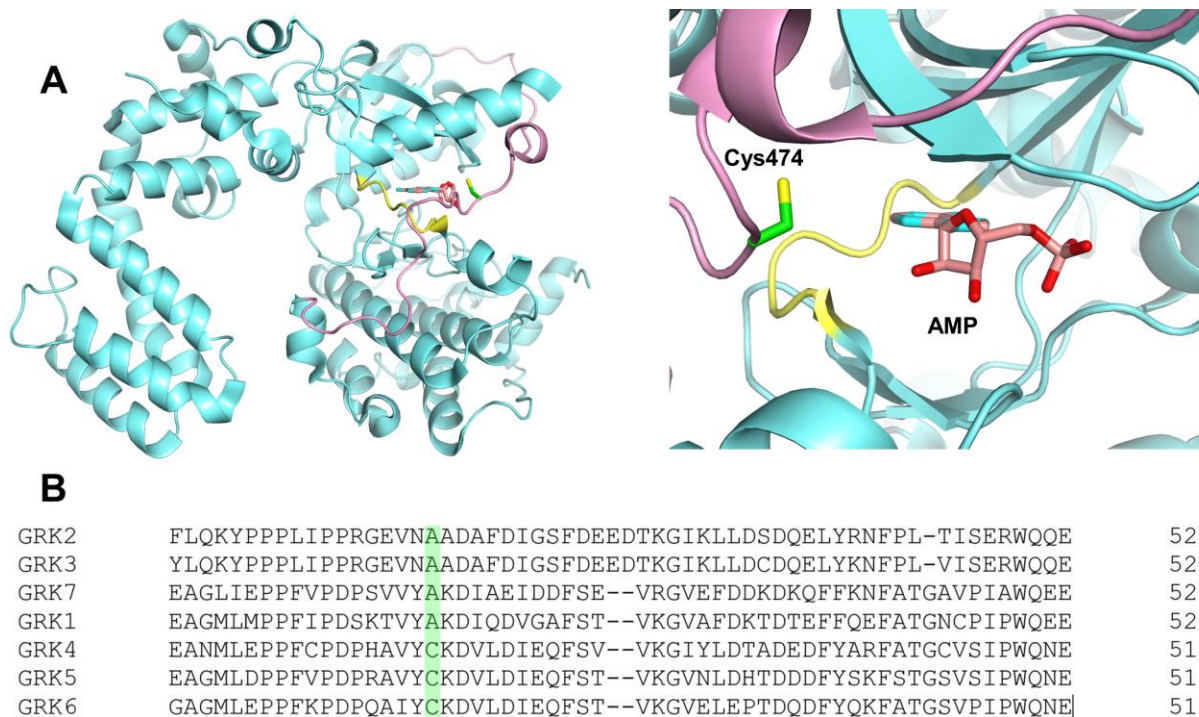


Figure 5.1. An AST-loop cysteine is conserved in the GRK4 subfamily. A) The high resolution crystal structure of GRK6-AMP (PDB 3NYO, aquamarine) (37) has a fully resolved AST-loop (light pink). Cys474 (green sticks) is in close proximity to the bound nucleotide, AMP (salmon sticks). The kinase domain hinge, which harbors important interaction sites with the adenine ring, is colored in yellow. B) The cysteine conserved in the GRK4 subfamily AST-loop is highlighted in this multiple sequence alignment of the seven human GRKs.

handle for covalent inhibition to gain selectivity for GRK5 over GRK2 and began designing a library of compounds guided by our previous SAR work and other available crystal structures.

Herein, we describe the development, pharmacological, and kinetic characterization of GRK5 inhibitors that gain their selectivity over GRK2 at least in part through covalent interaction with a cysteine in the AST-loop. We envision that these GRK5-selective inhibitors will be useful as molecular probes for understanding the different physiological roles of GRK2 and GRK5 in normally functioning cardiomyocytes and their pathological roles in the progression of heart failure. They will also serve as templates for future rounds of drug development targeting GRK5.

5.2. Materials and Methods

5.2.1. Homology Model and Virtual Screen

Crystal structures of GRK5·215022 (PDB 4WVK) (92) and GRK6·sangivamycin (PDB 4NYN) (37) were used to construct a full-length GRK5 homology model. A virtual screen using a constrained set of docking protocols including pharmacophore constraints, selected residues for compound engagement, and induced-fit active site flexibility was used to build a library of compounds enriched with inhibitors known to have activity towards GRK5.

5.2.2. Pharmacological Assays

IC₅₀s for human GRK5, bovine GRK6, and bovine GRK5-C474S were determined using the radiometric assay described in Chapter 4 and previously (100), with the exception that compounds were pre-incubated with GRKs for 4 h prior to initiation of the 8 min reactions by addition of 5 μ M ATP. GRK5 and GRK5-C474S were provided by Renee Bouley, and a palmitoylation-deficient variant of GRK6 was provided by previous Tesmer lab members.

For time dependence of inhibition, reactions containing 50 nM human GRK5 and 500 nM tubulin in Reaction Buffer (20 mM HEPES pH 7.5, 10 mM NaCl, 10 mM MgCl₂, 2 mM DTT), were initiated by simultaneously adding 100 μ M inhibitor in a final v/v of 10% DMSO and 5 μ M ATP supplemented with radioactive [γ -³²P]-ATP (PerkinElmer Life Sciences). Reactions were stopped at timepoints from 0 h to 6.5 h by quenching in SDS gel loading dye. Samples were separated on a 4-15% Criterion TGX precast gel (Bio-Rad), gels were exposed to a storage phosphor screen overnight and scanned using a Typhoon scanner, and bands corresponding to phosphorylated tubulin were quantified using ImageQuant software. Intensity of phosphorylated tubulin was plotted as a function of time and fit to the one-phase decay model to determine the

half-life and plateau value. All curve fitting and statistical analyses were performed in GraphPad Prism 7.03.

5.2.3. Intact and Tandem Mass Spectrometry

Intact and tandem mass spectrometry (MS) experiments were performed by Rachel Rowlands with assistance and consultation from the Proteomics Research Facility in the Department of Pathology at the University of Michigan Medical School.

5.3. Results

5.3.1. Design, Construction, and Structure-Activity Relationships of an Initial Library of Covalent Inhibitors

A high-throughput screen previously performed in the Tesmer lab identified GSK2163632A as a high potency GRK1 inhibitor ($IC_{50} = 130$ nM) with modest potency towards GRK5 ($IC_{50} = 3.2$ μ M). In addition, two related compounds GSK1713088A and GSK1326255A were shown to have similar potency for GRK5 ($IC_{50} = 3.2$ μ M and 2.5 μ M, respectively), and

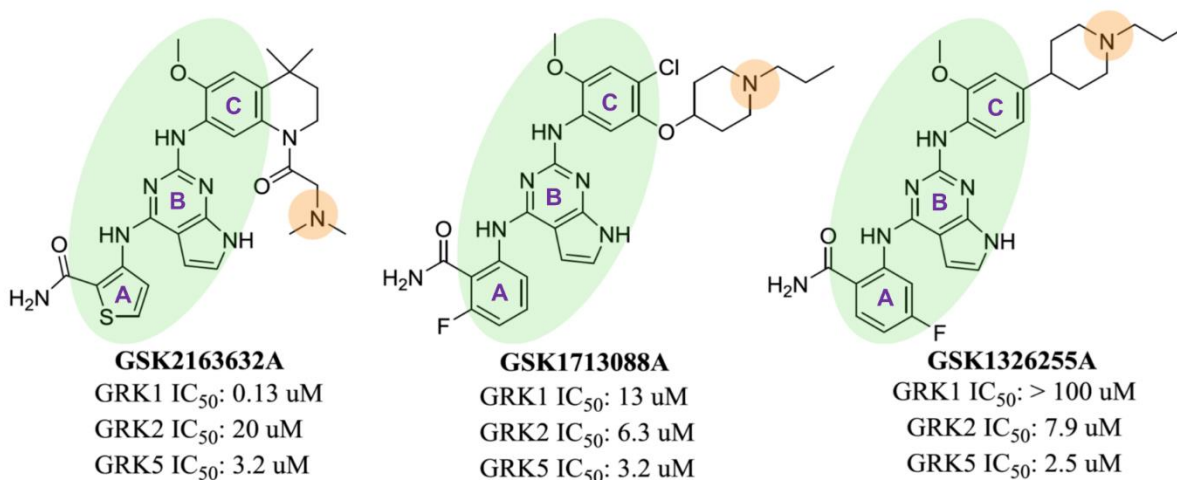


Figure 5.2^a. Lead compounds with modest GRK5 potency share a common pyrrolopyrimidine core. Three compounds identified from a high-throughput screen with modest GRK5 potency serve as starting models in the design of a hybrid scaffold molecule. A, B, and C rings are labeled. Chemically similar scaffold cores are indicated with green ellipses. Orange ellipses indicate the position predicted to be occupied by covalent modifiers in the library of pyrrolopyrimidine derivative compounds.
^a modified from (Waldschmidt 2017, Chapter 4)

modest selectivity over GRK1 and GRK2. All three compounds share a common pyrrolopyrimidine core. GSK2163632A contains a thiophene amide where both GSK1713088A and GSK1326255A contain a fluorophenyl amide. The three compounds become more structurally divergent on the opposite side of the pyrrolopyrimidine, although all three are linked to a methoxy-substituted aromatic ring (**Figure 5.2**).

GSK2163632A was later characterized in complex with GRK1 at 1.8 Å (4PNI) (104), showing the binding pose in the active site (**Figure 5.3**). In this complex, the three nitrogens from the pyrrolopyrimidine core form hydrogen bonds in a donor-acceptor-donor motif with the backbone carbonyl from Thr265 (Thr264 in GRK5) and the backbone nitrogen and carbonyl from Met267 (Met266 in GRK5). The thiophene amide packs under the P-loop, and the tetrahydroquinoline projects towards the AST-loop.

To build out selectivity for GRK1 and gain GRK5 selectivity, we envisioned that we could make a hybrid scaffold containing elements of these three lead molecules and optimize

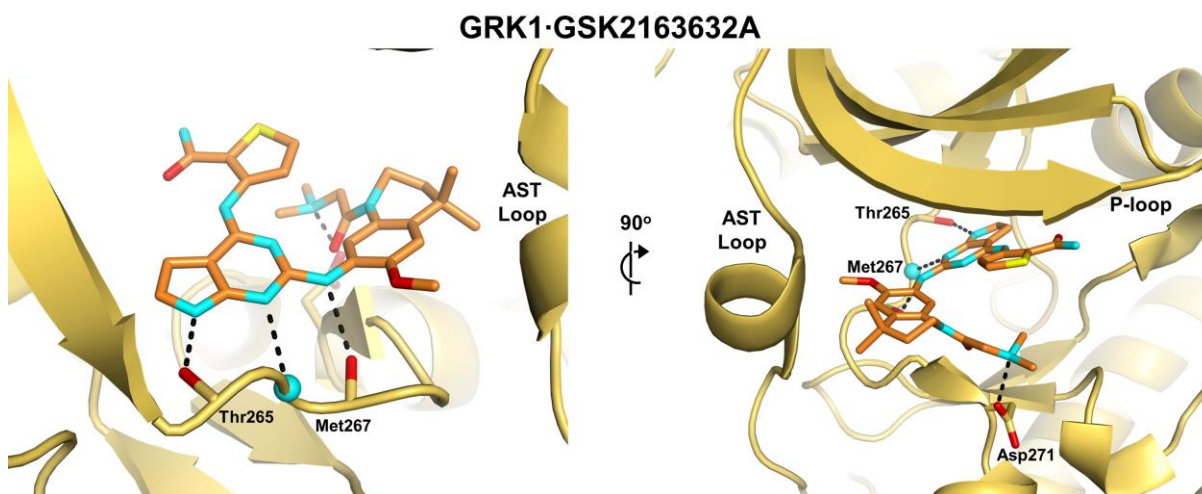


Figure 5.3. GRK1-GSK2163632A shows the pyrrolopyrimidine interactions with the hinge. In the co-crystal structure of GRK1-GSK2163632A (PDB 4PNI) (104), the pyrrolopyrimidine core forms an acceptor-donor-acceptor hydrogen bonding motif with backbone atoms in the kinase domain hinge (Thr265 carbonyl; Met267 backbone nitrogen and carbonyl). The thiophene ring packs under the P-loop, and the tetrahydroquinoline extends towards the AST-loop of GRK1. The terminal tertiary amine is stabilized by a salt bridge with Asp271.

GRK5 selectivity by appending additional substituents (120). Given that GRK5 has higher sequence similarity with the kinase domain of GRK1 (76%) than GRK2 (64%), we believed that we could use the GRK1-GSK2163632A structure to guide our design of selective GRK5 inhibitors. Also, in order to exploit interactions with the AST-loop, we created a homology model between GRK5 and GRK6, which has its AST-loop fully ordered (3NYN) (37). When the GRK5/GRK6 homology model was aligned with GRK1, we noticed a cysteine (Cys474 in GRK5) in the GRK6 AST-loop in close proximity to the tetrahydroquinoline of GSK2163632A (**Figure 5.4**). Sequence alignments show that this cysteine is uniquely conserved in the GRK4 subfamily (**Figure 5.1B**). Thus, we envisioned that we could gain GRK5 selectivity by designing inhibitors with the common pyrrolopyrimidine core that have covalent warheads predicted to engage with the free thiol of Cys474.

Because GSK1713088A and GSK1326255A have higher selectivity for GRK5 than GSK2163632A and both contain the fluorophenyl amide in the A ring position, we chose to

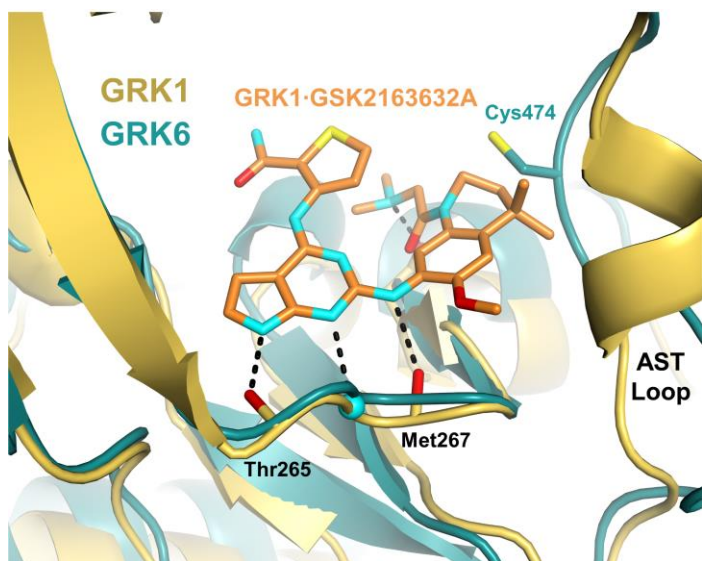


Figure 5.4. Cys474 is oriented towards the GSK2163632A tetrahydroquinoline. Alignment of GRK1 (PDB ID 4PNI, gold) (104) and GRK6 (from GRK5/GRK6 homology model, teal) shows the position of GRK6-Cys474 (teal sticks) relative to the GRK1-bound pyrrolopyrimidine (orange sticks).

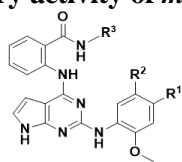
place a benzyl amide in the analogous position on our new scaffold. Because we were unsure about how the additional rings in the C ring position were contributing, we incorporated a 4-(aminomethyl)-2-methoxyaniline on the opposite side of the pyrrolopyrimidine ring and planned to append different amide-linked moieties to reach towards

Cys474. Our initial library of prototype covalent inhibitors included CCG258903 and CCG258904, which place an acrylamide *para* and *meta* to the aniline of the 4-aminomethyl-2-methoxyaniline, respectively, along with their unreactive fully saturated ethyl amide controls (CCG262604 and CCG262606). In addition, we explored a Boehringer Ingelheim (BI) covalent warhead in the *para* and *meta* positions (CCG263045 and CCG263115, respectively).

The BI *meta*- and *para*-substituted compounds had high potency for GRK1, 2, and 5, with higher potency for all in the *para* position, suggesting that this substituent packs favorably with all of the GRKs and is probably not gaining GRK5 potency through a covalent mechanism. The *meta* acrylamide (CCG258904) and *meta* ethyl amide (262606) both inhibited GRK5 with an IC₅₀ of 6 μ M, again suggesting that this compound does not gain its GRK5 potency through a covalent mechanism. Also, the acrylamide picked up modest potency for GRK2 (IC₅₀ = 39 μ M). We were interested to see that the *para* ethyl amide (CCG262603) had no inhibitory activity towards GRK1, 2, or 5, but the *para* acrylamide (CCG258903) had modest potency (IC₅₀ = 6 μ M) and selectivity for GRK5. In addition, it displayed evidence of time-dependent GRK5 inhibition over 60 min, which was our first indication that this inhibitor may be engaging GRK5 through a covalent mechanism.

5.3.2. Structure-Activity Relationships of Pyrrolopyrimidine Derivatives

Encouraged by the apparent covalent GRK5 inhibition by CCG258903, we then expanded upon this library of compounds. Using the same hybrid scaffold, we homologated the amide-linked covalent extensions to bring the covalent warhead closer to the predicted location of Cys474 in the GRK5 AST-loop. We tested four covalent modifiers of differing reactivity along with a fully saturated ethyl amide, placed in either the *meta* or *para* positions relative to

Table 5.1. Inhibitory activity of meta- and para-pyrrolopyrimidine derivatives

CCG	Compound	R ¹	R ²	R ³	IC ₅₀ (μM ± SD)				GRK5 Fold-Selectivity Over GRK2		
					GRK5			GRK2		GRK6	GRK5-C474S
					0 min	100 min	240 min				
258903	11		H	H		6.2 ± 4	>100	>100	ND	>16	
258904	12	H		H		5.5 ± 4	>100	39 ± 3	ND	>18	
264561	7a		H	CH ₃		>100	>100	>100	>100	NA	
264099	7b		H	CH ₃		78 ± 20	>100	>100	42 ± 40	>1.3	
264629	7c		H	CH ₃		17 ± 11	>100	>100	ND	>6	
265328	7d		H	CH ₃	>100	28.2 ± 21	1.1 ± 0.4	>100	1.8 ± 2	0.7 ± 0.5	>91
265327	7e		H	CH ₃		19 ± 20	>100	7.7 ± 6	ND	>5.2	
265041	7f	H		CH ₃		>100	2.9 ± 0.6	>100	ND	<0.03	
265042	7g	H		CH ₃		22 ± 5	3.2 ± 0.8	18 ± 8	ND	0.1	
265044	7h	H		CH ₃		4.8 ± 2	2.1 ± 2	2.6 ± 2	ND	0.4	
265268	7i	H		CH ₃		>100	>100	>100	ND	NA	
265267	7j	H		CH ₃		7.1 ± 3	>100	2.5 ± 3	ND	>14	

*All IC₅₀ values are the mean of *n* = 3 experiments. Errors shown represent the standard deviation. ND, IC₅₀ not determined. NA, GRK5 fold-selectivity not able to be calculated because both GRK2 and GRK5 IC₅₀ values are ambiguous (>100 μM).

the pyrrolopyrimidine core. Because our overall goal is to create GRK5-selective chemical probes that can be used to assess the different roles of GRK2 and GRK5 in the heart, we determined IC₅₀s for both GRK2 and GRK5. In addition, we determined IC₅₀s for GRK6 because it was used to generate the GRK5 homology model, with the expectation that we would see similarities in potency and selectivity for GRK5 and GRK6 given their high sequence similarity in the kinase domain. For our most potent and selective GRK5 compounds, we also tested whether we lost potency when Cys474 was mutated to serine. Although the free hydroxyl in serine can serve as a nucleophile in Michael addition reactions, the free thiol of cysteine is

expected to perform this chemistry much more efficiently. A decrease in GRK5-C474S potency relative to wild-type GRK5 would thus be in agreement with a covalent inhibition mechanism, although it is possible that similar affinities can be obtained even if covalent interactions are not formed.

Consistent with the SAR from our initial library of covalent inhibitors, the BI covalent modifier had high to moderate potency for GRK2, GRK5, and GRK6 in both the *meta* (CCG265044) and *para* (CCG264629) positions, with the exception that *para*-BI lost all potency for GRK2 (**Table 5.1**). These data suggest that this inhibitor is not working through a covalent mechanism, but rather is packing favorably with the kinase domain, except in the context of the *para* substitution with GRK2 (discussed further below). Based on docking into the GRK5/GRK6 homology model, it appears that this extension could pack between the AST-loop and P-loop, where the terminal amine could serve as a hydrogen bond acceptor for either a protein atom or the solvent. Both the *meta*-ethyl amide (CCG265041) and *meta* acrylamide (265042) inhibit GRK2 ($IC_{50} = 5 \mu M$ and $6 \mu M$, respectively), indicating that small lipophilic groups are tolerated in GRK2. Surprisingly, GRK2 lost potency for all of the compounds with *para*-substituted extensions, which is predicted to direct the covalent modifiers towards the AST-loop. It is possible that the slightly longer AST-loop in the GRK2 subfamily causes it to reach further down into the active site, as seen for residues 476-479 in the GRK2- $G\beta\gamma$ -GSK180736A co-crystal structure (4PNK) (104) which would collide with anything in the *para* position as it is modeled in this structure (**Figure 5.5**).

Examination of the *meta*-substituted position in GRK5 revealed that small polar groups, specifically those with hydrogen bond acceptors, are well tolerated. For example, both the *meta*

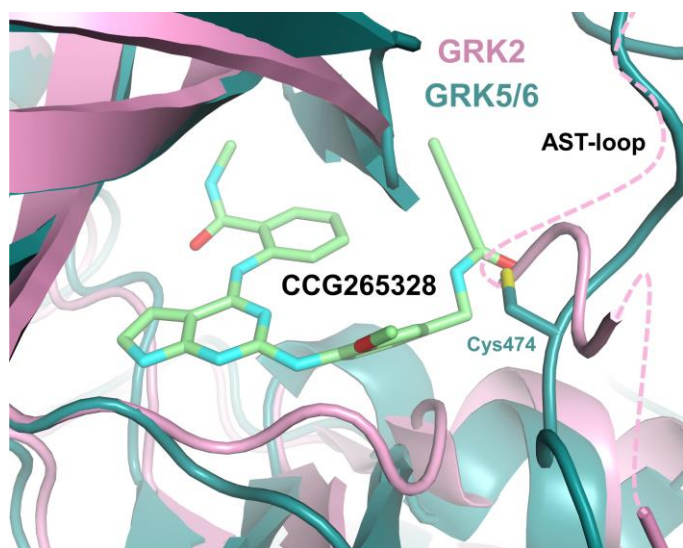


Figure 5.5. *Para* substituents may collide with the GRK2 AST-loop. Alignment of the GRK5/GRK6 homology model (teal) with GRK2 (PDB 4PNK, pink) (104) shows potential collisions of the covalent warhead (shown here is the *para*-alkyne in CCG265328) with the GRK2 AST-loop. Dashed lines represent the expected trajectory of the AST-loop, which is not well-resolved in the GRK2 electron density.

acrylamide (CCG265042) and *meta* vinyl sulfone (CCG265627) inhibit GRK5 and GRK6, but the polar vinyl sulfone is more potent ($IC_{50} = 6.23 \mu M$ for GRK5, $1.83 \mu M$ for GRK6) than the lipophilic acrylamide ($IC_{50} = 20 \mu M$ for GRK5, $18 \mu M$ for GRK6). Neither GRK5 nor GRK6 had any potency for the *meta* alkyne (CCG265268), suggesting that this more rigid covalent extension may collide with the P-loop or AST-loop,

or that it may simply be unfavorable to have a hydrocarbon chain extending towards the solvent.

The *para*-substituted compounds were the most selective for GRK5 over GRK2. As noted above, the BI compound (CCG264629) has modest potency ($IC_{50} = 14 \mu M$) for GRK5 and exhibited no inhibition of GRK2, but does not appear to be engaging GRK5 through a covalent mechanism because it is too distant from the Cys474 when it is docked into the GRK5/GRK6

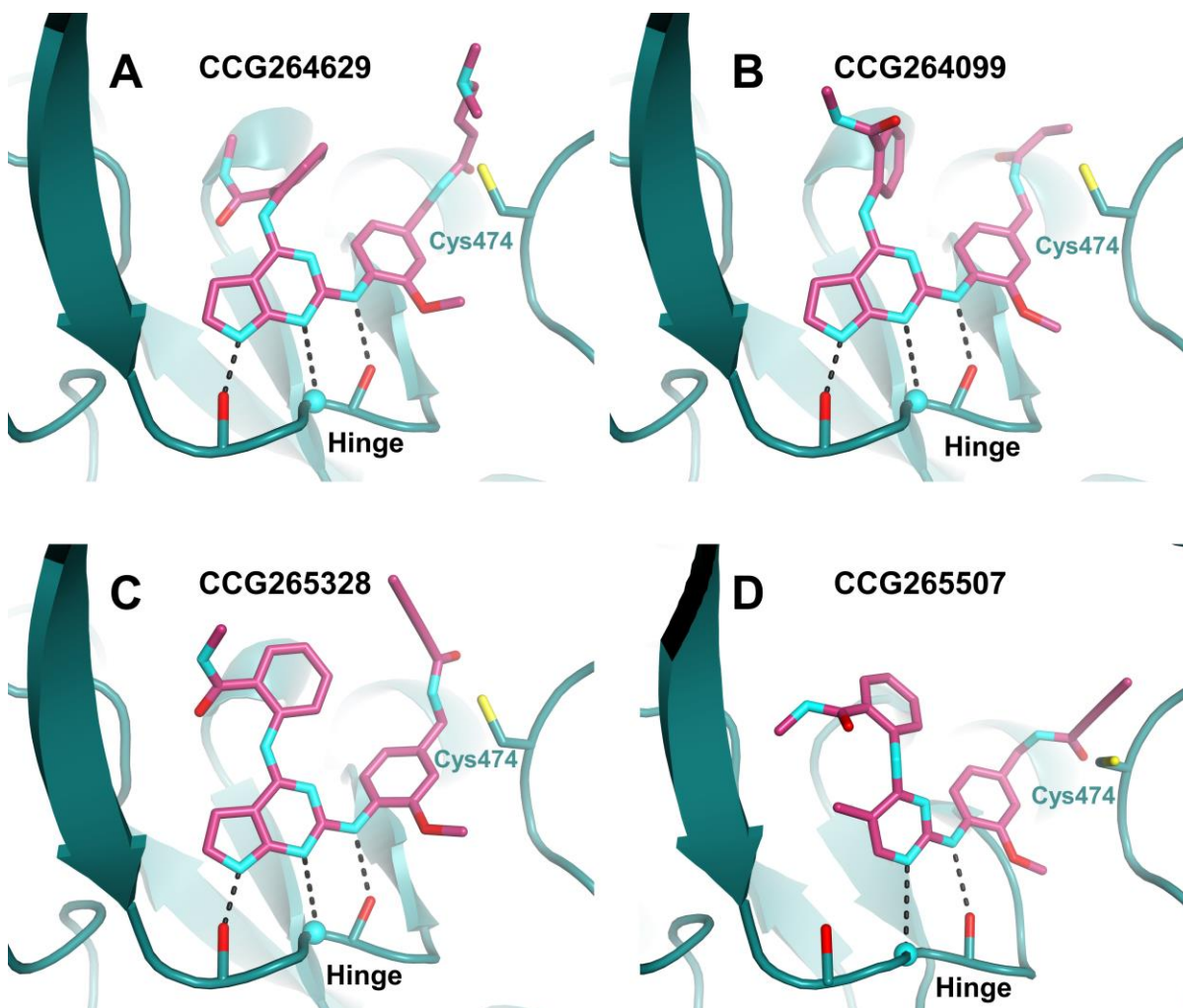
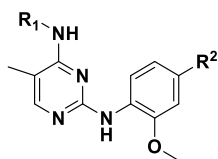


Figure 5.6. *Para*-substituted compounds docked into the GRK5/GRK6 homology model. Docking studies suggest that the pyrrolopyrimidine (A, B, C) or 5-methylpyrimidine (D) core forms the same hinge hydrogen bond pattern as seen in GRK1·GSK2163632A co-crystal structure. Electrophilic warheads extend towards Cys474 in the AST-loop. A) CCG264629, *para*-BI; B) CCG264099, *para*-acrylamide; C) CCG265328, *para*-alkyne. D) CCG265507, *para*-alkyne on the modified 5-methylpyrimidine scaffold.

homology model (**Figure 5.6A**). Consistent with the *meta* compounds, GRK5 tolerates the small substituents of the acrylamide (CCG264099, $IC_{50} = 90 \mu M$, **Figure 5.6B**) and vinyl sulfone (CCG265327, $IC_{50} = 57 \mu M$), although 5- to 10-fold less than when they are in the *meta* position, with a preference for the polar vinyl sulfone over the lipophilic acrylamide. We were surprised to find that the *para* alkyne (CCG265328) was our most potent and selective GRK5 inhibitor from this series ($IC_{50} = 1 \mu M$) because this same covalent modifier had no GRK5 activity in the *meta*

position. Our docking model places the alkyne group between the P-loop and AST-loop (**Figure 5.6C**). It is possible that the alkyne can actually be oriented more directly towards to AST-loop, not as it is seen in the docked homology model, given the rotational degrees of freedom around the benzene-methylene bond. These speculations could be resolved by a GRK5·CCG265328 co-crystal structure. Interestingly, CCG265328 also inhibits the GRK5-C474S mutant at 0.77 μM . The reason for this is unclear, but it is possible that the free hydroxyl of the engineered serine is able to achieve covalency given the high local concentration of CCG265328 in the active site, especially because the vector of interaction seems to be optimally aligned (see mass spectrometry results below). Alternatively, this particular compound could simply form a higher affinity reversible binding interaction than the other compounds tested.

Finally, we investigated modified scaffolds for our best compound, the *para*-substituted alkyne (CCG265328). We also placed the *para*-substituted acrylamide on these new scaffolds because, at the time of the compound synthesis, we believed we had evidence for covalent engagement by CCG264099 that we later determined was unjustified (**Table 5.2**). First, the benzyl amide (A ring) was replaced with 3-pyridine in an attempt to make a water-mediated hydrogen bond to the backbone of the P-loop. This substitution eliminated GRK5 inhibition, suggesting that hydrophobic rings are the most favorable for packing under the GRK5 P-loop at this position and the pyridine is not well tolerated. Next, the pyrrolopyrimidine was exchanged for a 5-methyl pyrimidine, causing a loss of one of the hydrogen bonds that are made by the protein with the pyrrolopyrimidine core as seen in the GRK1·GSK2163632A structure (**Figure 5.6D**). This scaffold modification combined with the *para* alkyne (CCG265507) led to slightly improved GRK5 potency ($\text{IC}_{50} = 0.77 \mu\text{M}$) over the original pyrrolopyrimidine scaffold

Table 5.2. Inhibitory activity of *para*-pyrimidine derivatives

CCG	R ¹	R ²	IC ₅₀ (μM ± SD)			GRK2	GRK6	GRK5 Fold-Selectivity Over GRK2
			GRK5					
			0 min	100 min	240 min			
265508					>100	>100	>100	NA
265507			5.1 ± 0.3	0.90 ± 0.03	0.85 ± 0.3	>100	0.75 ± 0.02	>117
265647					>100	>100	>100	NA
265648					57 ± 20	>100	>100	>1.8

*All IC₅₀ values are the mean of *n* = 3 experiments. Errors shown represent the standard deviation. ND, IC₅₀ not determined. NA, GRK5 fold-selectivity not able to be calculated because both GRK2 and GRK5 IC₅₀ values are ambiguous (>100 μM).

(CCG265328, GRK5 IC₅₀ = 1 μM), and we also observed a drastic reduction in potency of CCG265507 for the GRK5-C474S mutant (IC₅₀ = 30 μM).

5.3.3. Time-Dependent Inhibition for Lead Compounds

Although the predicted relative positions of Cys474 and the electrophilic warheads seen in our GRK5/GRK6 homology model combined with the GRK5/GRK6-selectivity over GRK2 seen in our SAR suggests that CCG265328 and CCG265507 are engaging GRK5 through a covalent mechanism, it is possible that these particular compounds have improved potency by a non-covalent mechanism. To begin to assess the possibility of a covalent interaction, we determined whether our two most promising lead compounds exhibited time-dependent inhibition for GRK5 (**Figure 5.7**). We determined IC₅₀s on GRK5 after either no pre-incubation, 100 min pre-incubation, or 240 min pre-incubation with compound (**Table 5.1**), with the expectation that there would be a leftward shift in the IC₅₀ over time if the compounds are forming a covalent interaction on this time scale. In addition, we tested a known GRK5 inhibitor

without a covalent modifier (CCG215022) at these time points as a negative control, with the expectation that there would be no significant change in IC_{50} over time.

As expected, CCG215022 did not demonstrate a significant change in IC_{50} between the 0, 100, and 240 min pre-incubations ($IC_{50} = 650$ nM, 710 nM, 910 nM, respectively; $p > 0.05$).

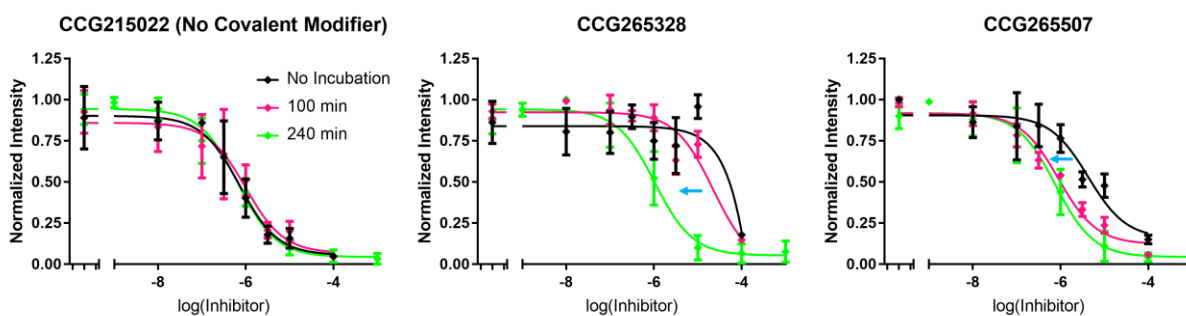


Figure 5.7. Time-dependent inhibition of CCG265328 and CCG265507. The expected leftward shift in IC_{50} for covalent compounds was demonstrated by both CCG265328 and CCG265507, while known non-covalent inhibitor CCG215022 shows no significant change in IC_{50} over time.

Without pre-incubation, CCG265328 showed an $IC_{50} > 100 \mu\text{M}$, with the hypothesized leftward shift to $22 \mu\text{M}$ after the 100 min pre-incubation and a further improvement in potency to $1.1 \mu\text{M}$ after 240 min. CCG265507 showed higher potency at 0 min ($IC_{50} = 4.3 \mu\text{M}$), with a 4.8- and 5.5-fold improvements in IC_{50} after 100 and 240 min pre-incubations (900 and 780 nM, respectively). The improvements in potency over time for both CCG265328 and CCG265507, while CCG215022 exhibited no change in potency, suggest that these two lead compounds are indeed inhibiting GRK5 through a covalent binding mechanism.

5.3.4. Intact and Tandem Mass Spectrometry on Top Compounds

To directly test whether CCG265328 and CCG265507 form covalent linkages to GRK5, specifically at Cys474 in the AST-loop, we performed intact and tandem mass spectrometry (MS). Intact MS results for CCG265328 and CCG265507 indicate a shift in the GRK5 protein peak by the mass corresponding to these two compounds. In addition, intact MS showed that a fraction of GRK5-C474S formed a covalent linkage with CCG265328 after overnight incubation

at 4 °C, in agreement with the 0.77 μ M IC₅₀. Tandem MS experiments with CCG265328 place the added mass on the peptide containing Cys474, although two other cysteines (Cys53 and Cys57, both of which are in the RH domain far from the ATP-binding pocket) show evidence for covalent engagement which we believe is a consequence of the high concentration of compound used in this study. These results provide strong support for a covalent binding model of inhibition for our two top compounds, CCG265328 and CCG265507, at Cys474.

5.4. Discussion

In this study, we developed a library of compounds designed to gain specificity for GRK5 over GRK2 through covalent attachment to the free thiol of a uniquely conserved cysteine in the AST-loop of the GRK4 subfamily (GRK5 Cys474). Specifically, a GRK5/GRK6 homology model was used to perform a virtual screen that identified compounds with modest selectivity for GRK5, and comparison to a previously determined GRK1 structural model was used to design a modified scaffold expected to enhance potency and selectivity for GRK5. Then, covalent extensions containing electrophilic Michael acceptor groups with variable softness and reactivities were appended to this modified scaffold at both the *para* and *meta* positions. Structure-activity relationships of our library of compounds identified the *para*-substituted alkyne as the best GRK5 inhibitor in terms of potency and selectivity over GRK2, leading us to explore additional modified scaffolds with the *para*-alkyne. These studies indicated two lead compounds with the most promising potency and GRK5-selectivity, CCG265328 and CCG265507. Time dependence of inhibition studies, intact MS, and tandem MS all provided evidence that both of these inhibitors form covalent attachment to Cys474, as we predicted and intended from our structural modeling. Excitingly, these are the first reported covalent GRK

inhibitors. We envision these compounds can be used as precursor molecules for further development of covalent inhibitors that may one day have therapeutic benefit for cardiac hypertrophy, and in the more immediate future as selective probes to investigate the GRK5-specific roles in the heart.

Chapter 6: Conclusions and Future Directions

GRKs are essential regulators of GPCR-mediated signal transduction pathways, and they are allosterically activated by interacting with active-state GPCRs. Despite being characterized in over 40 high resolution structural models with a variety of bound inhibitors and nucleotides, the structural determinants of GRK activation remain elusive. Mutational analyses, comparison to the transition state mimic of PKA, and the determination of the GRK6 crystal structure in a close to active conformation suggest that ordering of the GRK N-terminus and AST-loop are important for engaging GPCRs and stabilizing a catalytically competent conformation. In addition, regions on the surface of the kinase domain small lobe are believed to contribute to the GPCR docking site. The precise interactions at the GPCR-GRK interface and how they stabilize the active GRK conformation have not yet been characterized. Furthermore, with over 800 GPCRs and only seven human GRKs, the molecular determinants of GPCR specificity are poorly understood. To empirically determine the degree of conformational variability in the GRK kinase domain (KD), we performed a principal component analysis on all of the available GRK crystal structures. As expected, we saw that the majority of conformational flexibility is attributed to a clamshell-like opening and closing of the kinase domain around the ATP-binding site, and a twisting motion of the two kinase domain lobes accounted of a smaller amount of flexibility. When all of the protein kinase A (PKA) crystal structures were projected onto the principal component (PC) subspace defined by the GRKs, we observed a clear segregation between closed

(active) and open (inactive) PKA structures. Using PKA as a reference point for the degree of kinase domain closure, we saw that GRK4 subfamily crystal structures have come the closest to full kinase domain closure, but none of the GRKs become fully closed as seen in PKA. In addition, we observed that a large swing in the RH domain (RHD), which is structurally linked to the kinase domain, is associated with kinase domain opening and closing. This RHD-KD coupling led us to hypothesize that the RHD-KD interface is an intramolecular allosteric site. To test this hypothesis, we performed mutagenesis of both charged and hydrophobic residues at the RHD-KD interface and performed an *in silico* molecular dynamics analysis and *in vitro* steady-state kinetic analysis using the soluble substrate, tubulin. We observed small but significant effects on the phosphorylation of tubulin when either the charge was neutralized (eliminating a predicted salt-bridge) or the hydrophobicity was decreased. These results show that interactions at the intramolecular RHD-KD interface are important for stabilizing the kinase domain in a more active conformation. We suggest that disrupting this RHD-KD interface and increasing the frequency of KD closure is an intermediate GRK conformation that may be sampled along the pathway to full GPCR-mediated GRK activation.

A recent study suggests that GRK5 interacts directly with intracellular loop 3 (ICL3) of the β_2 -adrenergic receptor (β_2 AR). Structural alignment of GRK2 and 5 shows that a conserved patch of hydrophobic residues in GRK2 overlays with the predicted GPCR interaction site in GRK5. When we mutated these hydrophobic residues in GRK2 to polar residues and performed a steady-state kinetic analysis, we did not observe a significant effect on either tubulin or rhodopsin phosphorylation. These results suggest that the hydrophobicity of this solvent-exposed patch is not essential for GRK2 engagement with rhodopsin. The potential for a β_2 AR binding defect, especially given the much longer ICL3 in β_2 AR as compared to rhodopsin, remains to be

tested. Cells overexpressing β_2 AR have been grown and harvested and will be used as phosphorylation substrates for the GRK2 mutants in a future steady-state analysis. A β_2 AR phosphorylation defect by the GRK2 mutants would suggest that this hydrophobic patch may be an important determinant of GPCR specificity. If a lack of phenotype is observed with β_2 AR similar to what we observed for rhodopsin, different models will need to be considered. For example, this surface may be important for GPCR engagement in the GRK4 subfamily but may not play the analogous role in the GRK2 subfamily. A larger panel of GPCRs with variable ICL3s will need to be assessed to make any substantiated claims about the importance of this solvent-exposed hydrophobic patch in GRK2. In addition, the use of double or triple mutations, or more disruptive amino acid substitutions such as the incorporation of charged residues, may provide more clarity.

GRK-selective chemical probes are needed to assess the distinct roles of GRKs in different cell types and disease states. In addition, the therapeutic potential of inhibiting GRK2 or 5, or both, in heart failure has been demonstrated within the last decade. To advance through clinical trials, highly potent and selective inhibitors must be developed. Using a hybrid molecule approach, we developed highly potent and selective GRK2 inhibitors starting from either GSK180736A or paroxetine scaffolds. Our top compounds demonstrated improved contractility in adult mouse cardiomyocytes. Furthermore, co-crystallization with GRK2 and structural analysis of these compounds highlights the importance of the hinge binding moiety. While canonical hydrogen bond patterns observed when an indazole interacts with the hinge led to very low conformational flexibility among all the structures determined, the weaker hydrogen bond pattern seen with a benzodioxole hinge binding moiety coincided with a much greater degree of kinase domain flexibility. Analysis of the hinge binding moiety suggests that GRK2 may be able

to gain selectivity over the other GRKs and AGC kinases tested by having the unique innate ability to tolerate these weaker interactions at the hinge. Additional selectivity can be gained by exploiting the more spacious hydrophobic subsite found in GRK2.

To develop GRK5-selective inhibitors, we took advantage of a GRK4 subfamily-conserved cysteine in the AST-loop that is pointed towards the ATP-binding site. We used a common pyrrolopyrimidine scaffold with several electrophilic warhead groups appended either *meta* or *para* to the core and found that *para*-alkynes were the most potent and selective for GRK5. Mass spectrometry experiments confirmed that these compounds gained their GRK5 selectivity by forming covalent attachment. Our top GRK5-selective compound has a modest GRK5 IC₅₀ of 1 μ M, so additional improvements should be made improve the potency of this compound if it is to be used as a chemical probe. With SAR that indicates the utility of the pyrrolopyrimidine scaffold with a *para*-substituted alkyne, we are well equipped to perform compound optimizations. A GRK5-inhibitor co-crystal structure would provide more direct information, as we currently rely on a GRK5/GRK6 homology model with docked compounds for our SAR studies.

The studies herein have provided insight into regions on GRKs that may be important for GPCR engagement, an intramolecular allosteric site that we believe plays a role in stabilization of the active kinase conformation, and the subtle structural differences in the GRK ATP-binding sites that have been invaluable in the design of highly potent and selective GRK2 and 5 inhibitors. Without a high resolution structure of a GPCR-GRK complex, insight about GPCR engagement can only be provided by piecing together a number of independent studies. The highly dynamic nature of both GPCRs and GRKs has precluded the isolation of a stable GPCR-GRK complex that can be used for crystallization trials. The technological improvements and

increased access to cryo-electron microscopy in recent years makes this technique the most likely method for capturing a GPCR-GRK complex. The use of crosslinkers, nanobodies, and strong GPCR agonists will need to be explored before a homogeneous complex can be isolated and structurally characterized.

A high resolution GPCR-GRK structure would be instrumental in elucidating the molecular mechanism of GPCR-mediated allosteric activation of GRKs. Like GPCRs, which require both agonist and their intracellular binding partner to reach a stable, fully activated conformation, GRKs will likely only be stabilized in a fully activated conformation amenable for structural studies when bound to their GPCR substrate. Indeed, a fully activated GRK has not been observed despite over 40 deposited GRK structures in complex with a variety of inhibitor and nucleotide mimics. Many studies, including our analysis of the RH-KD allosteric interface presented in Chapter 2, suggest that a large swing in the RH domain away from the kinase domain occurs upon full GRK activation. Such a conformational change may be translated allosterically to enhanced kinase domain closure and activation, perhaps mediated by interactions between the $\alpha 10$ helix of the RH domain and the small lobe of the kinase domain. A high-resolution snapshot of an activated GPCR-GRK complex would provide clarity on the structural changes that must occur in order for GRKs to reach a fully activated state.

Other areas must also be explored to fully understand the how this interaction drives GPCR selectivity. With over 800 human GPCRs and only seven GRKs, it is likely that all GRKs contain a common GPCR docking site. Most evidence suggests that the GRK N-terminus interacts with the cytosolic site on GPCRs that is revealed upon agonist binding, and additional interactions with the negatively charged phospholipids help to stabilize this complex. By this model, GPCR engagement would be driven by the conserved interactions with the GRK N-

terminus, and GPCR selectivity could be gained through subtle structural differences on GRKs that change the chemical and structural complementarity with different GPCRs. A high-resolution GPCR-GRK complex will be needed to elucidate the precise interactions between the N-terminus and the GPCR. Determining the GRK surface that is buried by a GPCR interaction may reveal regions on both binding partners that are unique in different subtypes and thus may be used to confer selectivity. With a structural model in hand, more informed hypotheses about GPCR selectivity will be made that can be tested by mutagenesis and other *in vitro* methods. In addition, cell type-specific expression levels of both GPCRs and GRKs are likely important for GPCR selectivity. In the future, the expression profiles of GPCRs and GRKs for different cell types, in both healthy and disease states, and the resulting differences in GPCR phosphorylation profiles should be investigated to more fully understand the interplay between GRK expression and GPCR selectivity.

Importantly, a single GPCR-GRK structure will not answer the many questions that remain about this essential signaling complex. Rather, multiple GPCRs in multiple ligand-bound states will need to be characterized in complex with GRKs to more fully understand this interaction and, consequently, different mechanisms of signal transduction. For example, the structural differences between biased agonist-bound GPCRs may reveal subtle but distinct differences in the intracellular GPCR surface that are predicted to be bound preferentially by either arrestins or GRKs, leading the GPCR down either an arrestin-dependent intracellular signaling pathway or the canonical GRK-mediated desensitization pathway. Such structural information could be essential in developing biased agonist pharmaceuticals that elicit one desired activity without an undesirable side effect. *In silico* methods for predicting compound docking and protein dynamics in solution can also be useful for initial drug discovery screening,

but such methods require a high resolution structure or, preferably, multiple high resolution structures in different conformations. Expanding our knowledge of GPCR structures will likely be important for future drug discovery efforts, especially as modern pharmaceuticals are increasingly being designed to target highly specific pathologies with minimal side effects. Determining GPCR-GRK complexes in different ligand-bound states may reveal activated GPCR conformations that have not yet been characterized and may be exploited in future drug development efforts.

Finally, the role of aberrant GRK signaling in human disease and its ability to be inhibited by small molecules, as we have shown here, suggests that GRKs may have therapeutic potential beyond heart failure. For example, there is increasing evidence that GRKs are also involved in various aspects of cancer. As regulators of the canonical GPCR signaling pathways, as well as non-canonical signaling through receptor tyrosine kinases and other intracellular signaling proteins, GRKs are beginning to emerge as potential signaling hubs that can have a wide range of consequences if their careful regulation is compromised. For example, altered gene expression of GRKs has been found in different tumor types and associated with pro-survival phenotypes or increased cell migration, both of which are important for cancer pathology. Understanding how exactly GRKs contribute to the cross-talk between different signaling cascades is a daunting task because intracellular signal transduction pathways are highly complex, but it will have a large payoff if improved therapies for human disease can be developed.

References

1. Fredriksson, R., Lagerström, M. C., Lundin, L.-G., and Schiöth, H. B. (2003) The G-protein-coupled receptors in the human genome form five main families. Phylogenetic analysis, paralogon groups, and fingerprints. *Mol. Pharmacol.* **63**, 1256–72
2. Lagerström, M. C., and Schiöth, H. B. (2008) Structural diversity of G protein-coupled receptors and significance for drug discovery. *Nat. Rev. Drug Discov.* **7**, 339–357
3. Choe, H. W., Park, J. H., Kim, Y. J., and Ernst, O. P. (2011) Transmembrane signaling by GPCRs: Insight from rhodopsin and opsin structures. *Neuropharmacology.* **60**, 52–57
4. Katritch, V., Cherezov, V., and Stevens, R. C. (2013) Structure-function of the G protein-coupled receptor superfamily. *Annu Rev Pharmacol Toxicol.* **53**, 531–556
5. Katritch, V., Cherezov, V., and Stevens, R. C. (2012) Diversity and modularity of G protein-coupled receptor structures. *Trends Pharmacol. Sci.* **33**, 17–27
6. Flock, T., Ravarani, C. N. J., Sun, D., Venkatakrishnan, A. J., Kayikci, M., Tate, C. G., Veprintsev, D. B., and Babu, M. M. (2015) Universal allosteric mechanism for G α activation by GPCRs. *Nature.* **524**, 173–179
7. Gilman, A. G. (1987) G proteins: transducers of receptor-generated signals. *Annu. Rev. Biochem.* **56**, 615–649
8. Neer, E. J. (1995) Heterotrimeric G proteins: organizers of transmembrane signals. *Cell.* **80**, 249–257
9. Park, P. S.-H., Lodowski, D. T., and Palczewski, K. (2008) Activation of G Protein–Coupled Receptors: Beyond Two-State Models and Tertiary Conformational Changes. *Annu. Rev. Pharmacol. Toxicol.* **48**, 107–141
10. Huber, T., Menon, S., and Sakmar, T. P. (2008) Structural Basis for Ligand Binding and Specificity in Adrenergic Receptors : Implications for GPCR-Targeted Drug Discovery. *October*
11. Bouvier, M. (2013) Unraveling the structural basis of GPCR activation and inactivation. *Nat. Struct. Mol. Biol.* **20**, 539–541
12. Manglik, A., and Kobilka, B. (2014) The role of protein dynamics in GPCR function: Insights from the Beta2AR and rhodopsin. *Curr. Opin. Cell Biol.* **27**, 136–143
13. Park, J. H., Scheerer, P., Hofmann, K. P., Choe, H.-W., and Ernst, O. P. (2008) Crystal structure of the ligand-free G-protein-coupled receptor opsin. *Nature.* **454**, 183–187
14. Scheerer, P., Park, J. H., Hildebrand, P. W., Kim, Y. J., Krauss, N., Choe, H. W., Hofmann, K. P., and Ernst, O. P. (2008) Crystal structure of opsin in its G-protein-interacting conformation. *Nature.* **455**, 497–502
15. Choe, H.-W., Kim, Y. J., Park, J. H., Morizumi, T., Pai, E. F., Krauß, N., Hofmann, K. P., Scheerer, P., and Ernst, O. P. (2011) Crystal structure of *metarhodopsin II*. *Nature.* **471**, 651–655

16. Rasmussen, S. G. F., Choi, H.-J., Fung, J. J., Pardon, E., Casarosa, P., Chae, P. S., DeVree, B. T., Rosenbaum, D. M., Thian, F. S., Kobilka, T. S., Schnapp, A., Konetzki, I., Sunahara, R. K., Gellman, S. H., Pautsch, A., Steyaert, J., Weis, W. I., and Kobilka, B. K. (2011) Structure of a nanobody-stabilized active state of the $\beta 2$ adrenoceptor. *Nature*. **469**, 175–180
17. Rasmussen, S. G. F., DeVree, B. T., Zou, Y., Kruse, A. C., Chung, K. Y., Kobilka, T. S., Thian, F. S., Chae, P. S., Pardon, E., Calinski, D., Mathiesen, J. M., Shah, S. T. A., Lyons, J. A., Caffrey, M., Gellman, S. H., Steyaert, J., Skiniotis, G., Weis, W. I., Sunahara, R. K., and Kobilka, B. K. (2011) Crystal structure of the $\beta 2$ adrenergic receptor-Gs protein complex. *Nature*. **477**, 549–55
18. Wheatley, M., Wootten, D., Conner, M. T., Simms, J., Kendrick, R., Logan, R. T., Poyner, D. R., and Barwell, J. (2012) Lifting the lid on GPCRs: The role of extracellular loops. *Br. J. Pharmacol.* **165**, 1688–1703
19. Pitcher, J. A., Freedman, N. J., and Lefkowitz, R. J. (1998) G Protein-Coupled Receptor Kinases. *Annu. Rev. Biochem.* **67**, 653–692
20. Huang, C. C., and Tesmer, J. J. G. (2011) Recognition in the face of diversity: Interactions of heterotrimeric G proteins and G protein-coupled receptor (GPCR) kinases with activated GPCRs. *J. Biol. Chem.* **286**, 7715–7721
21. Gurevich, E. V., Tesmer, J. J. G., Mushegian, A., and Gurevich, V. V. (2012) G protein-coupled receptor kinases: More than just kinases and not only for GPCRs. *Pharmacol. Ther.* **133**, 40–69
22. Ferguson, S. S. G. (2001) Evolving concepts in G protein-coupled receptor endocytosis: the role in receptor desensitization and signaling. *Pharmacol. Rev.* **53**, 1–24
23. Hanyaloglu, A. C., and Zastrow, M. von (2008) Regulation of GPCRs by Endocytic Membrane Trafficking and Its Potential Implications. *Annu. Rev. Pharmacol. Toxicol.* **48**, 537–568
24. Lefkowitz, R. J., and Carolina, N. (1993) G Protein-Coupled Receptor Kinases Minireview. *Cell*. **74**, 409–412
25. Homan, K. T., and Tesmer, J. J. G. (2014) Structural insights into G protein-coupled receptor kinase function. *Curr. Opin. Cell Biol.* **27**, 25–31
26. Onorato, J. J., Gillis, M. E., Liu, Y., Benovic, J. L., and Ruoho, A. E. (1995) The beta-adrenergic receptor kinase (GRK2) is regulated by phospholipids. *J. Biol. Chem.* **270**, 21346–53
27. DebBurman, S. K., Ptasienski, J., Boetticher, E., Lomasney, J. W., Benovic, J. L., and Hosey, M. M. (1995) Lipid-mediated regulation of G protein-coupled receptor kinases 2 and 3. *J. Biol. Chem.* **270**, 5742–7
28. DebBurman, S. K., Ptasienski, J., Benovic, J. L., and Hosey, M. M. (1996) G protein-coupled receptor kinase GRK2 is a phospholipid-dependent enzyme that can be conditionally activated by G protein beta-gamma subunits. *J. Biol. Chem.* **271**, 22552–22562
29. Carman, C. V., Barak, L. S., Chen, C., Liu-Chen, L. Y., Onorato, J. J., Kennedy, S. P., Caron, M. G., and Benovic, J. L. (2000) Mutational analysis of Gbetagamma and phospholipid interaction with G protein-coupled receptor kinase 2. *J. Biol. Chem.* **275**, 10443–52
30. Homan, K. T., Glukhova, A., and Tesmer, J. J. G. (2013) Regulation of G Protein-Coupled Receptor Kinases by Phospholipids. *Curr. Med. Chem.* **20**, 39–46

31. Willets, J. M., Challiss, R. A. J., and Nahorski, S. R. (2003) Non-visual GRKs: Are we seeing the whole picture? *Trends Pharmacol. Sci.* **24**, 626–633
32. Pearce, L. R., Komander, D., and Alessi, D. R. (2010) The nuts and bolts of AGC protein kinases. *Nat. Rev. Mol. Cell Biol.* **11**, 9–22
33. Hanks, S. K., and Hunter, T. (1995) Protein kinases 6. The eukaryotic protein kinase superfamily: kinase (catalytic) domain structure and classification. *Faseb J.* **9**, 576–596
34. Kannan, N., Haste, N., Taylor, S. S., and Neuwald, A. F. (2007) The hallmark of AGC kinase functional divergence is its C-terminal tail, a cis-acting regulatory module. *Proc. Natl. Acad. Sci.* **104**, 1272–1277
35. Arencibia, J. M., Pastor-Flores, D., Bauer, A. F., Schulze, J. O., and Biondi, R. M. (2013) AGC protein kinases: from structural mechanism of regulation to allosteric drug development for the treatment of human diseases. *Biochim. Biophys. Acta.* **1834**, 1302–21
36. Madhusudan, Akamine, P., Xuong, N.-H., and Taylor, S. S. (2002) Crystal structure of a transition state mimic of the catalytic subunit of cAMP-dependent protein kinase. *Nat. Struct. Biol.* **9**, 273–277
37. Boguth, C. a, Singh, P., Huang, C., and Tesmer, J. J. G. (2010) Molecular basis for activation of G protein-coupled receptor kinases. *EMBO J.* **29**, 3249–3259
38. Tesmer, J. J. G. (2009) *Structure and Function of Regulator of G Protein Signaling Homology Domains*, 1st Ed., Elsevier Inc., 10.1016/S1877-1173(09)86004-3
39. Carman, C. V, Parent, J., Day, P. W., Pronin, A. N., Sternweis, P. M., Wedegaertner, P. B., Gilman, A. G., Benovic, J. L., and Kozasa, T. (1999) Selective Regulation of Gq/11 by an RGS Domain in the G Protein-coupled Receptor Kinase, GRK2. *J. Biol. Chem.* **274**, 34483–34492
40. Tesmer, V. M., Kawano, T., Shankaranarayanan, A., Kozasa, T., and Tesmer, J. J. G. (2005) Snapshot of Activated G Proteins at the Membrane: The G q-GRK2-G Complex. *Science (80-.).* **310**, 1686–1690
41. Lodowski, D., Pitcher, J., Capel, W., Lefkowitz, R., and Tesmer, J. (2003) Keeping G proteins at bay: A complex between G protein-coupled receptor kinase 2 and G beta gamma. *Science (80-.).* **300**, 1256–1263
42. Ribas, C., Penela, P., Murga, C., Salcedo, A., García-Hoz, C., Jurado-Pueyo, M., Aymerich, I., and Mayor, F. (2007) The G protein-coupled receptor kinase (GRK) interactome: role of GRKs in GPCR regulation and signaling. *Biochim. Biophys. Acta.* **1768**, 913–22
43. Port, J. D., and Bristow, M. R. (2001) Altered beta-adrenergic receptor gene regulation and signaling in chronic heart failure. *J. Mol. Cell. Cardiol.* **33**, 887–905
44. Rockman, H. a, Koch, W. J., and Lefkowitz, R. J. (2002) Seven-transmembrane-spanning receptors and heart function. *Nature.* **415**, 206–212
45. Lohse, M. J., Engelhardt, S., and Eschenhagen, T. (2003) What Is the Role of beta-Adrenergic Signaling in Heart Failure? *Circ. Res.* **93**, 896–906
46. Tilley, D. G. (2011) G protein-dependent and G protein-independent signaling pathways and their impact on cardiac function. *Circ. Res.* **109**, 217–230
47. Penela, P., Murga, C., Ribas, C., Tutor, A. S., Peregrin, S., and Mayor, F. (2006) Mechanisms of regulation of G protein-coupled receptor kinases (GRKs) and cardiovascular disease. *Cardiovasc. Res.* **69**, 46–56
48. Huang, Z. M., Gold, J. I., and Koch, W. J. (2011) G protein-coupled receptor kinases in normal and failing myocardium. *Front. Biosci.* **16**, 3057–3060

49. Cannavo, A., Liccardo, D., and Koch, W. J. (2013) Targeting cardiac beta-adrenergic signaling via GRK2 inhibition for heart failure therapy. *Front. Physiol.* **4** SEP, 1–7
50. Hullmann, J., Traynham, C. J., Coleman, R. C., and Koch, W. J. (2016) The expanding GRK interactome: Implications in cardiovascular disease and potential for therapeutic development. *Pharmacol. Res.* **110**, 52–64
51. Kemp, C. D., and Conte, J. V (2012) The pathophysiology of heart failure. *Cardiovasc. Pathol.* **21**, 365–371
52. Triposkiadis, F., Karayannis, G., Giamouzis, G., Skoularigis, J., Louridas, G., and Butler, J. (2009) The Sympathetic Nervous System in Heart Failure. *J. Am. Coll. Cardiol.* **54**, 1747–1762
53. Ungerer, M., Bohm, M., Elce, J. S., Erdmann, E., and Lohse, M. J. (1993) Altered expression of beta-adrenergic receptor kinase and beta1-adrenergic receptors in the failing human heart. *Circulation.* **87**, 454–463
54. Lymperopoulos, A., Rengo, G., and J. Koch, W. (2012) GRK2 Inhibition in Heart Failure: Something Old, Something New. *Curr. Pharm. Des.* **18**, 186–191
55. Raake, P. W., Vinge, L. E., Gao, E., Boucher, M., Rengo, G., Chen, X., Degeorge, B. R., Matkovich, S., Houser, S. R., Most, P., Eckhart, A. D., Dorn, G. W., and Koch, W. J. (2008) G protein-coupled receptor kinase 2 ablation in cardiac myocytes before or after myocardial infarction prevents heart failure. *Circ. Res.* **103**, 413–422
56. Rockman, H. a, Chien, K. R., Choi, D. J., Iaccarino, G., Hunter, J. J., Ross, J., Lefkowitz, R. J., and Koch, W. J. (1998) Expression of a beta-adrenergic receptor kinase 1 inhibitor prevents the development of myocardial failure in gene-targeted mice. *Proc. Natl. Acad. Sci. U. S. A.* **95**, 7000–7005
57. Eckhart, A. D., Ozaki, T., Tevaearai, H., Rockman, H. a, and Koch, W. J. (2002) Vascular-targeted overexpression of G protein-coupled receptor kinase-2 in transgenic mice attenuates beta-adrenergic receptor signaling and increases resting blood pressure. *Mol. Pharmacol.* **61**, 749–758
58. Thal, D. M., Homan, K. T., Chen, J., Wu, E. K., Hinkle, P. M., Huang, Z. M., Chuprun, J. K., Song, J., Gao, E., Cheung, J. Y., Sklar, L. A., Koch, W. J., and Tesmer, J. J. G. (2012) Paroxetine Is a Direct Inhibitor of G Protein-Coupled Receptor Kinase 2 and Increases Myocardial Contractility. *ACS Chem. Biol.* **7**, 1830–1839
59. Schumacher, S. M., Gao, E., Zhu, W., Chen, X., Chuprun, J. K., Feldman, A. M., Tesmer, J. J. G., and Koch, W. J. (2015) Paroxetine-mediated GRK2 inhibition reverses cardiac dysfunction and remodeling after myocardial infarction. *Sci. Transl. Med.* **7**, 1–12
60. Traynham, C. J., Hullmann, J., and Koch, W. J. (2016) Canonical and non-canonical actions of GRK5 in the heart. *J. Mol. Cell. Cardiol.* **92**, 196–202
61. Gold, J. I., Gao, E., Shang, X., Premont, R. T., and Koch, W. J. (2012) Determining the absolute requirement of G protein-coupled receptor kinase 5 for pathological cardiac hypertrophy. *Circ. Res.* **111**, 1048–1053
62. Kohout, T. a, and Lefkowitz, R. J. (2003) Regulation of G protein-coupled receptor kinases and arrestins during receptor desensitization. *Mol. Pharmacol.* **63**, 9–18
63. Huang, C. C., Yoshino-Koh, K., and Tesmer, J. J. G. (2009) A surface of the kinase domain critical for the allosteric activation of G protein-coupled receptor kinases. *J. Biol. Chem.* **284**, 17206–17215

64. Pao, C. S., Barker, B. L., and Benovic, J. L. (2009) Role of the amino terminus of G protein-coupled receptor kinase 2 in receptor phosphorylation. *Biochemistry*. **48**, 7325–7333
65. Sterne-Marr, R., Leahey, P. A., Bresee, J. E., Dickson, H. M., Ho, W., Ragusa, M. J., Donnelly, R. M., Amie, S. M., Krywy, J. a., Brookins-Danz, E. D., Orakwue, S. C., Carr, M. J., Yoshino-Koh, K., Li, Q., and Tesmer, J. J. G. (2009) GRK2 activation by receptors: Role of the kinase large lobe and carboxyl-terminal tail. *Biochemistry*. **48**, 4285–4293
66. Huang, C.-C., Orban, T., Jastrzebska, B., Palczewski, K., and Tesmer, J. J. G. (2011) Activation of G protein-coupled receptor kinase 1 involves interactions between its N-terminal region and its kinase domain. *Biochemistry*. **50**, 1940–9
67. Orban, T., Huang, C. C., Homan, K. T., Jastrzebska, B., Tesmer, J. J., and Palczewski, K. (2012) Substrate-induced changes in the dynamics of rhodopsin kinase (G protein-coupled receptor kinase 1). *Biochemistry*. **51**, 3404–3411
68. Komolov, K. E., Bhardwaj, A., and Benovic, J. L. (2015) Atomic structure of GRK5 reveals distinct structural features novel for G protein-coupled receptor kinases. *J. Biol. Chem.* **290**, 20629–20647
69. Yao, X.-Q., Cato, M. C., Labudde, E., Beyett, T. S., Tesmer, J. J. G., and Grant, B. J. (2017) Navigating the conformational landscape of G protein-coupled receptor kinases during allosteric activation. *J. Biol. Chem.* **292**, 16032–16043
70. Knighton, D. R., Zheng, J. H., Ten Eyck, L. F., Ashford, V. A., Xuong, N.-H., Taylor, S. S., and Sowadski, J. M. (1991) Crystal structure of the catalytic subunit of cyclic adenosine monophosphate-dependent protein kinase. *Science (80-.)*. **253**, 407–414
71. Narayana, N., Cox, S., Nguyen-huu, X., Ten Eyck, L. F., and Taylor, S. S. (1997) A binary complex of the catalytic subunit of cAMP-dependent protein kinase and adenosine further defines conformational flexibility. *Structure*. **5**, 921–35
72. Parsons, S. J., and Parsons, J. T. (2004) Src family kinases, key regulators of signal transduction. *Oncogene*. **23**, 7906–7909
73. Komolov, K. E., Du, Y., Duc, N. M., Betz, R. M., Rodrigues, J. P. G. L. M., Leib, R. D., Patra, D., Skiniotis, G., Adams, C. M., Dror, R. O., Chung, K. Y., Kobilka, B. K., and Benovic, J. L. (2017) Structural and Functional Analysis of a β 2-Adrenergic Receptor Complex with GRK5. *Cell*. **169**, 407–421.e16
74. Huang, C. -c., and Tesmer, J. J. G. (2011) Recognition in the Face of Diversity: Interactions of Heterotrimeric G proteins and G Protein-coupled Receptor (GPCR) Kinases with Activated GPCRs. *J. Biol. Chem.* **286**, 7715–7721
75. He, Y., Gao, X., Goswami, D., Hou, L., Pal, K., Yin, Y., Zhao, G., Ernst, O. P., Griffin, P., Melcher, K., and Xu, H. E. (2017) Molecular assembly of rhodopsin with G protein-coupled receptor kinases. *Cell Res.* **27**, 728–747
76. Ritter, S. L., and Hall, R. A. (2009) Fine-tuning of GPCR activity by receptor-interacting proteins. *Nat. Rev. Mol. Cell Biol.* **10**, 819–830
77. Moore, C. A. C., Milano, S. K., and Benovic, J. L. (2007) Regulation of Receptor Trafficking by GRKs and Arrestins. *Annu. Rev. Physiol.* **69**, 451–482
78. Lefkowitz, R. J., Wessels, M. R., and Stadel, J. M. (1980) Hormones, Receptors, and Cyclic AMP: Their Role in Target Cell Refractoriness. *Curr. Top. Cell. Regul.* **17**, 205–230
79. Hausdorff, W. P., Caron, M. G., and Lefkowitz, R. J. (1990) Turning off the signal: desensitization of beta-adrenergic receptor function. *FASEB J.* **4**, 2881–2889

80. Chen, C. Y., Dion, S. B., Kim, C. M., and Benovic, J. L. (1993) Beta-adrenergic receptor kinase. Agonist-dependent receptor binding promotes kinase activation. *J. Biol. Chem.* **268**, 7825–31
81. Kohout, T. A., and Lefkowitz, R. J. (2003) Regulation of G Protein-Coupled Receptor Kinases and Arrestins During Receptor Desensitization. *Mol. Pharmacol.* **63**, 9–18
82. Premont, R. T., and Gainetdinov, R. R. (2007) Physiological Roles of G Protein-Coupled Receptor Kinases and Arrestins. *Annu. Rev. Physiol.* **69**, 511–34
83. Kuhn, H., and Dreyer, W. J. (1972) Light Dependent Phosphorylation of Rhodopsin by ATP. *FEBS Lett.* **20**, 1–6
84. Wilden, U., and Kühn, H. (1982) Light-dependent phosphorylation of rhodopsin: number of phosphorylation sites. *Biochemistry.* **21**, 3014–3022
85. Pei, G., Samama, P., Lohse, M., Wang, M., Codina, J., and Lefkowitz, R. J. (1994) A constitutively active mutant beta2-adrenergic receptor is constitutively desensitized and phosphorylated. *Proc. Natl. Acad. Sci. U. S. A.* **91**, 2699–2702
86. Benovic, J. L., Bouvier, M., Caron, M. G., and Lefkowitz, R. J. (1988) Regulation of Adenylyl Cyclase-Coupled beta-Adrenergic Receptors. *Annu. Rev. Cell Biol.* **4**, 405–428
87. Palczewski, K., Buczyłko, J., Kaplan, M. W., Polans, A. S., and Crabb, J. W. (1991) Mechanism of rhodopsin kinase activation. *J. Biol. Chem.* **266**, 12949–55
88. McCarthy, N. E. M., and Akhtar, M. (2002) Activation of rhodopsin kinase. *Biochem. J.* **363**, 359–64
89. Lodowski, D. T., Tesmer, V. M., Benovic, J. L., and Tesmer, J. J. G. (2006) The structure of G protein-coupled receptor kinase (GRK)-6 defines a second lineage of GRKs. *J. Biol. Chem.* **281**, 16785–16793
90. Singh, P., Wang, B., Maeda, T., Palczewski, K., and Tesmer, J. J. G. (2008) Structures of Rhodopsin Kinase in Different Ligand States Reveal Key Elements Involved in G Protein-coupled Receptor Kinase Activation. *J. Biol. Chem.* **283**, 14053–62
91. Allen, S. J., Parthasarathy, G., Darke, P. L., Diehl, R. E., Ford, R. E., Hall, D. L., Johnson, S. a., Reid, J. C., Rickert, K. W., Shipman, J. M., Soisson, S. M., Zuck, P., Munshi, S. K., and Lumb, K. J. (2015) Structure and Function of the Hypertension Variant A486V of G Protein-coupled Receptor Kinase 4. *J. Biol. Chem.* **290**, 20360–20373
92. Homan, K. T., Waldschmidt, H. V., Glukhova, A., Cannavo, A., Song, J., Cheung, J. Y., Koch, W. J., Larsen, S. D., and Tesmer, J. J. G. (2015) Crystal Structure of G Protein-Coupled Receptor Kinase 5 in Complex with a Rationally Designed Inhibitor. *J. Biol. Chem.* **290**, 20649–20659
93. Watari, K., Nakaya, M., and Kurose, H. (2014) Multiple functions of G protein-coupled receptor kinases. *J. Mol. Signal.* **9**, 1
94. Touhara, K., Koch, W. J., Hawes, B. E., and Lefkowitz, R. J. (1995) Mutational Analysis of the Pleckstrin Homology Domain of the beta-Adrenergic Receptor Kinase. *J. Biol. Chem.* **270**, 17000–17005
95. Beautrait, A., Michalski, K. R., Lopez, T. S., Mannix, K. M., McDonald, D. J., Cutter, A. R., Medina, C. B., Hebert, A. M., Francis, C. J., Bouvier, M., Tesmer, J. J. G., and Sterne-Marr, R. (2014) Mapping the Putative G Protein-coupled Receptor (GPCR) Docking Site on GPCR Kinase 2: Insights from Intact Cell Phosphorylation and Recruitment Assays. *J. Biol. Chem.* **289**, 25262–25275
96. Penela, P., Ribas, C., and Mayor, F. (2003) Mechanisms of regulation of the expression and function of G protein-coupled receptor kinases. *Cell. Signal.* **15**, 973–981

97. Pitcher, J. A., Tesmer, J. J. G., Freeman, J. L. R., Capel, W. D., Stone, W. C., and Lefkowitz, R. J. (1999) Feedback Inhibition of G Protein-coupled Receptor Kinase 2 (GRK2) Activity by Extracellular Signal-regulated Kinases. *J. Biol. Chem.* **274**, 34531–34534
98. Raake, P. W. J., Schlegel, P., Ksienzyk, J., Reinkober, J., Barthelmes, J., Schinkel, S., Pleger, S., Mier, W., Haberkorn, U., Koch, W. J., Katus, H. a., Most, P., and Müller, O. J. (2013) AAV6.βARKct cardiac gene therapy ameliorates cardiac function and normalizes the catecholaminergic axis in a clinically relevant large animal heart failure model. *Eur. Heart J.* **34**, 1437–1447
99. Lymperopoulos, A., Rengo, G., Funakoshi, H., Eckhart, A. D., and Koch, W. J. (2007) Adrenal GRK2 upregulation mediates sympathetic overdrive in heart failure. *Nat. Med.* **13**, 315–323
100. Waldschmidt, H. V., Homan, K. T., Cruz-Rodriguez, O., Cato, M. C., Waninger-Saroni, J., Larimore, K. M., Cannavo, A., Song, J., Cheung, J. Y., Kirchhoff, P. D., Koch, W. J., Tesmer, J. J. G., and Larsen, S. D. (2016) Structure-Based Design, Synthesis and Biological Evaluation of Highly Selective and Potent G Protein-Coupled Receptor Kinase 2 Inhibitors. *J. Med. Chem.* 10.1021/acs.jmedchem.5b02000
101. Lee, D., Bentley, R., Khandekar, S. S., Goodman, K. B., Dul, E., Kirkpatrick, R. B., Doe, C. P., Smith, G. K., Viet, A. Q., Schon, C. A., Yi, T., Semus, S. F., Behm, D. J., Wang, G. Z., Dowdell, S. E., Jolivet, L. J., Hu, E., Evans, C., Elkins, P. A., and Wright, L. L. (2008) Potent, Selective and Orally Bioavailable Dihydropyrimidine Inhibitors of Rho Kinase (ROCK1) as Potential Therapeutic Agents for Cardiovascular Diseases. *J. Med. Chem.* **51**, 6631–6634
102. Homan, K. T., Wu, E., Cannavo, A., Koch, W. J., and Tesmer, J. J. G. (2014) Identification and Characterization of Amlexanox as a G Protein-Coupled Receptor Kinase 5 Inhibitor. *Molecules.* **19**, 16937–49
103. Thal, D., Yeow, R., and Schoenau, C. (2011) Molecular mechanism of selectivity among G protein-coupled receptor kinase 2 inhibitors. *Mol.* **80**, 294–303
104. Homan, K. T., Larimore, K. M., Elkins, J. M., Szklarz, M., Knapp, S., and Tesmer, J. J. G. (2014) Identification and Structure-Function Analysis of Subfamily Selective G Protein-Coupled Receptor Kinase Inhibitors. *ACS Chem. Biol.* 10.1021/cb5006323
105. Homan, K. T., and Tesmer, J. J. G. (2014) Molecular Basis for Small Molecule Inhibition of G Protein-Coupled Receptor Kinases. *ACS Chem. Biol.* 10.1021/cb50033976
106. Otwinowski, Z., and Minor, W. (1997) Processing of X-Ray Diffraction Data Collected in Oscillation Mode. *Methods Enzymol.* **276**, 307–326
107. McCoy, A. J., Grosse-Kunstleve, R. W., Adams, P. D., Winn, M. D., Storoni, L. C., and Read, R. J. (2007) Phaser crystallographic software. *J. Appl. Crystallogr.* **40**, 658–674
108. Murshudov, G. N., Vagin, A. A., and Dodson, E. J. (1997) Refinement of Macromolecular Structures by the Maximum-Likelihood Method. *Acta Crystallogr. Sect. D Biol. Crystallogr.* **D53**, 240–255
109. Afonine, P. V., Grosse-Kunstleve, R. W., Echols, N., Headd, J. J., Moriarty, N. W., Mustyakimov, M., Terwilliger, T. C., Urzhumtsev, A., Zwart, P. H., and Adams, P. D. (2012) Towards automated crystallographic structure refinement with phenix.refine. *Acta Crystallogr. Sect. D Biol. Crystallogr.* **68**, 352–367
110. Emsley, P., and Cowtan, K. (2004) Coot: model-building tools for molecular graphics. *Acta Crystallogr. Sect. D Biol. Crystallogr.* **D60**, 2126–2132

111. Chen, V. B., Arendall, W. B., Headd, J. J., Keedy, D. A., Immormino, R. M., Kapral, G. J., Murray, L. W., Richardson, J. S., and Richardson, D. C. (2010) MolProbity : all-atom structure validation for macromolecular crystallography. *Acta Crystallogr. Sect. D Biol. Crystallogr.* **D66**, 12–21
112. Jacobs, M., Hayakawa, K., Swenson, L., Bellon, S., Fleming, M., Taslimi, P., and Doran, J. (2006) The structure of dimeric ROCK I reveals the mechanism for ligand selectivity. *J. Biol. Chem.* **281**, 260–268
113. Breitenlechner, C., Gaßel, M., Hidaka, H., Kinzel, V., Huber, R., Engh, R. A., and Bossemeyer, D. (2003) Protein Kinase A in Complex with Rho-Kinase Inhibitors Y-27632, Fasudil, and H-1152P. *Structure.* **11**, 1595–1607
114. Bastidas, A. C., Deal, M. S., Steichen, J. M., Guo, Y., Wu, J., and Taylor, S. S. (2013) Phosphoryl transfer by protein kinase A is captured in a crystal lattice. *J. Am. Chem. Soc.* **135**, 4788–4798
115. Li, R., Martin, M. P., Liu, Y., Wang, B., Patel, R. A., Zhu, J. Y., Sun, N., Pireddu, R., Lawrence, N. J., Li, J., Haura, E. B., Sung, S. S., Guida, W. C., Schonbrunn, E., and Sebti, S. M. (2012) Fragment-based and structure-guided discovery and optimization of Rho kinase inhibitors. *J. Med. Chem.* **55**, 2474–2478
116. Waldschmidt, H. V., Homan, K. T., Cato, M. C., Cruz-rodriíguez, O., Cannavo, A., Wilson, M. W., Song, J., Cheung, J. Y., Koch, W. J., Tesmer, J. J. G., and Larsen, S. D. (2017) Structure-Based Design of Highly Selective and Potent G Protein-Coupled Receptor Kinase 2 Inhibitors Based on Paroxetine. *J. Med. Chem.* 10.1021/acs.jmedchem.7b00112
117. Bouley, R., Waldschmidt, H. V, Cato, M. C., Cannavo, A., Song, J., Cheung, J. Y., Yao, X.-Q., Koch, W. J., Larsen, S. D., and Tesmer, J. J. G. (2017) Structural Determinants Influencing the Potency and Selectivity of Indazole-Paroxetine Hybrid G Protein – Coupled Receptor Kinase 2 Inhibitors. *Mol. Pharmacol.* **92**, 707–717
118. Homan, K. T., Wu, E., Wilson, M. W., Singh, P., Larsen, S. D., and Tesmer, J. J. G. (2013) Structural and Functional Analysis of G Protein – Coupled Receptor Kinase Inhibition by Paroxetine and a Rationally Designed Analog. *Mol. Pharmacol.* **85**, 237–248
119. Waldschmidt, H. V, Homan, K. T., Cato, M. C., Cruz-Rodriguez, O., Cannavo, A., Wilson, M. W., Song, J., Cheung, J. Y., Koch, W. J., Tesmer, J. J. G., and Larsen, S. D. (2017) Structure-Based Design of Highly Selective and Potent G Protein- Coupled Receptor Kinase 2 Inhibitors Based on Paroxetine. *J. Med. Chem.* **60**, 3052–3069
120. Waldschmidt, H. V (2017) *Development, Synthesis, and Characterization of G Protein-Coupled Receptor Kinase Inhibitors Using Structure Based Drug Design for the Advancement of Heart Failure Therapeutics*. Ph.D. thesis, University of Michigan
121. Singh, J., Petter, R. C., Baillie, T. A., and Whitty, A. (2011) The resurgence of covalent drugs. *Nat. Rev. Drug Discov.* **10**, 307–317
122. Leproult, E., Barluenga, S., Moras, D., Wurtz, J. M., and Winssinger, N. (2011) Cysteine mapping in conformationally distinct kinase nucleotide binding sites: Application to the design of selective covalent inhibitors. *J. Med. Chem.* **54**, 1347–1355
123. Singh, J., Petter, R. C., and Kluge, A. F. (2010) Targeted covalent drugs of the kinase family. *Curr. Opin. Chem. Biol.* **14**, 475–480
124. Liu, Q., Sabnis, Y., Zhao, Z., Zhang, T., Buhrlage, S. J., Jones, L. H., and Gray, N. S. (2013) Developing irreversible inhibitors of the protein kinase cysteinome. *Chem. Biol.* **20**, 146–159